CRYSTAL CHEMISTRY OF Ca-DOPED AND Ca-FREE

$Pb_2Sr_2RCu_3O_{8+\delta}$ (R = RARE-EARTH)

——— SYNTHESIS, STRUCTURE AND PHYSICAL PROPERTIES

by

JIAYU SIMON XUE, M.Sc.

A Thesis

Submitted to the School of Graduate Studies

in Partial Fulfilment of the Requirements

for the Degree

Doctor of Philosophy

McMaster University

CRYSTAL CHEMISTRY OF Ca-DOPED AND Ca-FREE $Pb_2Sr_2RCu_3O_{8+\delta}$

Doctor of Philosophy (1992) McMaster University

(Chemistry) Hamilton, Ontario

TITLE: Crystal Chemistry of Ca-doped and Ca-free $Pb_2Sr_2RCu_3O_{8+\delta}$

(R = Rare-earth)

———— Synthesis, structure and physical properties

AUTHOR: Jiayu Simon Xue, M.Sc. (Shanghai Inst. for Nuclear Research, China)

SUPERVISOR: Professor J.E. Greedan

NUMBER OF PAGES: XIII, 139

ABSTRACT

A novel PbO/NaCl flux growth method has been developed to grow single crystals of Ca-doped $Pb_2Sr_2(R/Ca)Cu_3O_{8+\delta}$ with R = Nd, Sm, Gd, Dy, Er, Tm, Yb, Lu and Y. The absence of CuO flux enables the crystals to be extracted nondestructively from the melt using an ultrasonic bath and methanol. The as grown $Pb_2Sr_2(Y/Ca)Cu_3O_{8+\delta}$ crystals are of high quality, reasonable size and superconducting with T_c up to 80K. The role of NaCl in the crystal growth process has also been investigated.

The same method was applied to grow a series of Ca-free $Pb_2Sr_2RCu_3O_8$ (R = La, Ce, Pr, Nd, Sm, Eu, Gd, Tb, Dy, Ho, and Y) crystals. X-ray diffraction was used to determine the crystal structures of these compounds. A monoclinic symmetry was found for those crystals with R = Pr, Nd and Tb, orthorhombic for R = La and tetragonal for R = Eu and Dy. Different crystal symmetries can be understood in terms of order/disorder among oxygens in the PbO layers which is driven by an orientational ordering of the Pb^{2+} lone pairs. Bond valence sum calculations were also performed to evaluate the residual strains existing in the crystal structures. A transition from insulating to metallic and superconducting character occurs as a function of decreasing rare-earth size in this Ca-free crystal series. Structural and chemical analyses revealed that the electronic properties of these crystals are closely related to the rare-earth deficiency. Therefore, a cation vacancy carrier-doping mechanism has been proposed for the first time as the most plausible origin of the metallic and superconducting behaviour observed in the $Pb_2Sr_2RCu_3O_8$ crystal series.

ACKNOWLEDGEMENTS

First and foremost, I would like to thank my supervisor, Dr. John E. Greedan, for his inspiration, guidance and support throughout this research. I wish also to express my gratitude to the members of the superconductivity community at McMaster: Drs. J. Barbier, I.D. Brown, H. Dabkowska, A. Dabkowski, C.V. Stager and T. Timusk for many informative discussions and for the interest they showed in this project.

I am indebted to those people who have helped me produce some of the results presented in this thesis, Drs. J. Britten, Y.P. Lin and H. Yun for their assistance with the crystallographic works; J.D. Garrett, H.F. Gibbs, W.H. Gong, J. Hudak, Dr. N. Imanaka and K. Teeter for various instrumental analyses, and M. Maric for some crystal growth work. Special thanks are due to Maureen Reedyk for her long term collaboration. I appreciate the camaraderie from my research group.

I gratefully acknowledge the financial support from the Ontario Centre for Materials Research (OCMR) and Natural Sciences and Engineering Research Council of Canada (NSERC).

Finally, I would like to thank my wife, Su Cheng, for her encouragement, patience and support.

In memory of my father

TABLE OF CONTENTS

LIST OF FIGURES

LIST OF TABLES

SYMBOLS AND ABBREVIATIONS

i) *Structural unit*

RS-unit = Rocksalt-like unit of which the coordination number of metal elements is six or less;

P-unit = Perovskite-like unit of which some metal oxygen layers are oxygen-deficient, and

C-unit = Calcium fluorite-like unit of which the centre metal elements are eight-coordinated.

ii) *Metal oxygen layers*

[ ] = the metal oxygen layers in the RS-unit;

{ } = the metal oxygen layers in the P-unit, and

< > = the metal oxygen layers in the C-unit.

iii) *Chemical formula*

A = alkaline earths, yttrium and rare-earths, or a combination of these elements in the P- or C-units;

R = rare-earths, yttrium or calcium which are intercalated between two CuO_2 planes, thus eight-coordinated in the P-unit, and

M = thallium, lead, bismuth or copper in the RS-unit.

CHAPTER 1

INTRODUCTION

1.1 Historical Development of High-T_c Superconductors

The phenomenon of superconductivity was discovered first by the Dutch scientist K. Onnes in Leiden in 1911 when he observed that the dc electrical resistivity of solid mercury vanishes at 4.1K[1]. He realized that the material undergoes a transition to a new state which he called the ***superconducting state***. Within the next half century, more than 20 metallic elements, numerous alloys and intermetallic compounds have been found to be superconducting under suitable conditions[2]. Among them, two materials: Nb-Ti ——— a ductile alloy with a superconducting transition temperature T_c of 9.6K, and Nb_3Sn ——— a brittle intermetallic compound, with a T_c of 18K attained technological viability in 1960's. Meanwhile, several binary and ternary oxide superconductors began to come on the scene, such as NbO, TiO, $SrTiO_{3-\delta}$ and the bronzes: A_xWO_3, A_xMoO_3 and A_xReO_3 with quite low T_c's ranging from 0.7 to 6K. The crystal structures of NbO and TiO are related to rocksalt, while $SrTiO_{3-\delta}$ and the bronzes have a perovskite structure. A decade later, the T_c of oxide superconductors was raised to 13K by the discovery of two oxides, $Li_{1+x}Ti_{2-x}O_4$[3] and $BaPb_{1-x}Bi_xO_3$[4]. The former has a spinel structure which can be described as a three dimensional corner- or edge-sharing TiO_6 octahedra network with Li in the tetrahedral

sites and the latter, a perovskite structure.

The discovery of superconductivity ($T_c = 29K$) in a La-Ba-Cu-O system by Bednorz and Müller[5] in 1986 began a new era of concentration on oxide superconductors. The announcement in January 1987, by Chu and his associates[6] at the University of Houston, of another copper-based oxide system Ba-Y-Cu-O with $T_c = 92K$, above the liquid nitrogen boiling temperature (77K), sparked great excitement and expectation in both academia and industry, though neither Benorz and Müller nor Chu et al. actually 'identified' the materials which were later shown to be $La_{2-x}Ba_xCuO_4$ and $Ba_2YCu_3O_{7-\delta}$, respectively. Subsequently, many new copper oxide superconductors have been synthesized such as the three homologous copper oxide series: thallium, bismuth and lead cuprates. These series have a large number of derivatives and hybrids and represent a major part of the modern high-T_c superconductors. Their crystal structures contain octahedral CuO_6, or CuO_5 pyramid layers sandwiching oxygen-depleted calcium or rare-earth layers, common to all superconducting cuprates, and rocksalt-like blocks which have material-dependent structural characteristics. Unfortunately, a higher T_c-value of these cuprate superconductors is usually accompanied by an increase in crystal structural complexity.

Superconductivity in $Pb_2Sr_2(Y_{0.5}Ca_{0.5})Cu_3O_{8+\delta}$ (or the 2213 phase, so-called because of the ratio of metal atoms in the compound) reported by Cava et al.[7] in late 1988 has stimulated extensive interest in the exploration of the lead cuprate family. More than seven lead cuprate phases have been reported thus far (see table 1.1). Metallic or superconducting character in these phases is induced via chemical substitutions in those layers near the conducting CuO_2 planes such as, the substitution of divalent cations (or cation vacancies) for the trivalent ions sandwiched between the

two infinite CuO_2 planes (i.e. the 2213 and 1212 phases), or replacing a portion of Sr^{2+} in the SrO layers by La^{3+} (in the 2202 and 1201 phases) adjacent to the CuO_2 planes. Since most of the lead cuprates have been prepared in polycrystalline form, only limited work on their crystal structure and physical properties has been reported except for the 2213 and 1212 phases due to, probably, the availability of additional sample forms (i.e. single crystals and thin films). Of these the 2213 phase has received the most attention, yet it still remains relatively less well-known than the extensively studied $Ba_2YCu_3O_{7-\delta}$ (BYCO) and $Bi_2Sr_2CaCu_2O_8$ (BSCCO) systems for which it might provide new comparative insights. For example, as shown in figure 1.1, the basic structure of $Pb_2Sr_2RCu_3O_8$ (here R stands for rare-earths) contains double CuO_5 square pyramidal layers sandwiching an oxygen-free R layer which is also found in BYCO. Yet the interlayer block PbO-Cu-PbO is more similar to the double BiO layers in BSCCO as is the separation between the conducting layers, ~12Å, which is considerably greater than that for BYCO, ~8Å. An extensive review on the synthesis, crystal structure and physical properties of the 2213 phase has been given by Xue et al.[8]

It is the intent of this dissertation to present a comprehensive study of the 2213 family of lead cuprates including synthesis, crystal growth, structure and physical properties. Highlights include the demonstration of a novel PbO/NaCl flux crystal growth, a discussion of crystal symmetry, that cation vacancies exist at the R-sites of the Ca-free $Pb_2Sr_2RCu_3O_8$ single crystals, that an insulator to metal-superconductor transition takes place with decreasing R radius in the same crystal lattice, and that the cation vacancies may provide the relevant hole doping mechanism.

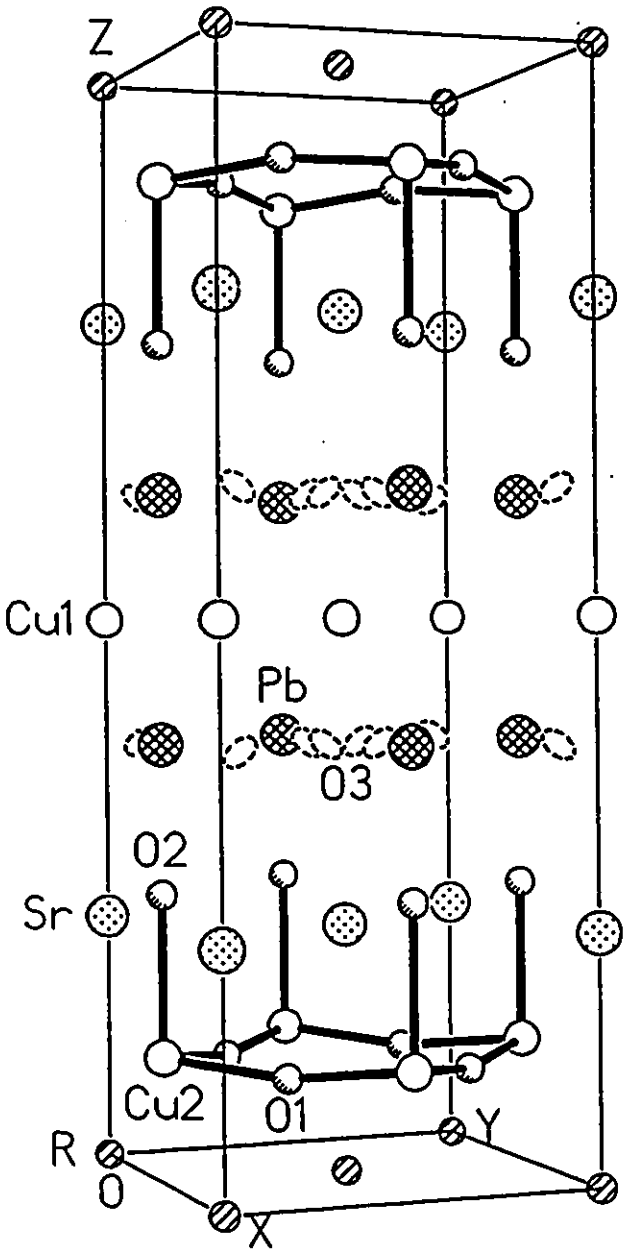

Figure 1.1 Crystal structure of $Pb_2Sr_2RCu_3O_8$.

Table 1.1 Various known lead cuprates.

FORMULAE	PHASES	T_c(K)	SPACE GROUPS
$Pb_2Sr_2(Y/Ca)Cu_3O_{8+\delta}$[7]	2213	70	Cmmm
$(Pb/Cu)Sr_2(Y/Ca)Cu_2O_{7-\delta}$[9]	1212	100	P4/mmm
$Pb_2(Sr/La)_2Cu_2O_{6+\delta}$[10,11]	2202	38	P4/mmm
$(Pb/Cu)(Sr/La)_2CuO_{4+\delta}$[12]	1201	31	P4/mmm
$PbBa(YSr)Cu_3O_{8-\delta}$[13]	0223	50*	I4mm
$(Pb/Cu)(Sr/Eu)_2(Eu/Ce)_2Cu_2O_y$[14]	1222	32	I4/mmm
$Pb_2Sr_2LnCeCu_3O_{10+\delta}$[15]	2223	-	Fmmm

* the phase is semiconducting as reported by Tokiwa et al.[16]

1.2 Superconductivity

A true superconductor is characterized by particular electrical transport and magnetic properties. For example, a superconductor is a material through which a persistent current can flow with no resistance as long as the operating temperature, electric current density and magnetic field are below their critical values T_c, J_c and H_c, respectively. The T_c will, in turn, depend upon the operating current density and magnetic field, or vice versa. Figure 1.2 illustrates that a superconductor will undergo a phase transition from a superconducting state to a normal state if the temperature, current density or magnetic field exceed their critical values. However, the observation

of zero-resistance or nearly zero-resistance is not sufficient to imply superconductivity. When a bulk superconductor is exposed to an applied magnetic field (H_a), it excludes (or shields) flux lines of induction **B** from its interior assuming $H_a \leq H_c$, and $T \leq T_c$. This phenomenon can be expressed mathematically by the following equation

$$B = H_a + \mu_0 M = 0 \qquad (1\text{-}2)$$

where **M** stands for magnetization of the material. This perfect diamagnetism is called the 'Meissner effect'[17] which is a unique property of a superconductor and is, therefore, a more reliable criterion for justifying whether a material is superconducting or not. Materials that completely exclude flux are so-called Type I superconductors which generally have low values of T_c, J_c and H_c. Practical superconductors exhibit another type of magnetic-flux behaviour and are known as Type II superconductors. At low field $H_a < H_{c1}$ these materials show perfect diamagnetism, but at intermediate fields $H_{c1} < H_a \leq H_{c2}$, both normal and superconducting regions co-exist, the flux penetrating these materials in clusters of flux lines, or so-called fluxoids. This is known as the 'mixed state' or 'vortex state'[18]. As the applied magnetic field (H_a) increases, the volume of normal region in the material grows and the superconducting region diminishes. The magnetization of the material reaches zero smoothly when H_a exceeds H_{c2} which indicates that the whole material is in the normal state. All the high temperature copper oxide superconductors are Type II.

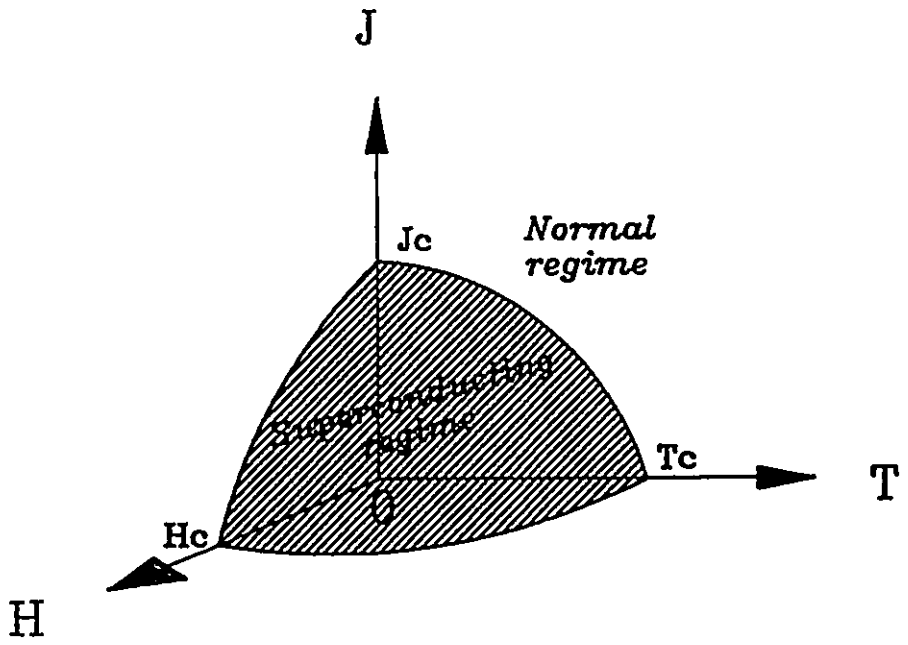

Figure 1.2 Superconducting and normal regimes.

1.3 Oxidation state

A widely accepted point of view regarding the origin of superconductivity in copper oxide superconductors is that a critical concentration of charge carriers in the two-dimensional CuO_2 planes is necessary. Since the mobile carriers in the CuO_2 planes are so important in interpreting the magnetic, electronic and superconducting properties of these materials, a good understanding of the oxidation state of Cu will be beneficial. Unfortunately, the terminology "oxidation state" is used frequently without clear definition by many solid-state scientists. In principle, the oxidation states of metal ions are determined by the nature of oxygen bonding; the oxidation state of oxygen in a pure ionic solid is negative two (or O^{-II}). This is so-called the "ionic model". In the case of a 100% ionic oxide, the oxidation state of a metal ion is equal to its charge. However, even in MgO, one of the highly ionic oxides, the real charges of Mg^{II} and O^{-II} are reduced to +1.5 and -1.5, respectively[19]. Thus the oxidation state in real cases is *not* equal to the ionic charge of an ion. The bonding between Cu^{II} and O^{-II} in these superconductors is not strongly ionic, with a relatively large covalent component. The real charge for the Cu^{II} ion is much lower than +2. In practice, however, the oxidation state of an ion is assigned assuming the ionic model works. By this assumption, the oxidation states of metals in oxides can be assigned straightforwardly. Meanwhile the terms Cu^{3+} and O^{-1} have been also utilized by many authors for describing the oxidized copper oxide superconductors. Several techniques, such as electron paramagnetic resonance (EPR)[20], electron energy loss (EELS)[21], x-ray photoelectron (XPS), Auger spectroscopies[22,23] and x-ray absorption measurements have been employed in the copper oxide superconductors. The results

show evidence for valences of 2+ and 1+ for Cu ions, but no presence of Cu^{3+}. Rather a case is made for O^{-1}. However, due to the large amount of d-p orbital mixing in these compounds neither description in terms of Cu^{3+} and O^{-1} is strictly correct. For convenience, we prefer to measure the hole concentration in terms of Cu^{3+}. The calculated oxidation states of anions or cations in this text will be represented as Arabic superscripts (i.e. O^{-2}, $Cu^{+2.1}$) which can be fractional numbers, while the oxidation states by definition will be designated by Roman superscripts (i.e. O^{-II}, Cu^{II}) which are always integers.

1.4 Charge transfer models

The next question concerns the circumstances under which the modification of Cu oxidation states can be accomplished. This aspect is crucial in manipulating the superconducting properties of these materials. Since all of the copper oxide superconductors have layer-type structures, these layers can be classified into two distinct blocks according to their physical functions. One is called the 'superconducting block', a perovskite-like structural unit (or P-unit) composed of a few di-, or tri-valent metal layers sandwiched by the CuO_2 layers, or simply of just single CuO_2 layer. The other, the 'charge reservoir block', commonly refers to the rocksalt-like, or calcium fluorite-like units (RS-, or C-units). These blocks are bi-functional: forming the framework of the material and supplying charge carriers for the CuO_2 planes by a charge transfer mechanism[24]. The charge carriers in the CuO_2 planes can be created by various carrier-doping mechanisms.

1.5 Carrier-doping mechanisms

All solids contain defects and impurities which lead to a perturbation in the electronic structure. The physical properties of many solids are in fact dominated by such defects. According to most researchers, superconductivity in copper oxide superconductors is closely related to those defects such as: chemical doping, anion or cation vacancies, interstitial atoms ... etc. These defects create the mobile charge carriers in the conduction band[25], which presumably originate from the CuO_2 planes. Those superconductors with positive charge carriers are called 'p-type'; and those with negative charge carriers, 'n-type'. Naturally, the average oxidation state of copper (formally +2.0) is a convenient quantity to measure the mobile charge carriers in the CuO_2 planes. The optimum value of the average formal oxidation state of copper seems to range from 2.06 to 2.32 for p-type superconductors, and 1.78 to 1.74 for n-type[26]. The concentration of mobile charge carriers in the CuO_2 planes of the superconducting materials can be manipulated via several mechanisms described below.

Mechanism I ——— Chemical substitution

The desired concentration of mobile charge carriers in a material can be achieved by chemical doping. For instance the tri-valent cations (i.e. rare-earth ions) in the copper oxide superconductors can be partially substituted by di-valent cations (Ca^{2+}, Sr^{2+} or Ba^{2+}), or tetra-valent cations (Ce^{4+} or Th^{4+}). The di-valent cation substitution will lead to an oxidation of some Cu^{II} to Cu^{III} due to the local charge neutrality principle, thus positive charge carriers (holes) are introduced into the Cu-d(x^2-

y^2) and O-p(xy) subbands and a p-type superconductor results. Similarly, an n-type superconductor can be obtained by the tetra-valent cation substitution which introduces negative charge carriers (electrons) into the material and leads to the reduction of the CuO_2 planes.

Mechanism II ——— Anion vacancies

Superconducting copper oxides, like other oxides, have anion (or oxygen) vacancies. These anion vacancies, the concentration of which can be changed through various annealing procedures, are crucial in order to induce superconductivity into the host materials. For example, the oxygen vacancies in $La_{2-x}Sr_xCuO_{4-\delta}$ can be filled by annealing under an oxygen atmosphere. Since La^{III} and Sr^{II} are much more stable than Cu^{II}, an increase in oxygen content will lead to the partial oxidation of Cu^{II} to Cu^{III}. On the contrary, the oxygen content in $Nd_{2-x}Ce_xCuO_4$ can be reduced by annealing the sample under an inert atmosphere (nitrogen or argon) or vacuum at high temperature, which facilitates the partial reduction of Cu^{II} to Cu^{I}.

Mechanism III ——— Cation vacancies

The correlation between cation vacancies and superconducting properties is less well studied and understood than mechanisms I and II, probably because they have been reported only in a few superconducting systems: $Tl_{1.84}Ba_{2.1}CuO_{5.70}$[27], $Tl_{1.94}Ba_{1.96}Ca_{1.07}Cu_{1.96}O_{8.21}$[28], $Bi_2Sr_{2-x}CuO_{6-\delta}$[29] ($x = 0.1$ to 0.5) and $Bi_{1.88}Sr_{2.04}Ca_{0.97}Cu_{2.18}O_{7.98}$[30]. The presence of cation vacancies in copper oxides is not an unexpected result because such vacancies are observed in numerous inorganic solids[31,32]. Cation vacancies in the crystal lattice function as zero-valence ions, or

as the strong negative charged centres due to the anions surrounding them. These negative charges can be compensated by an equal number of anion (usually oxygen) vacancies with the same amount of positive charge created near the negative charge centres, which is the so-called 'Schottky defect'. Another alternative is to compensate the negative charges around a cation vacancy by increasing the oxidation state of some nearby Cu^{II}.

Mechanism IV ——— Interstitial oxygens

Interstitial oxygens can be introduced into superconducting materials by oxygen annealing. The addition of interstitial oxygens will attract the negative charge carriers (i.e. electrons) at the expense of increasing the oxidation state of some cations (i.e. Cu^{II}). Obviously, this is a hole carrier-doping mechanism. The existence of interstitial oxygens has been observed only in bismuth cuprate superconductors[33] due to a dimensional mismatch between Bi_2O_2 and CuO_2 layers which is more serious than in the other Cu-based superconductors and can be lessened by the presence of interstitial oxygens in the Bi_2O_2 layer.

Mechanism V ——— Internal reduction/oxidization

Since there is no apparent chemical doping in most of the thallium cuprate systems (i.e. $Tl_2Ba_2CaCu_2O_8$, $Tl_2Ba_2Ca_2Cu_3O_{10}$ ... etc.), the superconducting properties of these systems have been attributed to various mechanisms: anion or cation vacancies, interstitial oxygens ... etc. None seem convincing. Thus the idea of 'self-doping' was proposed according to the chemistry of thallium[34] wherein part of the Cu^{II} is oxidized due to the redox reaction of $2Tl^{3+} + Cu^{2+} \longrightarrow Tl^{3+} + Tl^{+} + Cu^{3+}$.

Structural studies of Tl-based cuprates have indicated displacements of thallium and oxygen from their ideal positions. The highly asymmetrical bonding environment of Tl implies the existence of mono-valent Tl^{+1} which has a sterically active lone pair of electrons. A structural model of a 2x2 supercell along both a- and b-axes has been suggested by Dmowski et al.[35] based on a superstructure observed by electron diffraction.

Of course it should be emphasized that in most cases the superconducting properties of a high-T_c superconducting material reflect an integrated result of several carrier-doping mechanisms.

CHAPTER 2

CRYSTAL STRUCTURES OF HIGH-T_c COPPER OXIDE SUPERCONDUCTORS

A good crystal structural knowledge of the high-T_c superconducting copper oxides is important for interpreting their physical properties and in searching for new superconducting materials. Several very valuable review articles are available, such as on structural aspects by Jorgensen[36], Hewat[37], Rao[20], Torrance et al.[38], and Yvon et al.[39], on crystal chemistry aspects by Wilson[40], Cava[41], Raveau et al.[42], Santoro et al.[43], and Sleight[19]. The purpose of this chapter is to give a brief, up-to-date outline on the crystal structures of high-T_c superconducting copper oxides by classifying them into three main structural series.

As mentioned previously, the crystal structures of currently known Cu-based superconductors are built from three simple structural units: RS-, C- and P-units. The stacking sequences of the metal oxygen layers in the RS-, C- and P-units can be illustrated as $[^6MO]$, $<^8A.O_2.^8A>$ and $\{^5CuO.^8R.^5CuO\}$*, respectively. A large number of layered copper oxide structures can be constructed by varying the layer-stacking sequence. However, the compounds which exist now or may be prepared in the future, are those structures which are subject to several crystal chemical constraints: commensurability, coordination environment, local charge neutrality ... etc.

---

* here, the superscript denotes the coordination number of the metal ions.

2.1 A general formula for superconducting copper oxides

Since all the known copper oxide superconductors have a pseudo-tetragonal symmetry and a layered structure with different stacking of three basic structural types: RS-, P- and C-units (or [ ], { } and < >), they can be thus conveniently written as a general formula:

$$[MO]_m\{<AO>\}_2\{R_{n-1}Cu_nO_{2n}\}$$

Here, the [MO] represents the metal oxide layers (usually M = Tl, Pb, Bi or Cu) in the RS-unit; and m, which is an integer in most cases and half-integer for a few structural hybrids, designates the number of MO layers. {<AO>} are the alkaline earth or rare-earth oxide layers in either the P- or C-units ({ } or < >). They are usually adjacent to the CuO_2 planes. The content in the last curly bracket, $\{R_{n-1}Cu_nO_{2n}\}$, refers to a most important part of these copper oxide materials ——— the superconducting blocks. Here, n indicates the number of CuO_2 planes in the P-unit. Obviously, the number of metal oxide layers in the P-units will be equal to 2n + 1. This general formula can also be applied to other highly symmetric transition metal oxides such as: iron oxides (m = 2, 3; n = 1, 2, 3, 4)[44] or vanadium oxides (m = 0; n = 1, 2, 3)[45] by replacing the Cu in the formula with Fe or V.

These high-T_c superconducting copper oxides can be classified into three series according to their structural features. The series I - $A_2R_{n-1}Cu_nO_{3n+1}$ is mainly built of P- and C-units (n = 1, 2, 3 and ∞). The members in this series display a rather simple structural format. The series II - $M_mA_2R_{n-1}Cu_nO_{4n-\delta}$ features CuO chains in the RS-unit

(n = 2, m = 1, 1.5 or 2) where δ is a variable assigned to accommodate oxygen stoichiometry in different phases. The last series - $M_mA_2R_{n-1}Cu_nO_{m+2n+2}$ is assembled by stacking the P- and RS-units (m = 1, 2 or 3; n = 1, 2, 3 or 4) in a straightforward but complex way.

2.2 $A_2R_{n-1}Cu_nO_{3n+1}$ series

There are four known superconducting copper oxide phases in the series I: n = 1, 2, 3 and ∞. They are listed in table 2.2 together with the references denoted by the superscripts on each compound, lattice parameters, space groups (S.G.) and superconducting transition temperatures (T_c). Most of the crystallographic information presented here has been obtained from single crystal x-ray and powder neutron diffraction techniques. $La_{2-x}Ba_xCuO_4$, an n = 1 member in the $A_2R_{n-1}Cu_nO_{3n+1}$ series was the first compound discovered among the family of high-T_c superconducting copper oxides. It has a crystal structure related to K_2NiF_4. The unit cell of $La_{2-x}Ba_xCuO_4$ is composed of one CuO_2 layer sandwiched by two AO layers (figure 2.2.1a). The layer sequence of the compound can be written as $\{^9AO.^6CuO_2.^9AO\}$. The compound is also named the ***T-phase*** due to its tetragonal symmetry. The copper oxygen octahedra form corner-sharing, two-dimensional CuO_2 sheets in the basal plane, while the A ions are coordinated by nine oxygens (CN = 9). Another convenient way to present the crystal structures of these layered oxides is to project the three dimensional (3-D) unit cell onto a two dimensional (2-D) diagram along the b-axis (figure 2.2.2). $La_{2-x}Sr_xCuO_4$ is the solid solution between La_2CuO_4 which has a distorted orthorhombic unit cell with a space group of Bmab, and Sr_2CuO_3 which is also orthorhombic with a space group

of Immm[46]. Both La_2CuO_4 and Sr_2CuO_3 are insulators, but tetragonal $La_{2-x}Sr_xCuO_4$ (x=0.15) shows metallic behaviour and is superconducting at 40K which is, presumably, induced by the chemical substitution of Sr^{2+} for La^{3+}. The charge carriers (holes) are transferred from the charge reservoir {AO} to the CuO_2 planes.

The crystal structure of the so-called electron superconductor, $Nd_{2-x}Ce_xCuO_4$, is different from $La_{2-x}Sr_xCuO_4$ despite their similarities in chemical formula, unit cell dimensions and stacking sequence of the metal layers. The compound has a tetragonal symmetry and has been called the ***T'-phase***[47]. Superconductivity (T_c=24K) in the $Nd_{2-x}Ce_xCuO_4$ compound occurs for a narrow range of x-values from 0.14 to 0.17. The layer stacking sequence in $Nd_{2-x}Ce_xCuO_4$ is $<^8A.O_2.^8A>\{^4CuO_2\}$. The C-unit $<^8A.O_2.^8A>$ in $Nd_{2-x}Ce_xCuO_4$ can be derived from $\{^9AO\}_2$ in $La_{2-x}Sr_xCuO_4$ by translating the oxygens from the AO layers halfway between the A layers along the c-axis, followed by a 45° rotation about the axis. The consequence of these operations is that the coordination number of the rare-earth ions is reduced from nine to eight, meanwhile the Cu ions become four-coordinated with no oxygen above and below. A remarkable feature of $Nd_{2-x}Ce_xCuO_4$ is that it exhibits a negative coefficient of 'Hall effect' in the normal state, which indicates that the mobile charge carriers in the compound are electrons. Obviously, these negative charge carriers in $Nd_{2-x}Ce_xCuO_4$ are introduced by partial substitution of tri-valent Nd^{3+} ions with tetra-valent Ce^{4+}.

The crystal structure of $Nd_{2-x-y}Ce_xSr_yCuO_{4-\delta}$ (n=1) or the ***T**-phase** as shown in figure 2.2.2b, is a hybrid of $La_{2-x}Sr_xCuO_4$ and $Nd_{2-x}Ce_xCuO_4$. A layer sequence of $<^8A.O_2.^8A>\{^5CuO_2.^9AO\}\{^9AO.^5CuO_2\}$ shows that the top half of the unit cell is similar to that of $La_{2-x}Sr_xCuO_4$ and the bottom half to $Nd_{2-x}Ce_xCuO_4$. However, $Nd_{2-x-y}Ce_xSr_yCuO_{4-\delta}$ is a hole-conducting superconductor.

$La_2SrCu_2O_6$ (n=2) was first prepared by Nguyen et al.[48] in 1980. The crystal structure of $La_2SrCu_2O_6$ (see figure 2.2.3a) is similar to that of $La_{2-x}Sr_xCuO_4$ except that there are three layers, $\{^5CuO_2.^8R.^5CuO_2\}$, in each P-unit instead of one, $\{^6CuO_2\}$, as in the latter. The stacking sequence of $La_2SrCu_2O_6$ can be presented as $\{^9AO.^5CuO_2.^8R.^5CuO_2.^9AO\}$. $La_2SrCu_2O_6$ is metallic and nonsuperconducting down to 5K even after high pressure oxygen annealing[49] which enhances the oxygen content from 6 to 6.2. Later Cava et al.[50] and Fuertes et al.[58] reported the presence of superconductivity in the compounds $La_{2-x}Sr_xCaCu_2O_6$ (x=0.4) and $La_2CaCu_2O_{6+\delta}$, respectively. The superconductivity in these compounds seems to be induced by hole-doping in the double CuO_2 planes via chemical substitution or by high pressure oxygen annealing (20 atmospheres, 970°C) which brings the oxygen content from 5.8 to 6.04. Other n=2 members, $La_{1.7}Ca_{1.3}Cu_2O_y$ and $La_{1.7}Sr_{1.3}Cu_2O_y$ have been prepared by Okai using a high pressure approach (6GPa, 1050°C for 1 hour) and $KClO_3$ as an oxygen-generator[59].

$Ln_6Ba_4Ce_2Cu_9O_{30-\delta}$ (Ln=Nd, Sm and Eu) is the n=3 member in the $A_2R_{n-1}Cu_nO_{3n+1}$ series. The crystal structure of the compound comprises an alternating stacking of P- and C-units (figure 2.2.3b). The P-units in $Ln_6Ba_4Ce_2Cu_9O_{30-\delta}$ are seriously oxygen-deficient (about three quarters of the oxygens are missing). The layer sequence of $Ln_6Ba_4Ce_2Cu_9O_{30-\delta}$ is $<^8A.O_2.^8A>\{^5CuO_2.^9AO.^3CuO.^9AO.^5CuO_2\}$.

The recent successful synthesis of $Sr_{1-x}Nd_xCuO_2$ (x=0.15)[61] which can be loosely defined as the end member (n=∞) of the $A_2R_{n-1}Cu_nO_{3n+1}$ series, has received much attention for several reasons: i) it is a parent compound of almost all of the high-T_c copper oxide superconductors because of its simple two dimensional CuO_2 planes; ii) there is no charge reservoir in its crystal structure which is an unexpected result for

those who believe that the charge reservoir is necessary for inducing superconductivity in high-T_c copper oxide superconductors[26] and iii) it is the second electron-doped superconductor (T_c=40K) reported so far. Efforts towards the synthesis of $RCuO_2$-type structure compounds started a few years ago. Although, solid solutions of $Ba_{1-x}Sr_xCuO_2$ and $Sr_{1-x}Ca_xCuO_2$ were prepared under high pressure (up to 60kbar, 1050°C) by several research groups[51,52], an ambient pressure synthesis is possible such as the $Ca_{0.86}Sr_{0.14}CuO_2$ single crystals prepared by Roth et al.[53] The compound $Nd_{0.05}(Ca_{0.3}Sr_{0.7})_{0.95}CuO_y$ might be the first trial of doping $Sr_{1-x}Ca_xCuO_2$ with tri-valent Nd ions[54]. Unfortunately, the compound was not found to be superconducting due to a low doping level. $Sr_{1-x}Nd_xCuO_2$ has been prepared under high pressure and temperature (25 kbar, 1,000°C)[61]. It has a simple oxygen-deficient perovskite structure (figure 2.2.3c). The Sr/Nd layers are sandwiched by two infinite CuO_2 sheets or *vice versa*. Efforts to hole-dope the $RCuO_2$-type compounds by placing mono-valent ions into the R sites have not been successful so far.

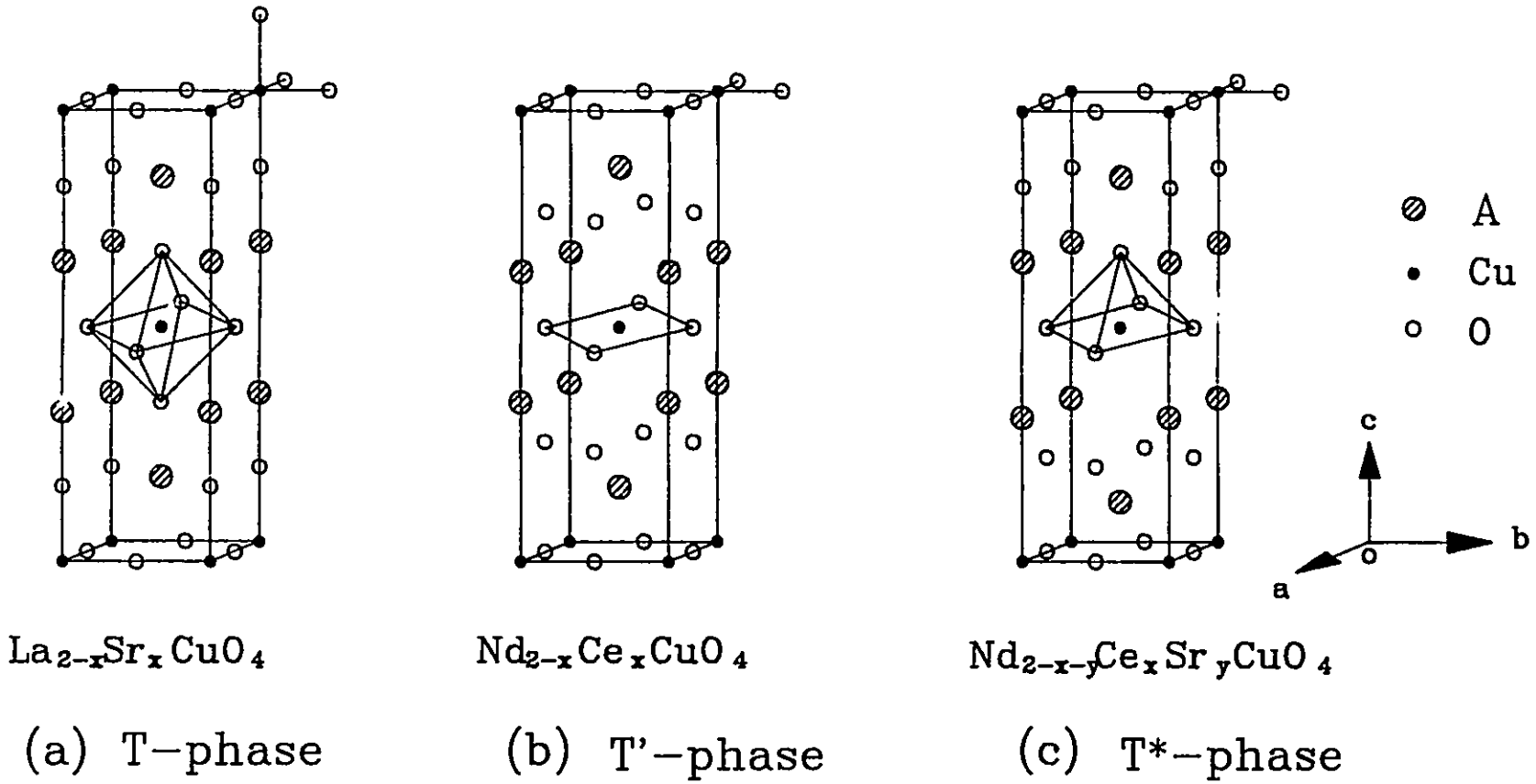

Figure 2.2.1 Three dimensional crystal structures of the compounds in series I - $A_2R_{n-1}Cu_nO_{3n+1}$ (n = 1).

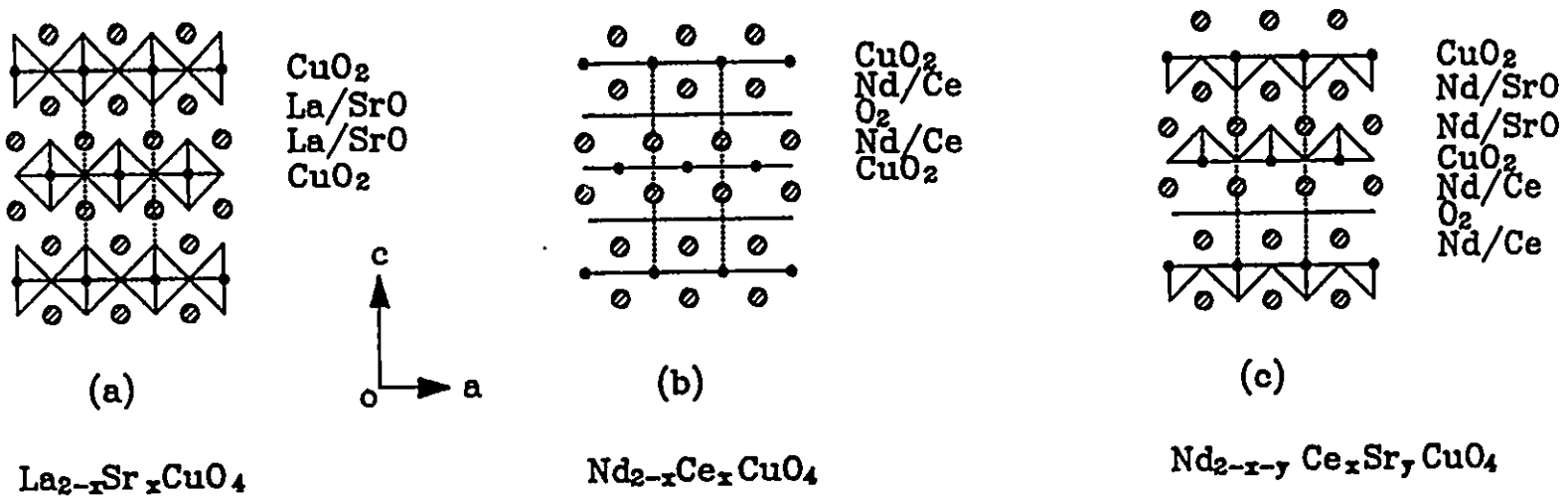

Figure 2.2.2 Two dimensional crystal structures of the compounds in series I - $A_2R_{n-1}Cu_nO_{3n+1}$ (n = 1).

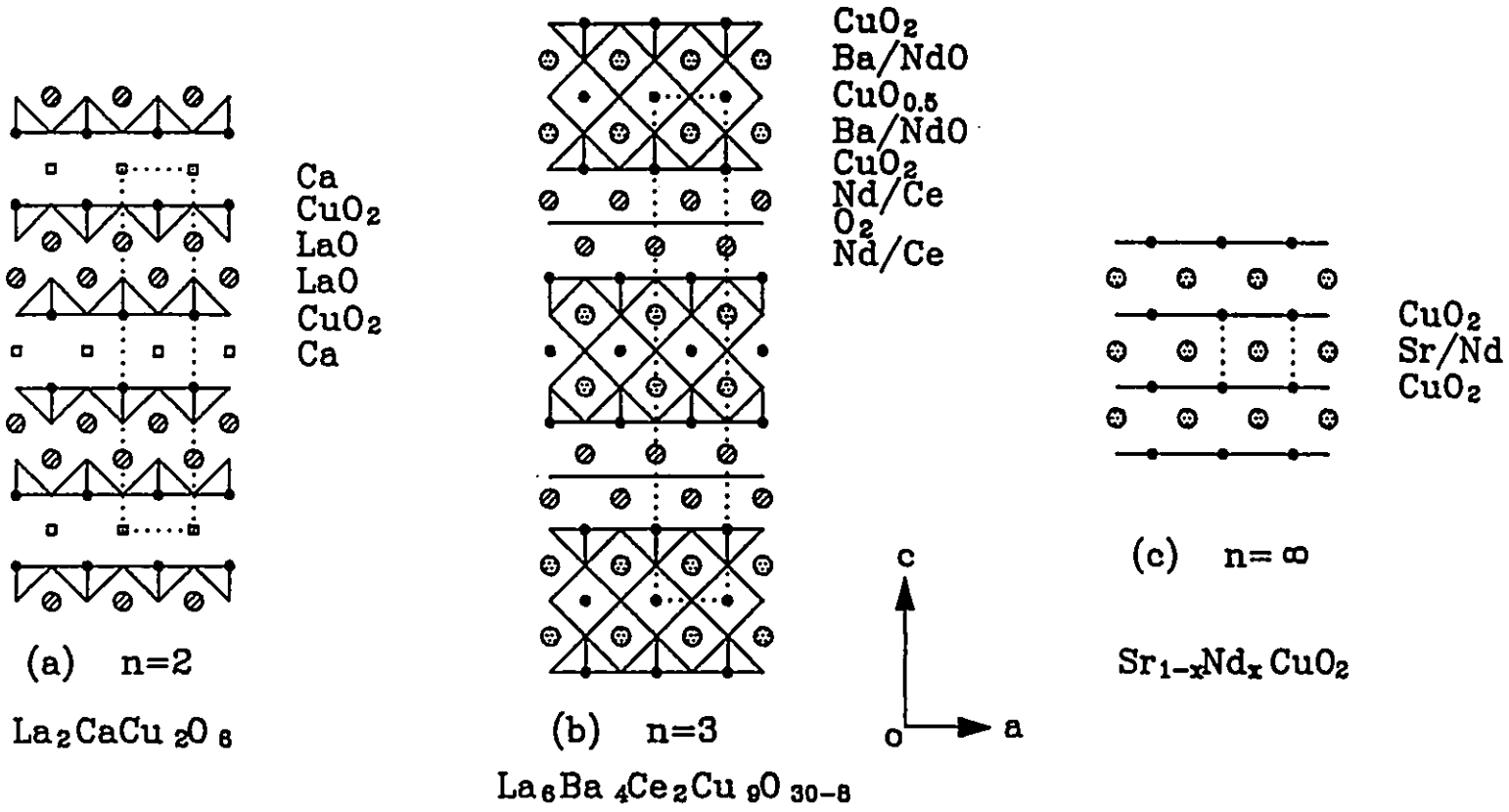

Figure 2.2.3 Series I - $A_2R_{n-1}Cu_nO_{3n+1}$ (n > 1)

Table 2.2 The $A_2R_{n-1}Cu_nO_{3n+1}$ series*.

n	$A_2R_{n-1}Cu_nO_{3n+1}$	a(Å)	c(Å)	S.G.	T_c(K)
1	$La_{2-x}A_xCuO_4$[55] (A = Ca,<u>Sr</u>,Ba)	3.7793(1)	13.2260(3)	I4/mmm	**40**
	$Nd_{2-x}Ce_xCuO_{4-\delta}$[56]	3.948(1)	12.045(2)	I4/mmm	**24**
	$Nd_{2-x-y}Ce_xSr_yCuO_{4-\delta}$[57]	3.8563(3)	12.4842(9)	P4/mmm	**28**
2	$(La/Sr)_2CaCu_2O_6$[50]	3.82	19.60	I4/mmm	**60**
	$La_2CaCu_2O_{6+\delta}$[58]	3.83350(5)	19.5169(4)	I4/mmm	**45**
	$(La/Ca)_2CaCu_2O_y$[59]	3.872	19.4851		**70**
	$(La/Sr)_2SrCu_2O_y$[59]	3.8592	19.9686		**75**
3	$Ln_6Ba_4Ce_2Cu_9O_{30-\delta}$[60] (Ln = <u>Nd</u>,Sm & Eu)	3.85044(6)	28.4598(5)	I4/mmm	**43**
∞	$Sr_{1-x}R_xCuO_2$[61] (R = <u>Nd</u>,Pr)	3.942	3.382	P4/mmm	**40**

* in the case of a phase composed of several compounds, the lattice parameters presented here correspond to the one with an underline.

2.3 $M_mA_2R_{n-1}Cu_nO_{4n-\delta}$ series

Only three phases (m = 1, 1.5 and 2) have been reported in series II (see table 2.3). $Ba_2YCu_3O_{7-\delta}$, or the well known '123-phase', is one of the most extensively studied high-T_c superconductors. The crystal structure of $Ba_2YCu_3O_{7-\delta}$ is tetragonal for

$\delta \geq 0.6$ and orthorhombic for $\delta < 0.6$. The layer sequence of the compound ($\delta \approx 0$), $[^{4}CuO]\{^{10}AO.^{5}CuO_2.^{8}R.^{5}CuO_2.^{10}AO\}$, shows that there exist two different kinds of Cu ions: five-coordinated Cu^{II} in the 2-D CuO_2 sheets of the P-units and four-coordinated Cu^{I} in the 1-D CuO chains of the RS-units. The correlation between oxygen stoichiometry and superconducting properties in this compound is very interesting. A plot of T_c vs δ exhibits two-plateau of 90K and 60K corresponding to δ-values of 0 and 0.5 respectively. The combination of powder neutron and electron diffraction techniques reveals that the 90K plateau corresponds to the structural feature of a well-ordered oxygen array in the CuO chain along the b-axis, which is also the origin of the orthorhombicity in the crystal structure. The oxidation state of copper in the oxygen-deficient CuO_δ chains depends on the number of neighbouring oxygens. Removing the oxygen in the 1-D CuO chains via controlled annealing procedures[62,63], results in a reduced electron density in the charge reservoir which will be compensated by negative charge transfer from the CuO_2 planes. Meanwhile, the Cu^{II} ions in the double CuO_2 planes are oxidized, thus more hole carriers in the conduction band are created. The effects of the charge transfer are related closely to the structural change of the compound. A $2xa_p$ superstructure has been observed in the 60K phase[62,64], which suggests an 'empty-full-empty-full...' configuration of oxygen ordering existing in the CuO_δ chains along the a-axis. Another analogue of $Ba_2YCu_3O_{7-\delta}$, $Sr_2YCu_3O_y$, has a T_c of 60K. A brutal approach (an oxygen pressure of 7GPa, 1380°C) must be taken in the synthesis of $Sr_2YCu_3O_y$ to stabilize the Sr ions in the lattice[69].

$Ba_2YCu_4O_8$ (the 124-phase) was discovered by electron microscopy work on a $Ba_2YCu_3O_{7-\delta}$ powder sample[65]. The structure of $Ba_2YCu_4O_8$ is similar to that of $Ba_2YCu_3O_{7-\delta}$ except for double CuO_δ chains in the former in place of single one in the

latter. The extra chains lead to a new layer sequence, $[^4CuO.^4CuO]\{^{10}AO.^5CuO_2.^8R.^5CuO_2.^{10}AO\}$, and double the length of the c-axis to 27.24Å. The T_c of $Ba_2YCu_4O_8$ is about 10K lower than that of $Ba_2YCu_3O_{7-\delta}$, while the Ca-doped sample is nonsuperconducting[68].

$Ba_4Y_2Cu_7O_{14+\delta}$ (or 247-phase) is the third member (m = 1, n = 2) in the $M_mA_2R_{n-1}Cu_nO_{4n-\delta}$ series. Its crystal structure can be established by the alternate stacking of $Ba_2YCu_3O_6$-like blocks, $[^4CuO]\{^8AO.^5CuO_2.^9R.^5CuO_2.^8AO\}$, and $Ba_2YCu_4O_8$-like blocks, $[^4CuO.^4CuO]\{^{10}AO.^5CuO_2.^8R.^5CuO_2.^{10}AO\}$ (figure 2.3). The compound has to be synthesized under high oxygen pressure: 2kbar, 1,200°C without flux[67] or 100bar, 1,060°C with the $BaCuO_2$/CuO flux[70].

Table 2.3 The $M_mA_2R_{n-1}Cu_nO_{4n-\delta}$ series (A = Ba; R = Rare-earths or Y)

m	n	$M_mA_2R_{n-1}Cu_nO_{4n-\delta}$	a(Å)	b(Å)	c(Å)	S.G.	T_c(K)
1	2	$Ba_2RCu_3O_{7-\delta}$[68] (R = Y or Ln)	3.8282(4)	3.8897(4)	11.694(1)	Pmmm	90
		$Sr_2YCu_3O_y$[51,69]	3.7949		11.4102		60
1.5	2	$Ba_4Y_2Cu_7O_{14+\delta}$[70]	3.851(1)	3.869(1)	50.29(2)	Ammm	40
2	2	$Ba_2YCu_4O_8$[71]	3.8411(2)	3.8718(2)	27.240(1)	Ammm	80

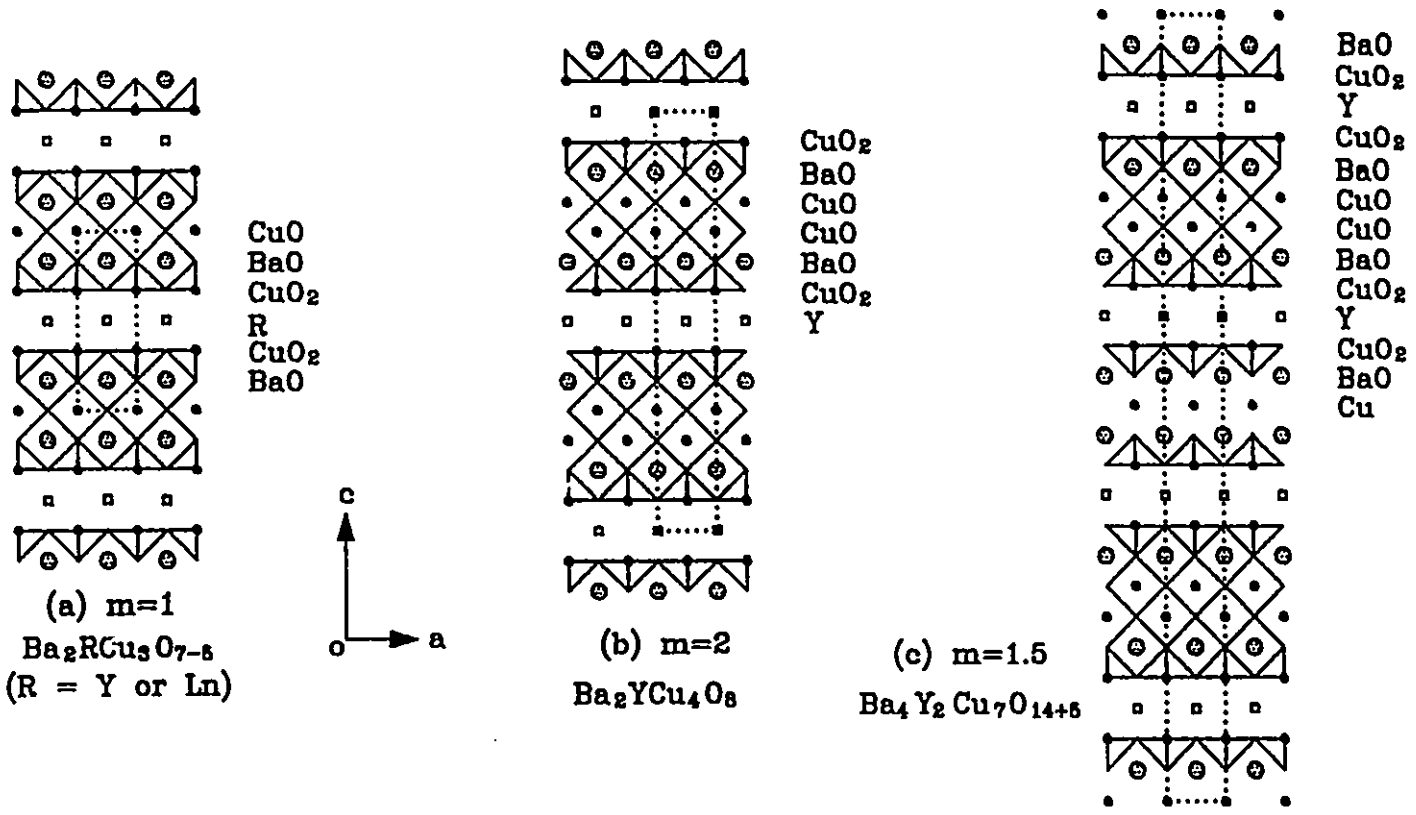

Figure 2.3 Series II - $M_mA_2R_{n-1}Cu_nO_{4n-\delta}$

2.4 $M_mA_2R_{n-1}Cu_nO_{m+2n+2}$ series

The $M_mA_2R_{n-1}Cu_nO_{m+2n+2}$ series represents a large number of copper oxide superconductors which have relatively high T_c values and nearly all of the structural features possessed by the compounds of series I and II. The Tl, Pb and Bi cuprates have a relatively straightforward structural pattern, but the origin of their superconducting properties has not always been obvious.

The $M_mA_2R_{n-1}Cu_nO_{m+2n+2}$ series (m = 1)

All the compounds listed in table 2.4.1, the m = 1 members in the $M_mA_2R_{n-1}Cu_nO_{m+2n+2}$ series, can be classified structurally into three phases by m-n indices (i.e. 1-1, 1-2 and 1-3). They were first discovered in the thallium cuprate system by Parkin et al.[82] using electron microscopy. All three phases have tetragonal symmetry and a space group of P4/mmm. There is only one [MO] layer per unit cell (m = 1) sandwiched by two {AO} layers (BaO or SrO). The superconducting layers can be just one $\{CuO_2\}$ layer or a series of consecutive $\{CuO_2\}$ and R layers depending on the number n = 1, 2 or 3. Their crystal structures are shown in figure 2.4.1 and their layer stacking sequences are as follows:

1-1 phase (or Tl, Pb/Cu, Bi-1201): $[^6MO]\{^9AO.^6CuO_2.^9AO\}$;

1-2 phase (or Tl, Pb/Sr, Bi-1212): $[^6MO]\{^9AO.^5CuO_2.^8R.^5CuO_2.^9AO\}$, and

1-3 phase (or Tl-1223)[b]: $[^6MO]\{^9AO.^5CuO_2.^8R.^4CuO_2.^8R.^5CuO_2.^9AO\}$.

---

[b] here the first, second, third and fourth numbers correspond to the number of M, A, R and Cu atoms in the chemical formula, respectively.

The crystal structure of the 1201 phase can be derived from that of La_2CuO_4 by substituting the two LaO layers with two alkaline earth layers {AO} and intercalating a [MO] layer in between. The T_c of $TlBa_2CuO_{5-\delta}$ has been raised[79] from ~10K to 52K after a partial substitution of La^{3+} for Ba^{2+}. An insulating/superconducting transition as a function of La^{3+} doping level has also been observed. However, the role of La^{3+}-doping in Tl-1201 is controversial: in one case, T_c was reported to be proportional to the La^{3+}-doping[79], while the work done by Sundaresan et al.[72] gave an opposite result. This might be a good example to show that the superconductivity of the high-T_c copper oxides can not be interpreted simply by chemical doping; other factors such as oxygen stoichiometry ... etc. also have to be taken into account.

Single crystals of Tl-1212 and 1223 have been grown by Morosin et al.[73,74] A formula of $Tl_{1.17}Ba_{2.0}Ca_{0.83}Cu_{2.0}O_{6.75}$ determined by single crystal x-ray diffraction indicates partial substitution of Tl^{3+} for Ca^{2+}. A similar situation was found in the case of $Tl_{1.1}Ba_{1.88}Ca_{1.90}Cu_3O_9$, or Tl-1223[75]. A multiphased sample containing Tl-1234, $Tl(Ba,Ca)_2Ca_3Cu_4O_{10.5+\delta}$, with $T_c = 122K$ was reported by Haldar et al.[76] No decent structural data is available for the Bi-1201 and 1212 phases due to poor sample quality as the lone pair electrons in the valence shell of the Bi^{3+} ions lead to a serious distortion in the coordination environment of Bi^{3+} and an accompanying structural instability. The Pb-1201 and 1212 phases, both containing Pb^{4+} ions, are iso-structural with the Tl cuprates. The Pb-1212 phase was first synthesized by Subramanian et al.[101], and becomes superconducting at $T_c = 100K$ as claimed by Rouillon et al.[9] although this result has not been duplicated by any other groups. Various hybrids among Pb, Tl and Bi cuprates have been reported[77,78].

Table 2.4.1 The $M_mA_2R_{n-1}Cu_nO_{m+2n+2}$ series (m = 1).

m n $M_mA_2R_{n-1}Cu_nO_{m+2n+2}$	a(Å)	c(Å)	S.G.	T_c(K)
1 1 $TlBa_{1.2}La_{0.8}CuO_5$[79]	3.8479(3)	9.0909(6)	P4/mmm	**52**
$(Pb/Cu)(Sr/La)_2CuO_{5-\delta}$[12]	3.787(2)	8.652(1)	P4/mmm	**31**
$(Pb/Tl)Sr_2CuO_{5\pm\delta}$[80]	3.736(1)	9.022(3)	P4/mmm	**60**
1 2 $TlBa_2CaCu_2O_7$[73]	3.8566(4)	12.754(2)	P4/mmm	**103**
$(Pb/Sr)Sr_2(Y/Ca)Cu_2O_{7-\delta}$[9]	3.817	11.907	P4/mmm	**100**
$(Pb/Tl)Sr_2CaCu_2O_7$[81]	3.80	12.05	P4/mmm	**85**
1 3 $TlBa_2Ca_2Cu_3O_9$[82]	3.843(2)	15.871(3)	P4/mmm	**116**
$(Pb/Tl)Sr_2Ca_2Cu_3O_9$[77]	3.803(1)	15.232(7)	P4/mmm	**120**

The $M_mA_2R_{n-1}Cu_nO_{m+2n+2}$ series (m = 2,3)

The crystal structures of the m = 2,3 members in series III are similar to those of the m = 1 compounds except that there are two or three [MO] layers between the {AO} layers instead of one (figures 2.4.2 and 2.4.3). Five different phases belonging to the $M_mA_2R_{n-1}Cu_nO_{m+2n+2}$ series (m = 2,3) have been listed in table 2.4.2. The typical layer sequences of these phases are

2-1 phase (or Tl, Bi-2201): $[^6MO.^6MO]\{^9AO.^6CuO_2.^9AO\}$

2-2 phase (or Tl, Bi-2212): $[^6MO.^6MO]\{^9AO.^5CuO_2.^8R.^5CuO_2.^9AO\}$

2-3 phase (or Tl-2223): $[^6MO.^6MO]\{^9AO.^5CuO_2.^8R.^4CuO_2.^8R.^5CuO_2.^9AO\}$

3-1 phase (or Pb-2202): $[^5MO.^2Cu.^5MO]\{^9AO.^6CuO_2.^9AO\}$

3-2 phase (or Pb-2213): $[^5MO.^2Cu.^5MO]\{^9AO.^5CuO_2.^8R.^5CuO_2.^9AO\}$

The existence of the 2-1 phase was first shown in the Bi cuprate system[83], then in the Tl cuprates. The crystal structure of the 2-1 phase contains $[MO]_2$ double layers and $\{CuO_2\}$ single layers sandwiched by two {AO} layers. Bi-2201 and 2212 are the only two phases in the Bi cuprate system which can be prepared in single phase form without addition of Pb. Structural modulations in these phases, which may result from strain due to lattice mismatch and to lone pair induced distortions, are more severe than in the Tl analogue as shown by stronger satellite reflections in the electron diffraction patterns[84].

A T_c of 81K in the Tl-2212 phase was first reported by Sheng and Hermann[85]. The crystal structure of the Tl-2212 phase can be derived from that of $Ba_2YCu_4O_8$ by replacing {Y} and $[CuO]_2$ with {Ca} and $[TlO]_2$ double layers, respectively. Although the compound has a high symmetry (body-centred tetragonal), the oxygens in the $\{CuO_2\}$ and $[TlO]_2$ layers are shifted away from their special crystallographic position *4e* to more general ones *8g* and *16n* of space group I4/mmm[28]. The crystal structure of Bi-2212 is orthorhombic. Various space groups have been assigned to this phase: A2aa[30], Amaa[86], Bbmb[87] and Fmmm[88] owing to the complex defects in this compound: displacement of Bi or O atoms, substitutions among Sr, Ca and Bi[89], cation vacancies, and interstitial oxygens inserted at approximately every fifth unit cell[90]. Incommensurate structural modulations are frequently observed in both Tl-2212 and Bi-2212.

Among the known 2-3 phases, Tl-2223 is the only one reported thus far as a single phase. It was first identified by Hazen et al.[91] who reported a T_c of 120K. The crystal structure of Tl-2223 contains $[TlO]_2$ double layers and three consecutive CuO_2

layers that are separated by two calcium layers (figure 2.4.2c). The same symmetry (I4/mmm), oxygen displacement and incommensurate structural modulations existing in 2-2 phase have been observed in the 2-3 phase. Bi-2223 usually exhibits intergrowth with Bi-2212 as evidenced by two superconducting transitions at 110K and 80K in resistivity measurements[92]. Crystallographic information is not available due to the poor sample quality. The crystal structures of Pb-2202 and Pb-2213 (m = 3) are similar to those of Tl-2201 and Tl-2212 (m = 2) except that an extra oxygen-depleted Cu layer is intercalated between the two $[MO]_2$ layers in the former cases. Their T_c and orthorhombic symmetry are similar to the corresponding Bi cuprates, while the crystal symmetry for the Tl cuprates is tetragonal.

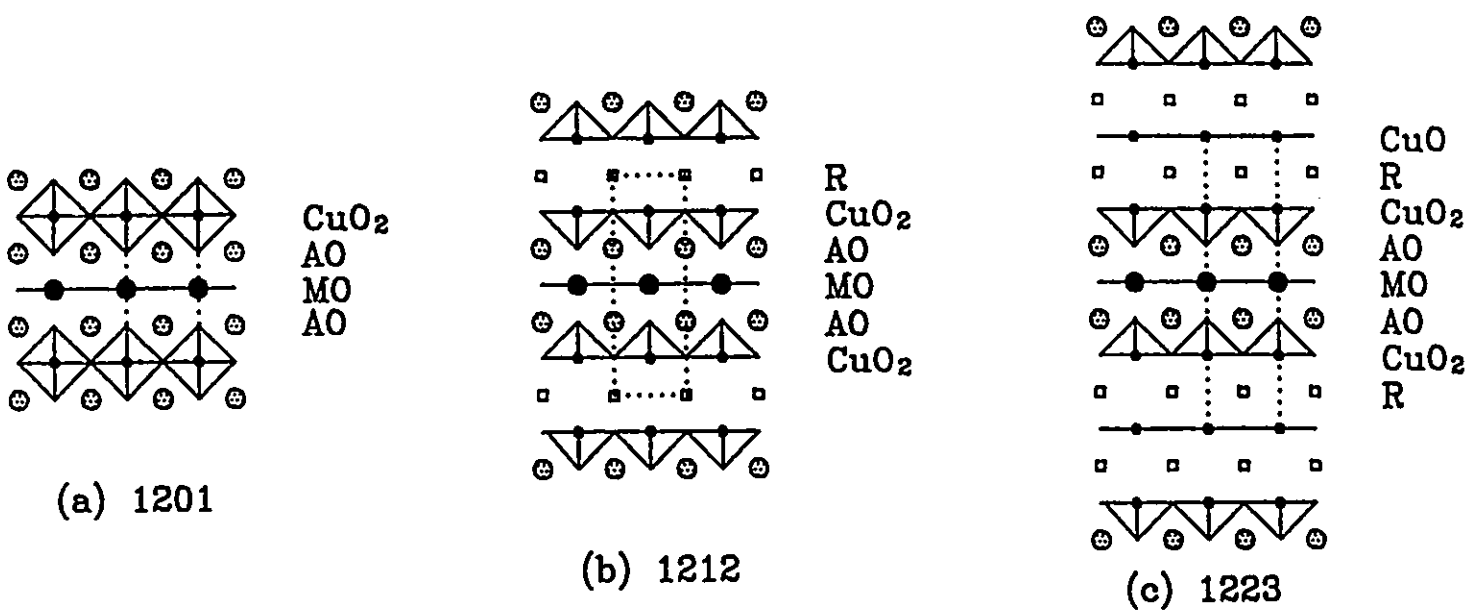

Figure 2.4.1 Series III - $M_mA_2R_{n-1}Cu_nO_{m+2n+2}$ (m = 1)

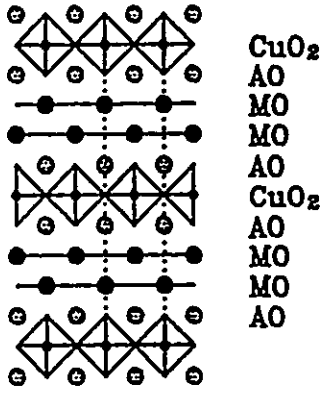

(a) 2201

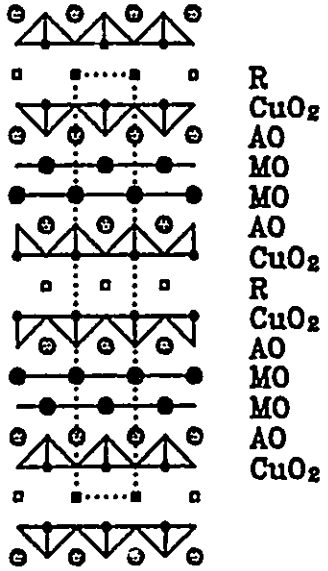

(b) 2212

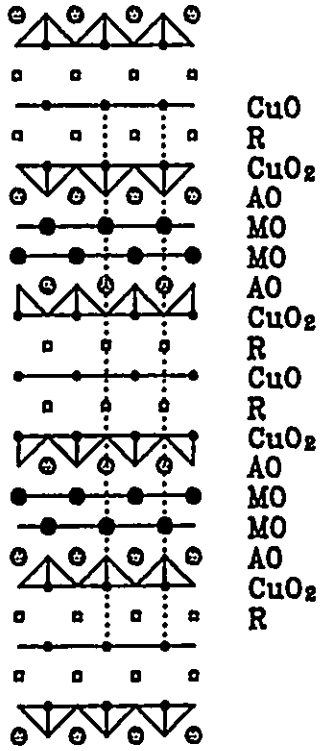

(c) 2223

Figure 2.4.2 Series III - $M_mA_2R_{n-1}Cu_nO_{m+2n+2}$ (m = 2)

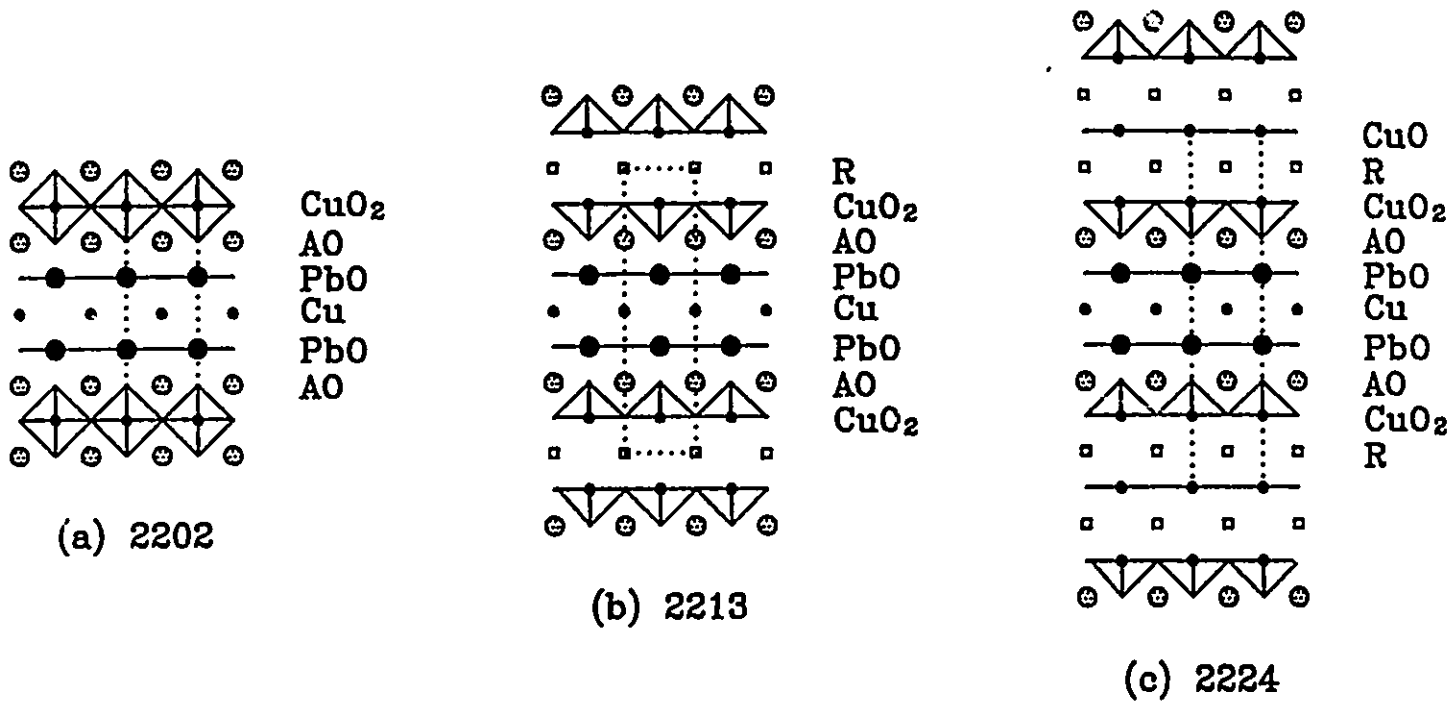

Figure 2.4.3 Series III - $M_mA_2R_{n-1}Cu_nO_{m+2n+2}$ (m = 3)

Table 2.4.2 The $M_mA_2R_{n-1}Cu_nO_{m+2n+2}$ series (m = 2,3)

m	n	$M_mA_2R_{n-1}Cu_nO_{m+2n+2}$	a(Å)	b(Å)	c(Å)	S.G.	T(K)
2	1	$Tl_2Ba_2CuO_6$ [93]	3.866(1)		23.239(6)	I4/mmm	70
		$Bi_2Sr_2CuO_6$ [93]	5.362(3)	5.374(1)	24.622(6)	Amaa	9
2	2	$Tl_2Ba_2CaCu_2O_8$ [94]	3.8550(6)		29.318(4)	I4/mmm	110
		$Bi_2Sr_{2-x}CaCu_2O_8$ [30]	5.4095(4)	5.4202(4)	30.930(3)	A2aa	85
2	3	$Tl_2Ba_2Ca_2Cu_3O_{10}$ [95]	3.8503(6)		35.88(3)	I4/mmm	125
3	1	$Pb_2(Sr/La)_2Cu_2O_{6+\delta}$ [10]	5.333(2)	5.421(2)	12.609(6)	$P22_12$	34
3	2	$Pb_2Sr_2RCu_3O_{8+\delta}$ [96]	5.383(1)	5.423(1)	15.765(2)	Pmmm	84

2.5 Crystal chemical constraints

Commensurability

By projecting the crystal structure of a typical copper oxide superconductor along the c-axis, one should see the square lattices of {CuO}, {AO} or [MO]. The edge length (a_0) of the CuO squares, or the a-axis of a primitive unit cell[c] falls into a narrow range: 3.78 to 3.86Å for a p-type superconductor and more than 3.94Å for an n-type. Owing to the principle of intergrowth, the {AO} layers adjacent to $\{CuO_2\}$ must be commensurate with the edge length of $\{CuO_2\}$, and the in-plane dimension of the layers next to the {AO}, for instance the [MO] layers should be commensurate with

[c] an average length of a and b axes for the orthorhombic cases is adopted here for brevity.

both {AO} and {CuO} ... etc. The relationship between the dimensions of {AO} and $\{CuO_2\}$ layers is such that $\sqrt{2}(A\text{-}O) = 2(Cu\text{-}O)$ (here A-O is the bond distance between atom A and oxygen). An integrated dimensional effect of all the layers in the unit cell determines the length of a_0. Since the in-plane layer dimension mainly depends on the metal size which varies from layer to layer, some of the layers in the unit cell will be stretched and others, compressed. The tension in the stretched layers, which can be estimated by calculating the bond valence sum (BVS), can be relaxed by several mechanisms, such as reducing the inter-layer spacing, moving cations off centre of their coordination sphere, adding interstitial oxygens to compress or buckle the layers ... etc.[97]

Preferred coordination number

Partial chemical substitution is one of the main features in the high-T_c copper oxide superconductors. For example, Ba^{2+} and Sr^{2+} in {AO} layers can be partially substituted by Bi^{3+}, Pb^{4+} and R^{3+}; Cu^{2+} in $\{CuO_2\}$ by Ni^{2+}, Co^{2+}, Fe^{3+}, Al^{3+} .....; Ca^{2+} in {R} by R^{3+}, Tl^{3+}, and Bi^{3+}; and Tl^{3+}, Bi^{3+}, Pb^{4+} in [MO] by Cu^{2+}, Sr^{2+}, Ca^{2+} ... etc. The plausibility and degree of chemical substitution are not only governed by atomic size, but also depend on the preferred coordination number of those ions involved in the substitution. The cations in {AO} layers usually are those elements preferring a high coordination number (CN = 9, 10 or 12); those in {R} layers, CN = 8; and for those in [MO], CN = 2, 4, 5 or 6. Since there are a considerable number of inorganic crystal structures which have been collected in the Inorganic Crystal Structure Database (ICSD)[98] and the preferred coordination numbers for various cations has been calculated[99], this is certainly a valuable tool in elucidating the crystal chemistry of the

known high-T_c superconductors and in designing new ones.

Local charge neutrality

Besides the size and coordination number of the cation, local charge neutrality is another crystal chemical constraint. By this it is meant that the electric charge on a cation in a crystal lattice has to be compensated by the opposite charges from its neighbour anions. By extending the idea to the layered structures, the statement becomes: the residual charge on a metal oxygen layer must be balanced by the same amount of opposite charge from the adjacent layers. Combining the layer sequence notation established in former sections with the concept of local charge neutrality, one can calculate the total charges (Q) in the layered copper oxide superconductors. Taking $La_{2-x}Sr_xCuO_4$ as an example, the residual charge in two $\{La^{III}O^{-II}\}$ layers can be calculated to be +2 by neglecting a small amount of Sr^{2+} substitution (x=0.15), while the charge in the $\{Cu^{II}O^{-II}_2\}$ layer should be -2. A total charge (Q) of zero can be obtained by summing up the residual charges of all the layers in the unit cell. Similarly, a Q value of -1 has been found in all the phases in series II ($M_mA_2R_{n-1}Cu_nO_{4n-\delta}$) and for the m = 1 phases in the Tl-Ba-Ca-Cu-O and Bi-Sr-Ca-Cu-O systems, while Q=0 for the rest of the phases in the $M_mA_2R_{n-1}Cu_nO_{m+2n+2}$ series. Some half-integer charges occur in the Pb cuprate systems due to the substitutions of Pb^{4+} by Cu^{2+}, or Sr^{2+} by La^{3+} (see Appendix for the calculations).

The concept of local charge neutrality is not only useful in designing new phases but also very important to synthetic chemistry since the crystal growth is a process of depositing layers of ions with alternating charges onto a crystal surface.

CHAPTER 3

CRYSTAL CHEMISTRY OF $Pb_2Sr_2RCu_3O_8$

3.1 Evolution of the crystal structure of $Pb_2Sr_2YCu_3O_8$

From the view point of crystal chemistry, the crystal structure of $Pb_2Sr_2YCu_3O_8$ can be understood as a structural evolution which progresses from series I ($A_2R_{n-1}Cu_nO_{3n+1}$) to series II ($M_mA_2R_{n-1}Cu_nO_{4n-\delta}$) then series III ($M_mA_2R_{n-1}Cu_nO_{m+2n+2}$):

$$\begin{array}{llll} Sr_{1-x}Nd_xCuO_2 & Sr_2YCu_3O_y & Bi_2Sr_2CaCu_2O_8 & Pb_2Sr_2YCu_3O_8 \\ CaCuO_2 & Ba_2YCu_3O_6 & Tl_2Ba_2CaCu_2O_8 & Pb_2Ba_2YCu_3O_8 \end{array}$$

$CaCuO_2$ has been a hypothetical compound for several years and is predicted to be tetragonal with a = 3.85, c = 3.16Å[51]. The compound is iso-structural with the recently-discovered electron superconductor $Sr_{1-x}Nd_xCuO_2$. Its crystal structure is simply composed of oxygen-free R layers sandwiched between infinite CuO_2 sheets. If we move all of the apical oxygens of the CuO_5 pyramids in $Ba_2YCu_3O_6$, a series II compound, from *(0,0,z)* to *(0,½,0)*, both the crystal structure and stoichiometry of $(Ba_2Y)Cu_3O_6$ resemble those of $CaCuO_2$. The ionic radius of Y is comparable to that of Ca, but Ba ions are larger than both Y and Ca in size and require larger sites and higher coordination number (i.e. C.N. ≥ 9). This is the driving force for the oxygen ordering in $Ba_2YCu_3O_{7-\delta}$. As a consequence, two distinct Cu ions, Cu^{2+} in square

pyramidal coordination and Cu^{+}, in linear-coordination are created. $Sr_2YCu_3O_y$ is an analogue of $Ba_2YCu_3O_6$, which can crystallize in the same structure as that of $Ba_2YCu_3O_6$ only under high oxygen pressure (7GPa) and high temperature (1380°C)[54,69]. The crystal structure of $Sr_2YCu_3O_y$ is not so stable as that of $Ba_2YCu_3O_6$ due to the smaller ionic radius of Sr^{2+} (1.45Å) relative to Ba^{2+} (1.61Å). However, if the Y layers and the CuO chains in $Sr_2YCu_3O_y$ are replaced by Ca and two BiO layers respectively, the crystal structure can be stabilized and has a stoichiometry of $Bi_2Sr_2CaCu_2O_8$, a series III compound. As mentioned earlier that this compound is much more difficult to prepare in single phase form than its analogue $Tl_2Ba_2CaCu_2O_8$ due to serious oxygen disordering caused by lone pair electrons of the Bi^{3+} ions. Pb^{2+}, a neighbour of Bi^{3+} in the periodic table, also has lone pairs. The two PbO layers in $Pb_2Sr_2YCu_3O_8$ can not accommodate each other until a Cu layer is intercalated in between. $Pb_2Sr_2YCu_3O_8$ appears to be much easier to prepare in single phase form than $Bi_2Sr_2CaCu_2O_8$ and $Pb_2Ba_2YCu_3O_8$. The crystal structure of $Pb_2Sr_2YCu_3O_8$ resembles that of the well-studied $Ba_2YCu_3O_{7-\delta}$ except for the insertion of a PbO layer between the AO (A=Sr or Ba) and Cu^{I} layers which makes it a good candidate for comparative studies.

3.2 Structural relationships among various lead cuprates

Six superconducting lead cuprates have been reported thus far with T_c's, ranging from 30 to 100K. Many efforts have been made to search for new lead cuprate phases[100,101,102,103]. Lead cuprate superconductors have the Aurivillius-type crystal structure. Many similarities exist among the various lead

cuprates. For example by removing the {R} and one of the $\{CuO_2\}$ layers in the Pb-2213 structure, one can obtain $Pb_2(Sr/La)_2Cu_2O_{6+\delta}$[10,11], or the 2202 phase. Superconductivity ($T_c = 38K$) is believed to be induced in this phase by the substitution for Sr^{2+} by La^{3+}. The crystal structure of the 2213 phase can be altered by removing the [PbO] and [Cu] layers. The phase thus obtained is 1212. In one further step, the {R} and one of the $\{CuO_2\}$ layers in the 1212 phase can be eliminated. The new phase is 1201, or $(Pb/Cu)(Sr/La)_2CuO_{4+\delta}$[12], which has a superconducting transition temperature of 31K. However, there are three derivatives of the lead cuprates; $PbBa(YSr)Cu_3O_{8-\delta}$ (the 0223 phase, $T_c = 50K$)[16,106], $(Pb/Cu)(Sr/Eu)_2(Eu/Ce)_2Cu_2O_y$ (the 1222 phase, $T_c = 25K$)[14,104] and $Pb_2Sr_2LnCeCu_3O_{10+\delta}$[105] (the 2223 phase) which are structurally somewhat different from the lead cuprates discussed above. The crystal structure of the 0223 phase is still a point of debate. Rouillon et al.[106] proposed a crystal structure which consisted of an alternate stacking of the RS-unit with single metal oxygen layer and the P-unit with three metal oxygen layers. Tokiwa et al.[16] believe that the crystal structure of the 0223 phase is a derivative of the 2213 phase, in which one of the [PbO] layers is missing. They also suggested a domain structure model according to observations made using transmission electron microscopy (TEM). Later, Rouillon et al. re-examined the 0223 phase by neutron powder diffraction and concluded that the correct space group for this phase is I4mm[13]. The 1222 phase, although a p-type superconductor, has two 'fluorite-type' layers sandwiched by two CuO_2 layers which structurally resemble the n-type superconductor $Nd_{2-x}Ce_xCuO_4$. The 2223 phase is a member of a nonsuperconducting lead cuprate series with intergrowth of fluorite and perovskite layer-structures and a chemical formulae of $Pb_2Sr_2(Ln,Ce)_nCu_3O_{6+2n+\delta}$ $(n = 2,3,4,...)$[107]. Although these

compounds have not been well characterized, they may imply that there exists a much richer crystal chemistry in the lead cuprate family than in the other high-T_c superconductors.

3.3 Substitution Chemistry of $Pb_2Sr_2RCu_3O_{8+\delta}$

Ca^{2+} is an ideal candidate for substituting the R ion in $Pb_2Sr_2RCu_3O_{8+\delta}$ for the following reasons: i) it is similar in size, ii) it prefers an eight-coordinate environment and more importantly, iii) the oxidation state of $+2$ is necessary for hole-doping the CuO_2 conduction planes. Experiments show that partial Ca-substitution can be performed for nearly all the rare-earths and Y in $Pb_2Sr_2R_{1-x}Ca_xCu_3O_{8+\delta}$ polycrystalline samples thereby inducing superconductivity in the compounds[7]. The substitution range is limited from $x=0$ to 0.8. The end member, $Pb_2Sr_2CaCu_3O_7$, is not stable due to too many oxygens being withdrawn from the crystal structure in order to maintain charge neutrality.

Amador et al.[108] studied Ni-substituted $Pb_2Sr_2YCu_3O_8$. The structure refinement result shows that about 40% of Cu^{2+} in the CuO_2 planes are substituted by Ni^{2+} while none is substituted in the oxygen-free Cu layers. No magnetic ordering of Ni^{2+} was observed down to 1.5K by powder neutron diffraction. The Sr in the same parent compound has also been substituted by Ba without severe modification of the crystal structure[103]. Naturally, the substituted compounds in both cases are nonsuperconducting since no carrier-doping in the CuO_2 plane is involved in these substitutions and the parent compound is nonsuperconducting as well.

CHAPTER 4

SYNTHESIS AND CHARACTERIZATION OF $Pb_2Sr_2RCu_3O_8$

Successful synthesis of $Pb_2Sr_2(Y/Ca)Cu_3O_{8+\delta}$ was first reported by Cava et al.[7], and then confirmed by Subramanian et al.[101] The original report indicated that the preparative conditions for this system were considerably more stringent than for the other families of copper oxide superconductors. The compound can be synthesized only under mildly reducing conditions and not in air or oxygen below 900°C. The crystals were found to display a range of T_c values from 10 to 70K. As with most of the single crystals of the high-T_c superconductors reported in recent years, these crystals were synthesized using a CuO-rich flux, from which they had to be separated mechanically, a process which is both destructive and incomplete. To date, the 2213 phase of the superconducting lead cuprates has been grown in single crystal form using various combinations of PbO, CuO, PbF_2 and $PbCl_2$ fluxes[7,101,108,110]. The crystal growth method presented in this dissertation is a new approach to the synthesis of Cu-based superconducting single crystals; a growth procedure free of CuO flux, whereby the crystals can be separated non-destructively from the melt using an organic solvent. The crystals produced by this method are considerably thicker along the c-direction than typical crystals of $Ba_2YCu_3O_{7-\delta}$ or $Bi_2Sr_2CaCu_2O_8$ and can be synthesized in either a pure nitrogen atmosphere or in air. The best crystals showed

$T_c > 80K$ and were of sufficient size and of convenient habit to allow determination of the anisotropy in the basic superconducting parameters such as penetration depth[111], coherent length and upper critical fields[112] using magnetization and optical measurements.

4.1 Various reported sample preparation methods

As one of the starting materials, PbO, has a melting temperature of 880°C and is highly volatile at high temperature, the preparation of the lead cuprate polycrystalline samples requires a compromise in temperature (around 880°C) and reaction time in order to reduce lead evaporation. A nitrogen atmosphere is crucial for the formation of the 2213-phase to prevent oxidation of Pb^{2+} and Cu^{1+}.

Polycrystalline samples and thin films

Polycrystalline samples of the 2213-phase are usually prepared by a two-step method[7,113,114]. An oxide precursor is made by preheating stoichiometric CuO, rare-earth oxides and alkaline earth carbonates at 950°C for 12 hours in air. Then, the precursor is well mixed with PbO and calcined at a temperature between 830° and 920°C under N_2 (1-2% O_2). The solid state reaction takes about 1 to 16 hours depending on the maximum temperature (T_{max}). Some stable compounds, such as $Pb_2Sr_2YCu_3O_8$ can be made within 1 hour at 900°C. A precursor is preferable for the polycrystalline sample preparation in order to avoid the formation of impurity phases, such as $SrPbO_3$, $CaPbO_3$ ... etc. However, direct synthesis of a single phase compound is also possible[102].

Thin films of $Pb_2Sr_2(R/Ca)Cu_3O_{8+\delta}$ (R = Yb or Y) have been epitaxially grown *in situ* on MgO (*100*) substrate using rf-magnetron sputtering by Adachi et al.[115] In order to prevent the problem of Pb-loss during the film growth process, a Pb-rich target was made with a cation ratio of Pb:Sr:R:Ca:Cu = 5:2:(1-1.5):0.4:(2.7-3.3) by a procedure similar to those described above for the preparation of polycrystalline samples. The films were deposited on polished (*100*) wafers of MgO single crystals with a substrate temperature approximately 550°C under both pure argon or a mixture of argon with a small amount of oxygen. A deposition rate of 2Å/sec was achieved under a gas pressure of 0.5 Pa and rf (13.56 MHz) input of 100W for an erosion area about 16cm^2 on the target. The deposited films with a final thickness of 3,000Å were then cooled to room temperature within 20 minutes under the same atmosphere. The resulting film of $Pb_2Sr_2(Yb/Ca)Cu_3O_{8+\delta}$ is c-oriented and has a c-axis length of 15.75Å deduced by x-ray diffraction, an onset T_c of 75K and zero-resistivity below 60K. The critical current density of the film was measured to be $10^4A/cm^3$ at 50K. Post-annealing of the films under argon or nitrogen showed no significant improvement in the electronic properties. Annealing in air or oxygen destroyed the superconducting properties of the films.

Single crystals

Single crystals of the 2213-phase are prepared by a flux method. Cava et al.[7] used a two-step procedure similar to the preparation of polycrystalline samples, except that extra PbO and CuO were added to the crystal growth system as flux and the synthetic temperature was about 100°C higher than that for the polycrystalline samples. Crystals of up to 1x1x0.1mm^3 were formed. Subramanian et al.[101] grew

single crystals simply by sealing the CuO-rich reactants in a gold tube and firing them at 950°C for 12-48 hrs. The advantages of this method are i) the PbO evaporation at high temperature is reduced, and ii) extra oxygen in the crystal growth system can diffuse through the porous wall of the gold tube at high temperature. However, crystals of (Pb/Cu)Sr_2(Y/Ca)$Cu_2O_{7-\delta}$ (1212-phase) were found to co-exist with the 2213 crystals in the growth system due to a part of the Pb ions being oxidized into their 4+ oxidation state. Capponi and Korczak et al.[116,110] modified the two-step method by adding a few percent of additives (PbF_2 or $PbCl_2$) into the PbO flux. The maximum crystal size obtained was 2x2x0.1mm^3, the larger dimensions, presumably, are due to a deeper supercooling after the addition of the lead halides. Hibiya et al.[117] studied a complicated pseudo-ternary phase diagram of $Ba_2YCu_3O_{7-\delta}$-CuO-PbO/B_2O_3. The crystals of $Pb_2Ba_2YCu_3O_8$ were grown as one of several products ——— $BaPbO_3$, $Ba_3Al_2O_6$ and CuO in the alumina crucibles under N_2 (1% O_2) atmosphere. Attempts to dope Ca^{2+} into the Y-sites in the $Pb_2Ba_2YCu_3O_8$ crystals were not successful. The maximum crystal size of 5x5x0.03mm^3 is enhanced by a large amount of flux charge (100-150g) and the acidic B_2O_3 flux where $B_4O_7^{2-}$ clusters may form and attain oxygens at high temperature.

The preparative conditions for the 2213-phase by the various flux methods described above are considerably more stringent than for the other families of copper-oxide superconductors. Growth of this material in air or oxygen is not possible, and the compound can be synthesized only under mildly reducing conditions (N_2, 1-2% O_2). The crystals were found to display a range of T_c. As with most of the high-temperature superconducting copper oxides reported in recent years, the crystals are often synthesized using a CuO-rich flux, from which they have to be separated

mechanically. In addition, typical crystals of $Pb_2Sr_2RCu_3O_{8-\delta}$ grown by the above methods are dimensionally thin in the c-direction, making separation of the crystals from the melt difficult. The plate-like crystals are also undesirable for certain physical property measurements such as neutron scattering, investigations of anisotropy ... etc.

4.2 Preparation of polycrystalline samples

Both stoichiometric and nonstoichiometric Ca-free polycrystalline samples of $Pb_2Sr_2RCu_3O_8$ (R = La, Ce, Pr, Nd, Sm, Eu, Gd, Tb, Dy, Ho, Er, Tm, Yb, Lu and Y) were prepared using a fast solid state synthesis technique. Appropriate amounts of PbO, R_2O_3[d], CuO and $SrCuO_2$ were carefully weighed, well-ground and pelletized. Pt boats were used to hold the pellets and left in the cold zone of a quartz-tube furnace under N_2 or air for about 20 minutes before being pushed into the hot zone with a maximum temperature (T_{max}). After a 1 to 12 hour reaction period, the samples were quenched to room temperature by pulling the quartz tube out of the furnace under the same atmosphere. Ca-doped polycrystalline samples can also be prepared by this technique. The values of T_{max} and sample quality for the Ca-free samples with various rare-earths are given in table 4.2.

---

[d] CeO_2, Pr_6O_{11} and Tb_4O_7 were used in the cases of R = Ce, Pr and Tb, respectively. The same oxides were employed as the starting materials in the crystal growth discussed in the successive section.

Table 4.2 Maximum temperatures (T_{max}) for the synthesis of Ca-free $Pb_2Sr_2RCu_3O_8$ polycrystalline samples and comments on sample quality. Most of these samples were prepared in air except for those marked with a '*', which were made under N_2.

R	T_{max}(°C)	Comments
La	860*	almost single phase
Ce	840*	almost single phase
Pr	890	single phase
Nd	870	single phase
Sm	870	single phase
Eu	870	single phase
Gd	900	single phase
Tb	830*	single phase
Dy	900	single phase
Ho	910	single phase
Er	860	almost single phase
Tm	860*	very small amount of impurity
Yb	860*	very small amount of impurity
Lu	860*	small amount of impurity present
Y	880	single phase

4.3 PbO/NaCl flux growth method

Single crystals of Ca-doped $Pb_2Sr_2(R/Ca)Cu_3O_{8+\delta}$ (R = Nd, Sm, Gd, Dy, Er, Tm, Yb, Lu and Y) and Ca-free $Pb_2Sr_2RCu_3O_8$ (R = La, Pr, Nd, Sm, Eu, Gd, Tb, Dy, Ho and Y) were synthesized using a modification of the two-step flux growth method. More than a hundred crystal growth runs have been conducted on various kinds of 2213 crystals in order to obtain those with best crystal quality, physical properties and large size. An optimized recipe is as follows: the precursors of $Sr_2(R/Ca)Cu_3O_y$ with an R/Ca ratio of 1/1 (or $Sr_2RCu_3O_y$ in the case of Ca-free crystals) were prepared by firing stoichiometric amounts of well-ground $SrCO_3$, $CaCO_3$, R_2O_3 and CuO powders at 950°C for 12 hours (more than 97wt% of the carbonates are decomposed). They were then reground, combined with PbO and NaCl flux in the molar ratio of $Sr_2(R/Ca)Cu_3O_y$:PbO:NaCl = 1:4:30 and loaded into covered platinum crucibles. A vertical tube furnace employing a flow of N_2 gas was used to grow single crystals of $Pb_2Sr_2(Y/Ca)Cu_3O_{8+\delta}$ using the following temperature program:

$$200°C \xrightarrow[4hrs]{} 980\sim1050°C/1hr \xrightarrow[30\sim60hrs]{5\sim10°C/hr} 760°C \xrightarrow[4hrs]{} 200°C$$

The growth parameters for Ca-doped crystals with different starting Y/Ca ratios, rare-earth substitutions and Ca-free 2213 crystals are listed in tables 4.3.1, 4.3.2 and 4.3.3, respectively. The maximum synthetic temperature (T_{max}) for the Ca-doped $Pb_2Sr_2(Y/Ca)Cu_3O_{8+\delta}$ crystals is roughly proportional to the starting Y/Ca ratio. The yield of $Pb_2Sr_2(Y/Ca)Cu_3O_{8+\delta}$ crystals obtained from the starting material can be as high as 40%. The $Pb_2Sr_2(Y/Ca)Cu_3O_{8+\delta}$ crystals grown by this method have a typical dimension of 1x1x0.25mm (see figure 4.3.1, the scale shown in the photograph is in

tenths of millimetres). The dc resistivity and magnetic flux exclusion measurements (lower inset of figure 4.3.2) on one of the $Pb_2Sr_2(Y/Ca)Cu_3O_{8+\delta}$ crystals show that a superconducting transition occurs near 84K and is less than 1K in width (upper inset).

Table 4.3.1 Crystal growth parameters for $Pb_2Sr_2(Y/Ca)Cu_3O_{8+\delta}$ and comments on crystal size.

Y/Ca ratio	T_{max} (°C)	Comments
0.00/1.00	975	no crystals
0.15/0.85	985	no crystals
0.30/0.70	995	a few small crystals
0.35/0.65	995	crystals
0.40/0.60	1000	many large crystals
0.45/0.55	1000	many large crystals (up to 1x1x0.5mm^3)
0.50/0.50	1000	many large crystals
0.55/0.45	1015	many large crystals
0.60/0.40	1015	many large crystals
0.70/0.30	1045	many crystals
0.85/0.15	1060	many crystals
1.00/0.00	1060	medium sized crystals

Table 4.3.2 Maximum temperatures (T_{max}) for the crystal growth of Ca-doped $Pb_2Sr_2(R/Ca)Cu_3O_{8+\delta}$.

R	Nd	Sm	Gd	Dy	Y	Er	Tm	Yb	Lu
Radius(Å)[118]	1.109	1.079	1.053	1.027	1.019	1.004	0.994	0.985	0.977
T_{max}(°C)	1050	1000	1000	1025	995	1040	970	960	970

Table 4.3.3 Maximum temperatures (T_{max}) for the crystal growth of Ca-free $Pb_2Sr_2RCu_3O_8$ and comments on crystal quality and size.

R	T_{max}(°C)	Comments
La	1015	small, extremely thin-plates (a few μm)
Ce	985	small, a few large, plate-like crystals
Pr	1040	plate-like crystals
Nd	1040	large, thick crystals
Sm	1010	crystals up to ~4x4x1mm^3 were obtained
Eu	1000	fairly large, thick crystals of good quality
Gd	1020	large, thick crystals (~1x1x0.5mm^3)
Tb	1040	small, a few large, plate-like crystals
Dy	1030	crystals of good quality
Ho	1040	crystals formed but of poor quality
Y	1060	medium sized crystals (~0.5x0.5x0.2mm^3)

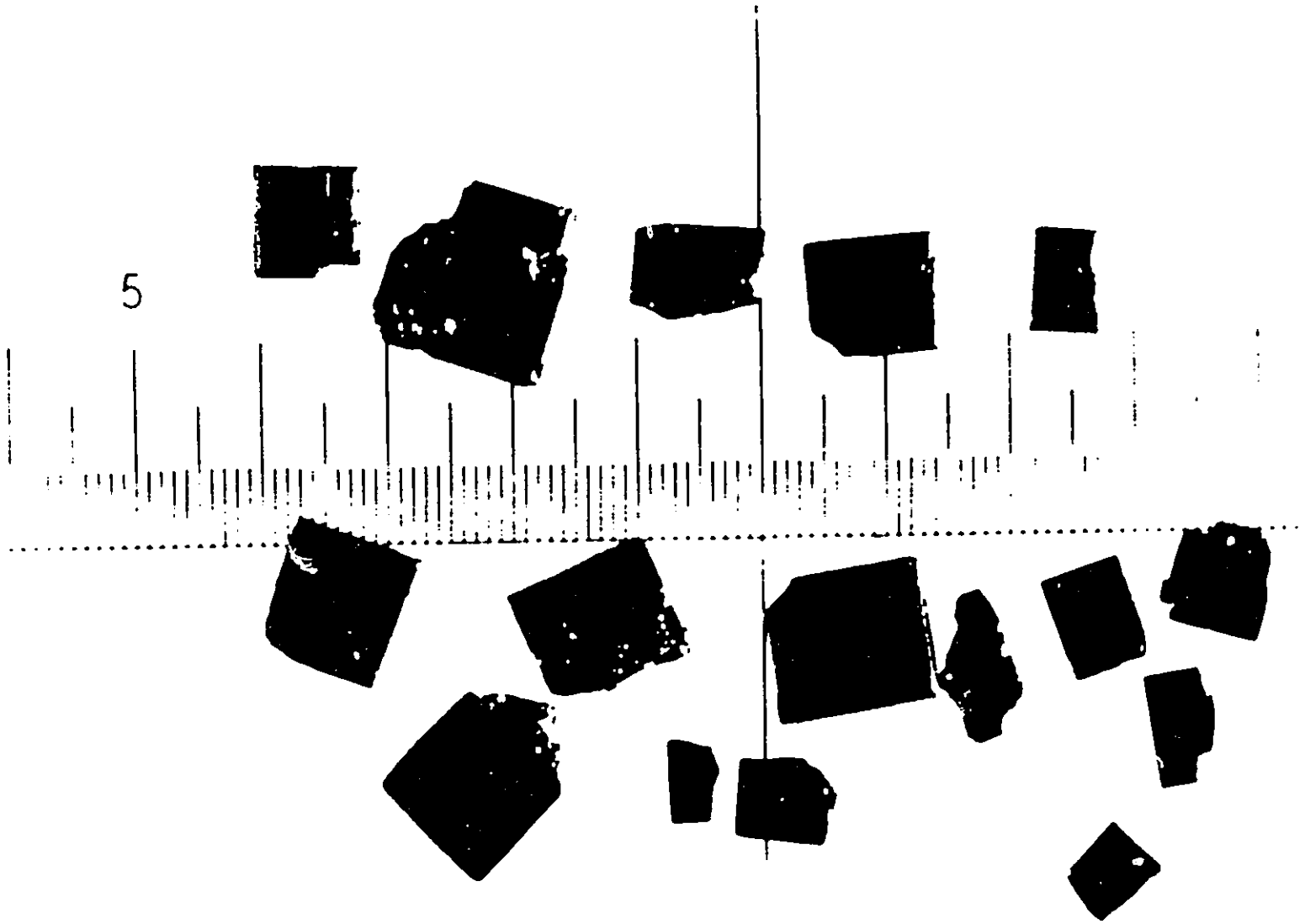

Figure 4.3.1 Typical $Pb_2Sr_2(Y/Ca)Cu_3O_{8+\delta}$ crystals grown from a PbO/NaCl flux.

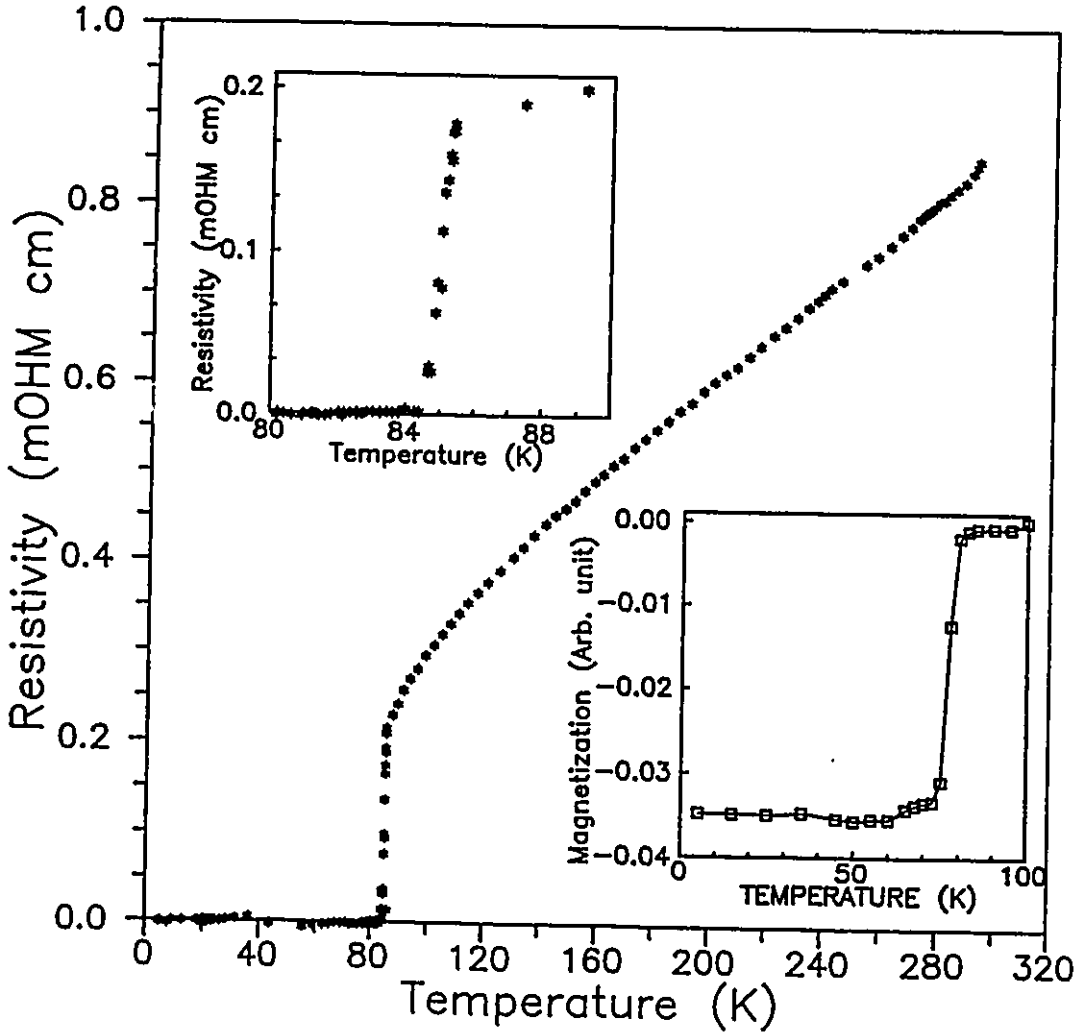

Figure 4.3.2 The dc resistivity measurement for a $Pb_2Sr_2(Y/Ca)Cu_3O_{8+\delta}$ crystal. The upper inset showing a magnified view of a superconducting transition while the lower one, the result of flux exclusion measurement on another 2213 crystal.

4.4 Separation and annealing

A NaCl layer, which is easily removed mechanically, lines the top of the crucible. The melt below contains the crystals of $Pb_2Sr_2RCu_3O_8$ embedded in a PbO-rich flux mixture. The black crystals can be extracted undamaged from the PbO flux with methanol solvent in an ultrasonic bath. Distilled water is even more effective in dissolving the NaCl flux at the cost of visible damage to the surface of the crystals possibly caused by a reaction with dissolved chlorine.

Although the $Pb_2Sr_2(Y/Ca)Cu_3O_{8+\delta}$ crystals grown from the PbO/NaCl flux are superconducting as grown, a post-annealing in N_2 at 600°C for 40 hours has been found to improve the sharpness of the superconducting transition. Various annealing conditions were tried: annealing in oxygen at 400°C for 12 hours, in nitrogen at various temperatures ranging from 400°C to 850°C, the best condition found is to anneal the crystals in nitrogen at 600°C for two days or longer. Figure 4.4.1 shows the results of the magnetic flux exclusion measurements for the same crystal of $Pb_2Sr_2(Y/Ca)Cu_3O_{8+\delta}$, annealed in nitrogen at 400°C, 600°C, 750°C and 850°C for 12 hours, respectively. The magnetic field used was ~50 Oe, and the mass of the crystal was 0.31mg. The surfaces of crystals annealed in N_2 above 600°C showed a visible deterioration although the bulk crystals remained superconducting. Figure 4.4.2 shows the field dependence of the flux exclusion of a $Pb_2Sr_2(Y/Ca)Cu_3O_{8+\delta}$ crystal (mass 0.61mg) at 5K. A near-ideal Meissner effect is observed.

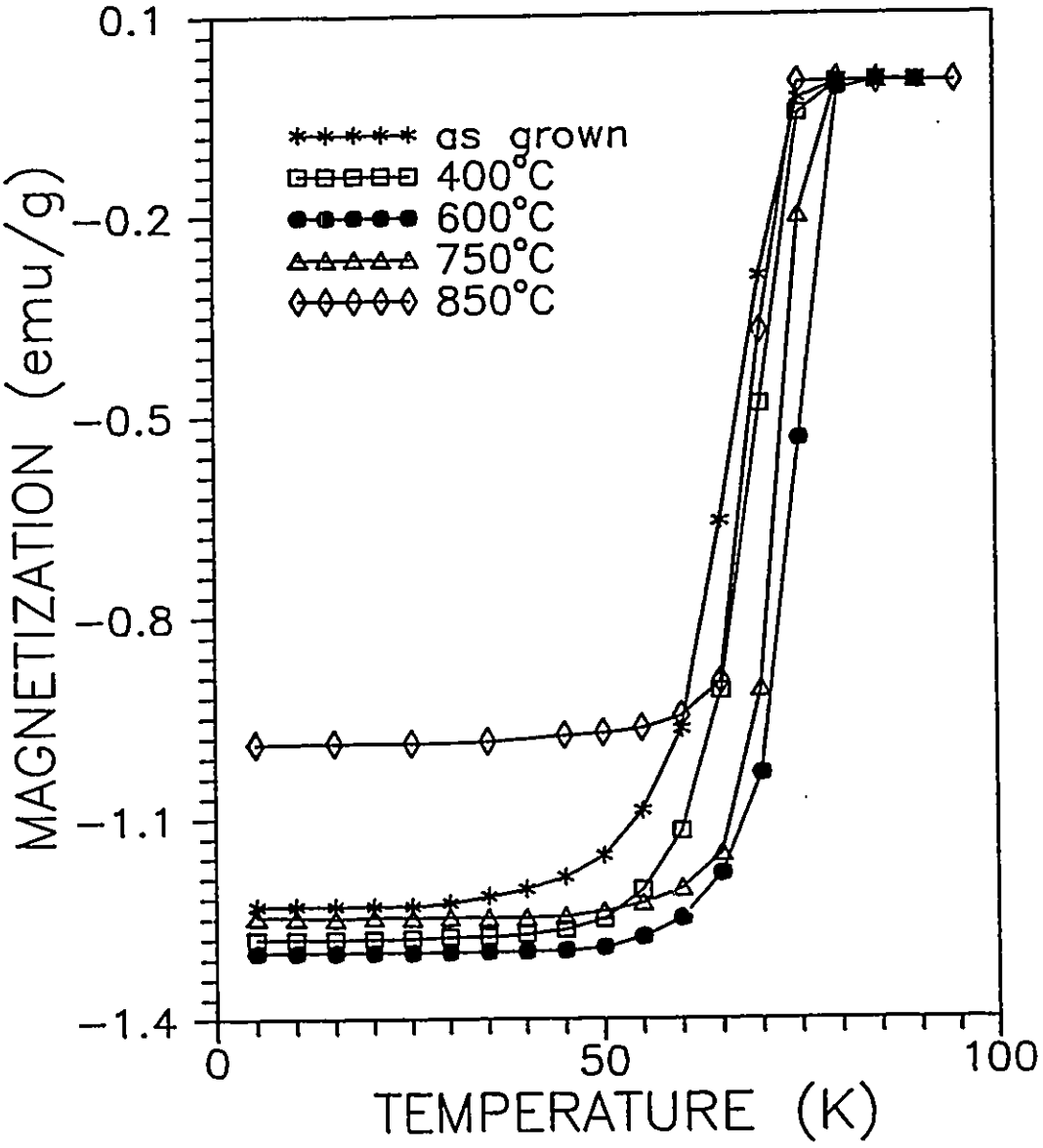

Figure 4.4.1 The magnetization flux exclusion of the same as grown $Pb_2Sr_2(Y/Ca)Cu_3O_{8+\delta}$ crystal, annealed in N_2 at various temperatures (as shown in the legend) for 12 hours.

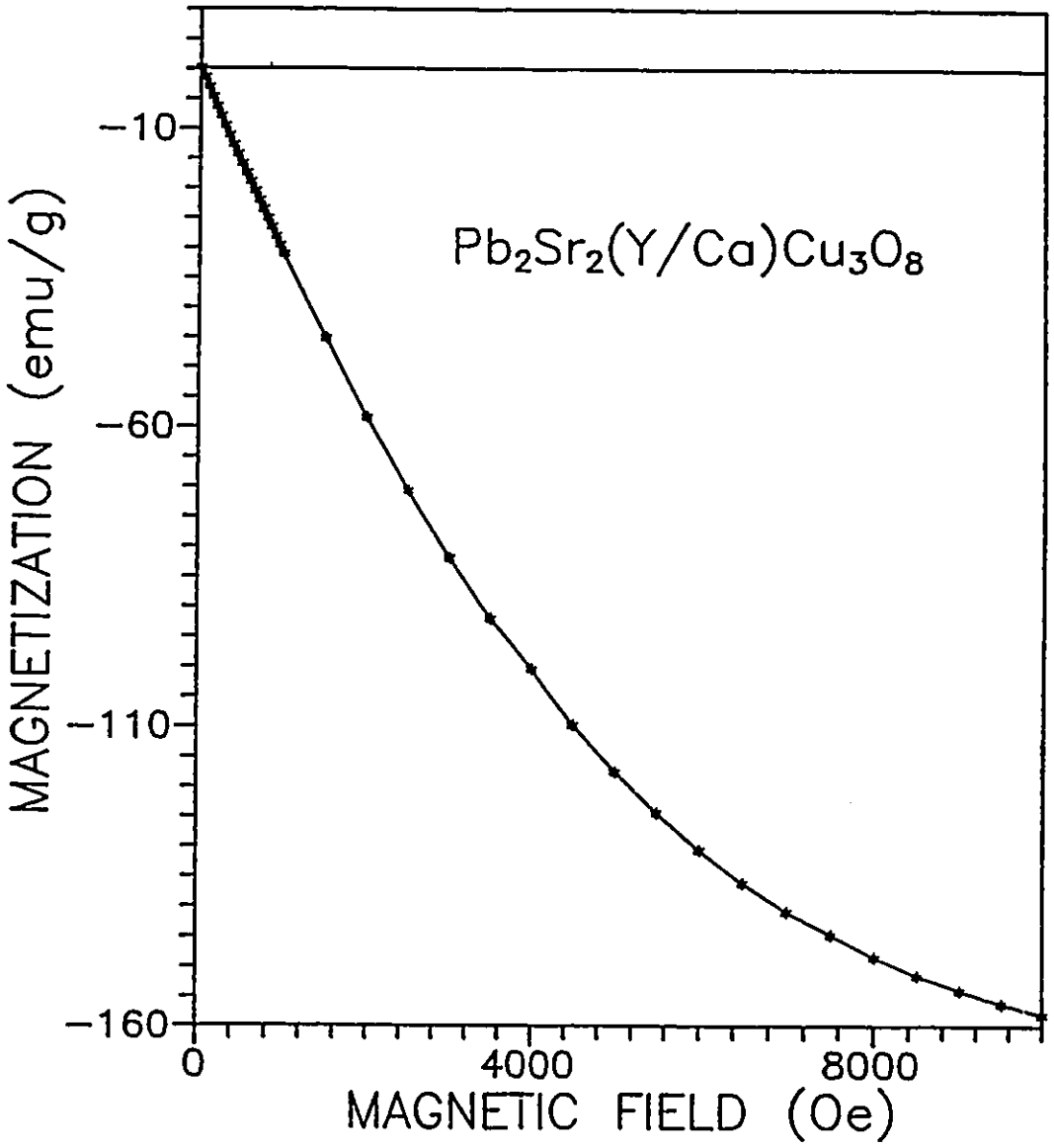

Figure 4.4.2 The magnetic field dependence of the flux exclusion of a $Pb_2Sr_2(Y/Ca)Cu_3O_{8+\delta}$ crystal at 5K.

4.5 Seed crystal growth method

In order to grow larger superconducting single crystals, a seed crystal technique was integrated with the PbO/NaCl flux method. The crystal growth process was similar to that of the PbO/NaCl flux method except that a few $Pb_2Sr_2(Er/Ca)Cu_3O_{8+\delta}$ crystals obtained from a previous PbO/NaCl flux growth run were chosen as seeds and dropped into the Pt crucible during the cooling process at a temperature ($\sim$930°C) near the incongruent melting temperature of the growth system[119]. The crystals grown by this method can be twice as large in all three dimensions and ten times heavier than those grown by spontaneous nucleation from the PbO/NaCl flux. No difference in the superconducting properties was found between the crystals grown from seeds and those from the PbO/NaCl flux.

4.6 Characterization

Chemical analysis

The chemical compositions of both Ca-doped and Ca-free 2213 single crystals were determined by electron probe microanalysis (EPMA), neutron activation analysis (NAA), inductively coupled plasma/mass spectroscopy (ICP/MS) and thermogravimetric analysis (TGA). EPMA was started with cold-mounting a crystal in an epoxy resin and polishing to obtain a clean surface. A point analysis was employed with probe voltage and current of 20kV and 30μA respectively. The measurement was performed by selecting randomly four locations on the polished surface. The x-ray intensities for all of the constituent elements in the crystal were accurately calibrated using

corresponding standards: crocoite ($PbCrO_4$) for Pb, celestite ($SrSO_4$) for Sr, anorthite ($CaAl_2Si_2O_8$) for Ca, cuprite (Cu_2O) for Cu and yttrium metal for Y. ICP/MS was conducted by dissolving approximately 3mg of crystals in 50ml of 6N hydrochloric acid for each test followed by dilution with high-purity water to a final concentration of 0.5 to 3ppm for each metal element. The experimental errors for the metal elements are within a range of ±2% and the results have been normalized upon Cu. The oxygen content of the crystals was determined by TGA using a Netzsch STA-409 thermal gravimeter. About 50mg crystals were held in an alumina crucible and heated with another empty crucible as standard from room temperature to 800°C at a rate of 10°C/min in 10%H_2-90%Ar gas. The analyses were based on the assumption that only Cu and Pb are reduced to their metallic forms:

$$Pb_2Sr_2RCu_3O_8 + 4\frac{1}{2}H_2 = 2Pb + 3Cu + 2SrO + \frac{1}{2}R_2O_3 + 4\frac{1}{2}H_2O$$

An accuracy of −3% by weight was obtained. The melting temperature of the crystals measured by differential thermal analysis (DTA) is 953±2°C. Impurities in the crystals grown from flux were detected qualitatively by using an energy dispersive x-ray (EDX) analyzer (LINK QX-2000). Table 4.6.1 lists the results of chemical analysis on the Ca-doped $Pb_2Sr_2(Y/Ca)Cu_3O_{8+\delta}$ crystals. NAA is insensitive to Pb, but from ICP/MS, the stoichiometric value of 2 is obtained. The Sr and Cu contents are consistent with the stoichiometric values of 2 and 3 respectively. The mass spectroscopic analysis was undertaken mainly to determine the Pb content. It is less reliable for the Y/Ca ratio because a low purity standard was used for Y. The neutron activation results are consistent with an Y/Ca ratio in the range 0.66:0.34 to 0.60:0.40. It can be seen, however, that the results obtained from these two

techniques are essentially consistent with one another. The oxygen content per formula unit, as determined from TGA is 8.48(11) which is higher than the reported value of 8.08[120]. This discrepancy is likely caused by a Pb-evaporation during the measurement. From NAA, contamination by Na and Pt is found to be less than 0.01 per formula unit while no Cl or Na is detectable by energy dispersive x-ray analysis (EDX). The EDX results also show that the two different starting compositions used to synthesize $Pb_2Sr_2(Y/Ca)Cu_3O_{8+\delta}$ give nearly the same crystal composition.

High resolution Guinier powder x-ray diffraction

Powder x-ray diffraction analysis was performed on polycrystalline samples or on individual crushed crystals using a high resolution Hägg-Guinier camera with Cu $K_{\alpha 1}$ radiation and a bent quartz crystal as monochromator. The lattice parameters for the Ca-free $Pb_2Sr_2RCu_3O_8$ crystal and polycrystal samples are given in table 4.6.2.

Resistivity and magnetization measurements

The temperature dependence of the dc resistivity of the $Pb_2Sr_2(R/Ca)Cu_3O_{8+\delta}$ single crystals was measured using the standard four-probe technique in the van der Pauw configuration[121]. Contacts were obtained by attaching gold wires ($\phi = 25\mu m$) to the corners of the crystal with silver paste, and annealing in N_2 at 600°C for a few hours. DC magnetization measurements were made using a Quantum Design SQUID magnetometer in the temperature range from 5 to 100K. The magnetic field, in the order of a few Oe, was parallel to the c-axis of the crystals for all measurements.

Table 4.6.1 Chemical analysis results of the $Pb_2Sr_2(Y/Ca)Cu_3O_{8+\delta}$ crystals.

Element	EPMA		NAA	ICP/MS	TGA
Pb	1.96(4)	1.98(2)	-	2.00(17)	
Sr	1.91(4)	1.89(3)	2.03(3)	2.05(18)	
Y	0.76(3)	0.74(3)	0.76(20)	0.87(9)	
Ca	0.33(3)	0.35(3)	0.37(3)	0.47(5)	
Cu	2.98(4)	2.98(2)	3.00(13)	3.15(26)	
O	-	-	-	-	8.48(11)
Initial Y/Ca	3/7	4/6	1/1	1/1	

Table 4.6.2 Lattice parameters for single crystal and polycrystalline samples of Ca-free $Pb_2Sr_2RCu_3O_8$ deduced from high resolution Guinier powder x-ray diffraction or single crystal x-ray diffraction for those marked with a '*'. The orthorhombic lattice parameters for those polycrystals with R = Pr, Nd and Tb have been given here due to negligible differences ($\leq 3\sigma$) between those parameters refined in monoclinic and orthorhombic symmetries.

	Single crystals			Polycrystals		
R	a(Å)	b(Å)	c(Å)	a(Å)	b(Å)	c(Å)
La	5.460(1)	5.505(1)	15.876(3)*	———		
Pr	5.456(2)	5.481(2)	15.804(5)*	5.377(1)	5.430(1)	15.798(2)
Nd	5.443(2)	5.468(2)	15.774(3)*	5.441(1)	5.474(1)	15.779(3)
Sm	5.432(2)	5.479(2)	15.772(3)	5.444(2)	5.468(1)	15.776(4)
Eu	5.421(1)	5.459(1)	15.758(2)	5.414(1)	5.455(1)	15.740(3)
Gd	5.394(2)	5.421(1)	15.789(3)	5.410(1)	5.444(2)	15.741(2)
Tb	5.407(1)	5.446(1)	15.742(2)*	5.406(1)	5.444(1)	15.733(2)
Dy	5.398(1)	5.432(2)	15.773(3)	5.402(1)	5.438(1)	15.724(3)
Ho	5.400(1)	5.424(1)	15.748(5)*	5.379(1)	5.428(2)	15.720(4)
Er	———			5.387(1)	5.427(1)	15.702(2)
Tm	———			5.380(1)	5.420(1)	15.702(2)
Yb	———			5.376(1)	5.417(1)	15.702(2)
Y	5.389(1)	5.420(1)	15.750(2)	5.391(1)	5.430(1)	15.728(2)

4.7 The role of NaCl in the crystal growth

The advantages of adding NaCl to the PbO flux are manifold. The PbO/NaCl flux is a two-phase liquid at high temperature due to the low miscibility of NaCl in PbO. Being less dense than PbO, the NaCl layer encapsulates the melt from the growth atmosphere during the entire crystal growth process and thus, relaxes the stringent atmospheric condition (N_2, 1% O_2) which is necessary for crystal growth in the absence of NaCl flux[7,109,110]. The reduced volatility of PbO due to the NaCl encapsulating layer results in a more stable flux composition and a reduced PbO toxicity hazard. Superconducting 2213 crystals can thus be grown from a PbO/NaCl flux either in N_2 or in air.

Owing to the large number of constituent elements involved in the crystal growth system, the construction of an actual phase diagram is difficult. However, the pseudobinary phase diagrams of PbO-PSYCCO and PbO/NaCl-PSYCCO systems were determined in air by improved thermogravimetric analysis (ITGA) and differential thermal analysis (DTA)[119]. The results are shown schematically by the dashed and solid lines respectively in figure 4.7, where region L stands for Liquid. There are two main differences between these two systems: i) In the PbO/NaCl-PSYCCO system, the composition range for crystal growth (from a to b in figure 4.7) is much wider than that in the PbO-PSYCCO system (30% versus 5%) due to the reduced slope of the liquidus, (a composition of 33% PSYCCO was chosen in most of our crystal growth runs) and ii) the addition of NaCl lowers the eutectic temperature of the PbO-PSYCCO system from 800 to 770°C. Consequently, the conditions for crystallization of $Pb_2Sr_2(Y/Ca)Cu_3O_{8+\delta}$ are better due to a larger cooling range (from 950 to 770°C).

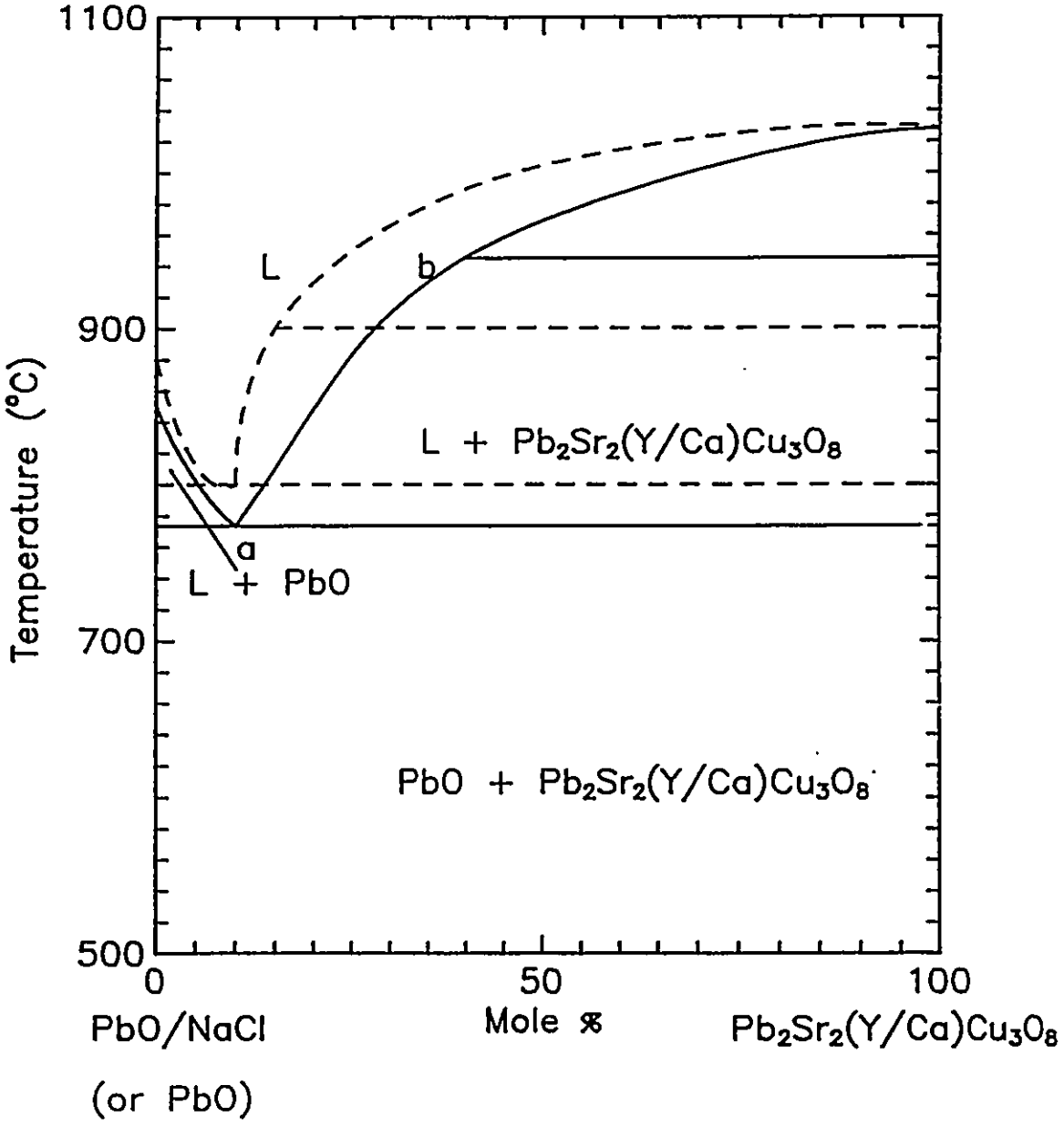

Figure 4.7 Schematic pseudobinary phase diagram of $Pb_2Sr_2(Y/Ca)Cu_3O_{8+\delta}$ - PbO (dashed line) and - PbO/NaCl (solid line) systems.

4.8 Effect of varying the starting Y/Ca ratio

More than ten precursors with different starting Y/Ca ratios ranging from 0/1 (pure Ca) to 1/0 (pure Y) were prepared. Using the method described above, crystals of $Pb_2Sr_2(Y/Ca)Cu_3O_{8+\delta}$ were obtained when the starting Y/Ca ratio was greater than 1/4. A similar chemical composition was obtained on three crystals with starting Y/Ca ratios of 3/7, 4/6 and 1/1 (see table 4.6.1). Meanwhile, the EPMA results showed good homogeneity of one crystal while a few lead-deficient lamellae were detected in the other. The actual Y/Ca ratio in the crystals deduced from EPMA and ICP/MS is always close to 7/3. The fact that from resistivity measurements, all of the $Pb_2Sr_2(Y/Ca)Cu_3O_{8+\delta}$ crystals grown from the PbO/NaCl flux exhibit similar T_c's above 80K is another indication that all of the $Pb_2Sr_2(Y/Ca)Cu_3O_{8+\delta}$ crystals have a similar Y/Ca ratio regardless of the starting composition (figure 4.8). Possible explanations for the tendency of the system to revert to this composition are: i) that $Pb_2Sr_2Y_{0.7}Ca_{0.3}Cu_3O_{8+\delta}$ is a thermodynamically stable phase in this specific composition of the PbO/NaCl flux system; and ii) that the NaCl encapsulating layer stabilizes the oxidation states of the constituent elements in the system, and maintains a constant oxygen fugacity, or partial pressure, within the flux mixture which controls the Cu^{2+}/Cu^{3+} ratio and thus the Y/Ca ratio[122].

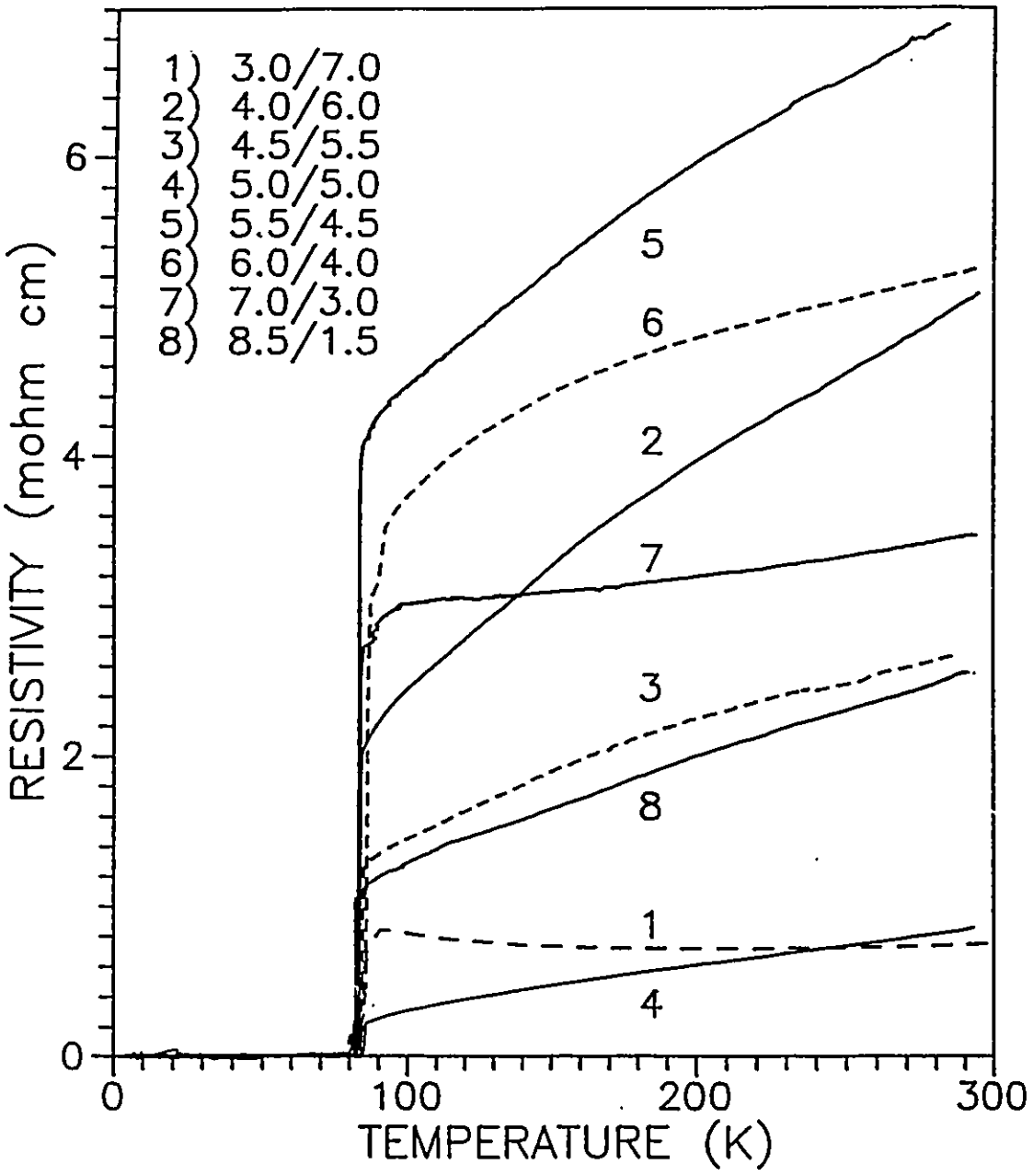

Figure 4.8 Resistivity measurements on several $Pb_2Sr_2(Y/Ca)Cu_3O_{8+\delta}$ crystals with different starting Y/Ca ratio as indicated in the legend show basically the same T_c near 80K.

4.9 Rare-earth substitution

Single crystals of $Pb_2Sr_2(R/Ca)Cu_3O_{8+\delta}$ (R = Nd, Sm, Gd, Dy, Er, Tm, Yb or Lu) were synthesized by the PbO/NaCl flux method. The R/Ca ratio of all the crystals deduced from energy dispersive x-ray analysis (EDX) is, once again, approximately equal to 7/3. Their lattice parameters and cell volumes, listed in table 4.9, were deduced from high resolution Guinier camera data. It is observed that the a and b axes increase with increasing ionic radius of the rare-earth, while the c-axis is more or less constant (figure 4.9.1). The cause of the relatively low values for the lattice parameters and cell volume of the Gd 2213 phase, which are similar to those of the Ca-free 2213 phases[109], is still not clear. The figure of merit (FOM) in table 4.9 is defined as:

$$FOM = \frac{N_{obs}}{|\delta 2\theta| \times N_{calc}} \qquad (4\text{-}9)$$

where $|\delta 2\theta|$ is the average absolute discrepancy between observed and calculated 2θ values; and N_{obs} and N_{calc} stand for the number of observed and calculated diffraction lines, respectively within the 2θ range[123].

Resistivity measurements of the $Pb_2Sr_2(R/Ca)Cu_3O_{8+\delta}$ crystals (R = Sm, Gd, Dy, Er or Y) show a similar onset T_c for all crystals which is, with the exception of Sm, relatively sharp although a small foot is observed in most of the crystals which extends to approximately 75K (figure 4.9.2). The magnetization measurements, however, give a better indication of the superconducting properties of these crystals (figure 4.9.3).

Some of the rare-earth substituted $Pb_2Sr_2(R/Ca)Cu_3O_{8+\delta}$ crystals (R = Er, Tm or Y) exhibit much sharper superconducting transitions than the others. There appears to be a correlation between a sharper magnetic transition and the crystal quality as measured by the FOM from the Guinier data analysis. Those crystals showing sharper transitions (R = Er, Tm and Y), have large FOM's in contrast to those which have small FOM's and broad transitions (R = Sm, Gd and Dy). The small FOM value is likely to be correlated with inhomogeneity in the crystal, i.e. Pb-deficient lamellae which were detected in some $Pb_2Sr_2(Y/Ca)Cu_3O_{8+\delta}$ crystals by EPMA.

Table 4.9 High-resolution Guinier data for $Pb_2Sr_2(R/Ca)Cu_3O_{8+\delta}$. The lattice parameters of the Nd 2213 phase could not be accurately determined due to poor crystal quality.

R	a(Å)	b(Å)	c(Å)	V(Å^3)	FOM
Sm	5.4051(17)	5.4438(16)	15.836(2)	463.00(2)	13.4
Gd	5.3829(8)	5.4243(11)	15.730(3)	459.28(10)	12.9
Dy	5.3895(5)	5.4284(6)	15.743(2)	460.57(6)	23.7
Y	5.3750(5)	5.4090(4)	15.763(1)	458.27(4)	387.2
Er	5.3784(5)	5.4123(6)	15.765(2)	458.91(6)	482.8
Tm	5.3697(5)	5.4067(5)	15.761(2)	457.58(5)	643.5
Yb	5.3633(8)	5.4208(10)	15.718(4)	456.97(1)	22.7
Lu	5.3652(5)	5.3993(5)	15.746(2)	456.13(6)	461.9

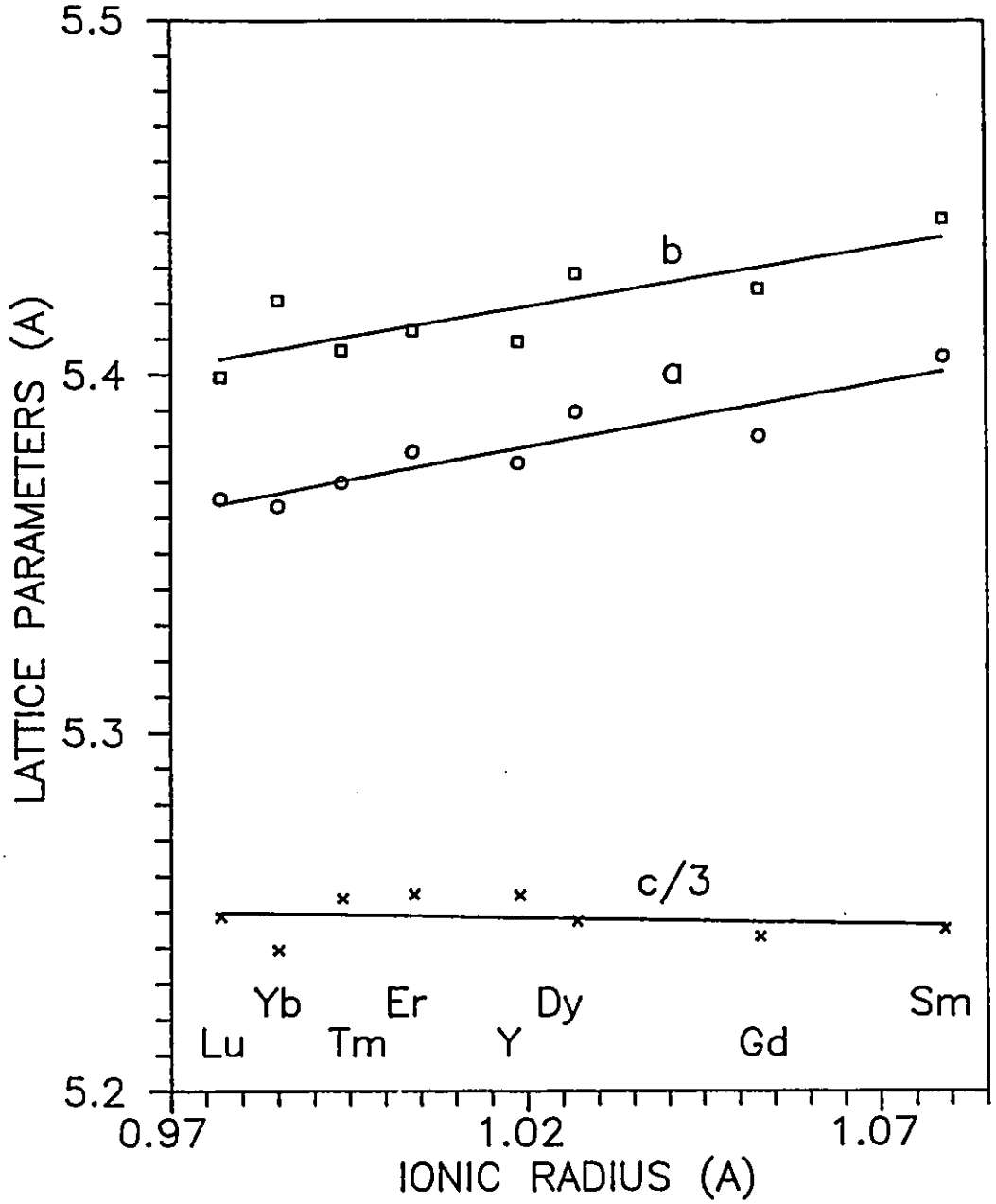

Figure 4.9.1 The lattice parameters of $Pb_2Sr_2(R/Ca)Cu_3O_{8+\delta}$ (R = Sm, Gd, Dy, Er, Tm, Yb, Lu and Y) deduced from a high resolution Guinier data.

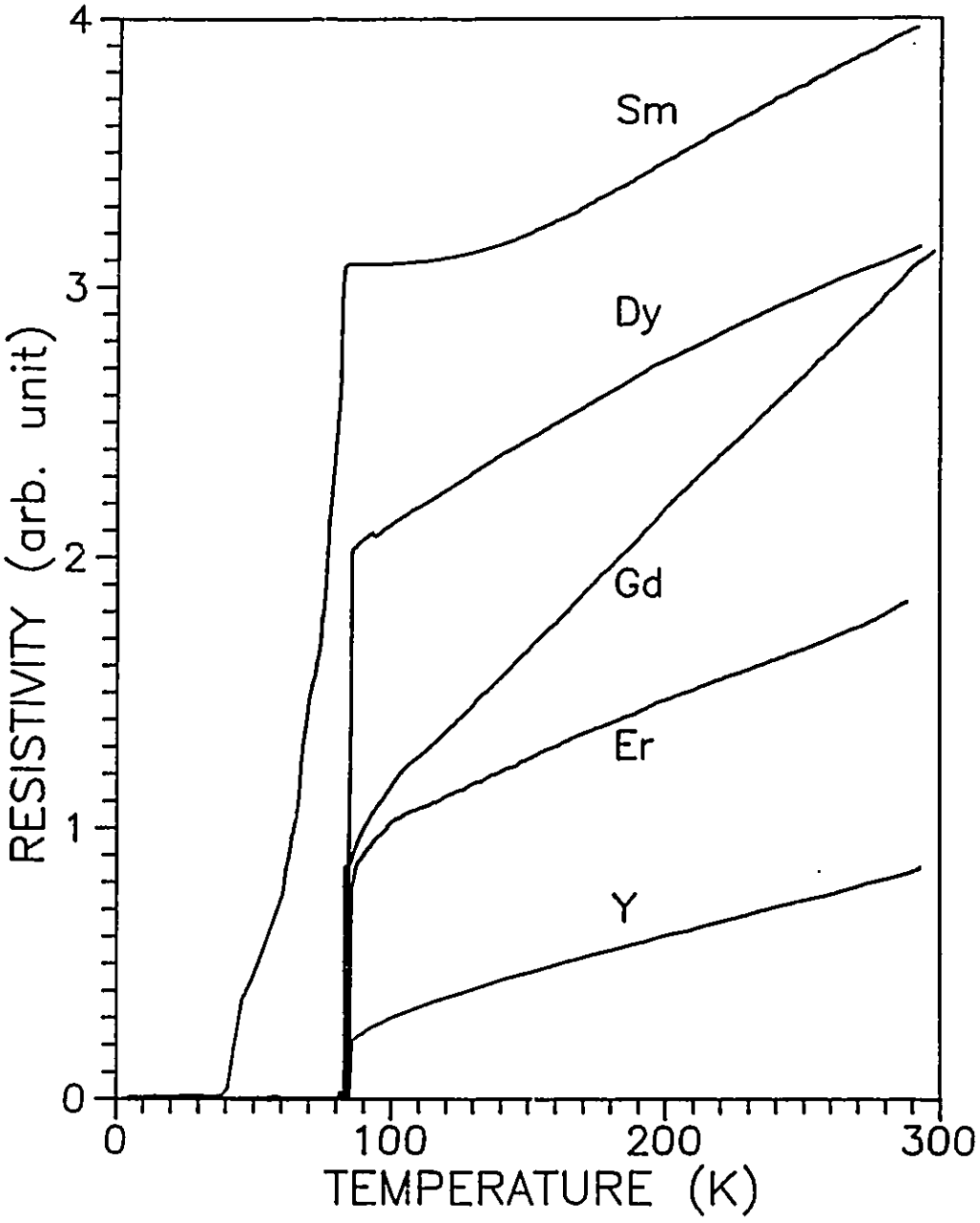

Figure 4.9.2 The temperature dependence of the in-plane resistivity of $Pb_2Sr_2(R/Ca)Cu_3O_{8+\delta}$ (R = Sm, Gd, Dy, Er or Y) crystals.

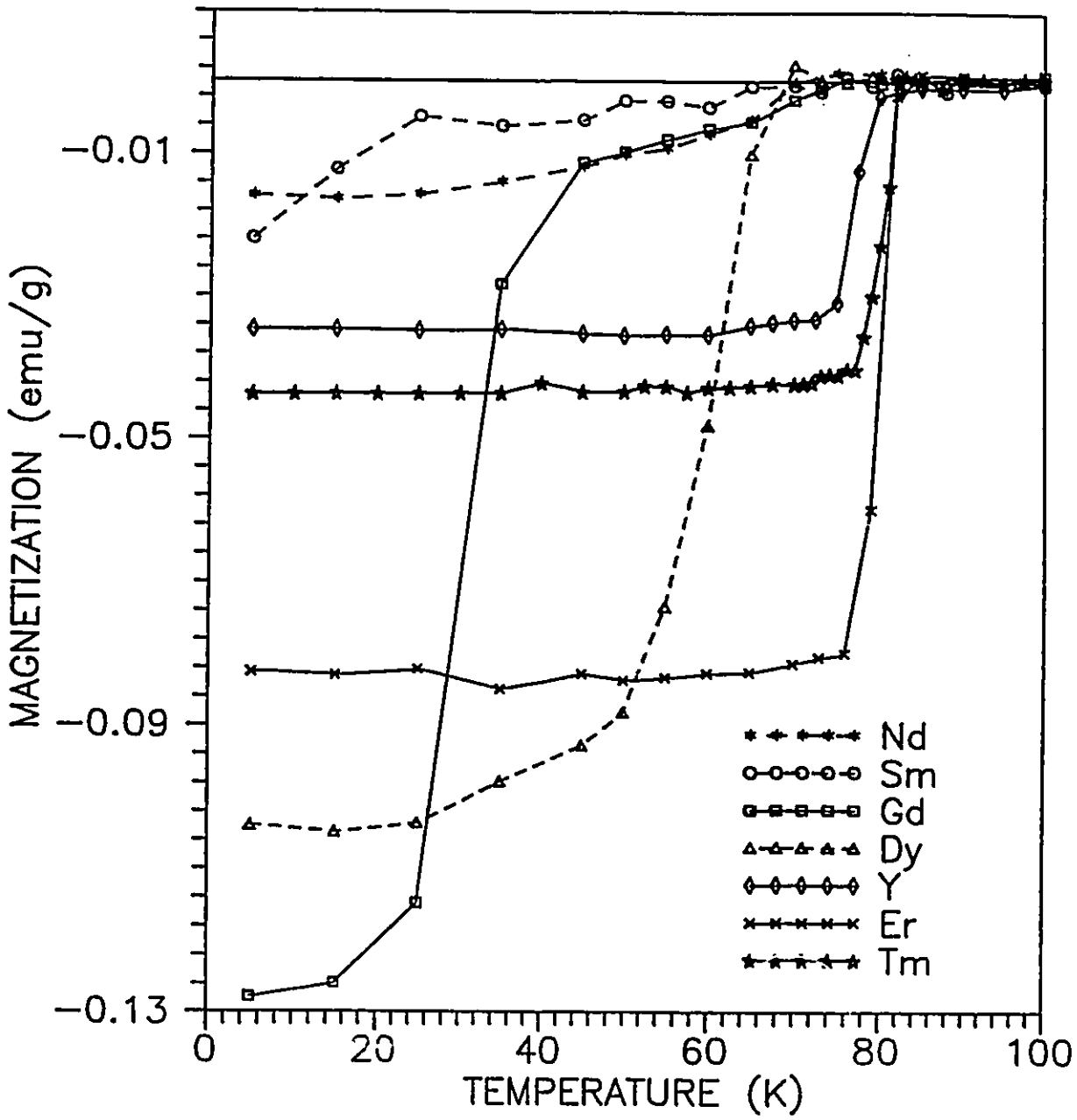

Figure 4.9.3 Low field magnetization of the $Pb_2Sr_2(R/Ca)Cu_3O_{8+\delta}$ (R = Nd, Sm, Gd, Dy, Er, Tm and Y) crystals.

4.10 Violation of the C-centering symmetry

The observed d-spacings for a $Pb_2Sr_2Y_{0.7}Ca_{0.3}Cu_3O_{8+\delta}$ crystal listed in table 4.10 are consistent with an orthorhombic cell a = 5.383(1), b = 5.423(1) and c = 15.765(2)Å. The splitting of reflections of the type *hkO* and *khO* is seen easily. Also note the presence of a few reflections of the type *hkl* with $h+k=2n+1$ which violate the C-centering condition. An examination of the reflected intensities collected from a crystal using a single crystal x-ray diffractometer indexed on the orthorhombic cell indicated 148 unique reflections out of 834 which violate C-centering. Thus, the crystal symmetry for this crystal would be primitive. Electron diffraction data obtained in a transmission electron microscope (TEM) also showed C-centering violations (figure 4.10) but failed to exhibit any modulations or superlattice in the a*b*-plane. Results somewhat similar to these were reported for a crystal of composition $Pb_2Sr_{2.24}Nd_{0.76}Cu_3O_8$ but in this case no C-centering violations were detected; however evidence for a superlattice was seen[7]. In another case data from a crystal of nominal composition $Pb_2Sr_2Y_{0.75}Ca_{0.25}Cu_3O_8$ were indexed as tetragonal with a = 3.813(2)Å and c = 15.76(1)Å[101].

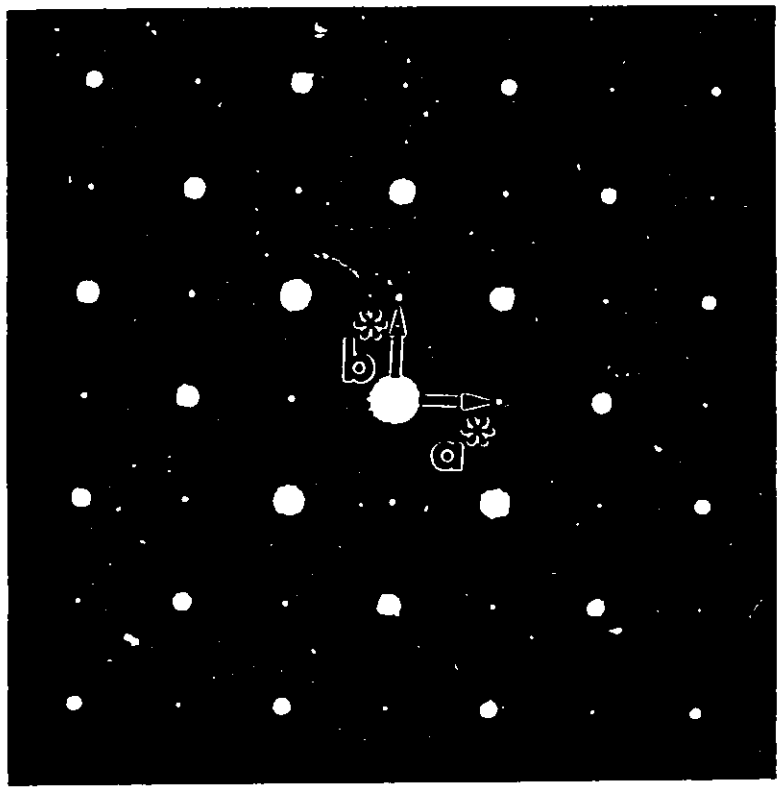

Figure 4.10 Electron diffraction pattern of $Pb_2Sr_2(Y/Ca)Cu_3O_{8+\delta}$ showing the well defined $h+k=2n+1$ reflections which are violating the C-centering condition.

Table 4.10 Guinier camera data for a $Pb_2Sr_2(Y/Ca)Cu_3O_{8+\delta}$ single crystal.

h k l	d(Å)	h k l	d(Å)	h k l	d(Å)	h k l	d(Å)
0 0 2	7.906	2 0 1	2.654	2 2 4	1.719	0 0 11	1.433
0 0 3	5.254	0 0 6	2.628	1 3 0	1.713	2 2 8	1.371
0 0 4	3.947	0 0 7	2.254	3 1 0	1.703	0 2 10	1.363
1 1 0	3.822	0 2 4	2.233	3 1 1	1.694	2 3 5	1.355
1 1 1	3.716	1 1 6	2.165	1 1 9	1.593	4 0 0	1.345
1 1 2	3.440	0 2 5	2.005	0 0 10	1.576	4 1 3	1.268
1 1 3	3.293	2 0 5	2.047	1 3 4	1.572	1 1 12	1.242
1 1 4	2.745	0 0 8	1.971	3 1 4	1.563	1 3 9	1.225
0 2 0	2.710	2 2 0	1.910	2 2 6	1.545	2 4 0	1.211
2 0 0	2.692	0 0 9	1.752	2 2 7	1.456	4 2 0	1.205
0 2 1	2.672	0 2 7	1.732	2 3 3	1.444	4 1 7	1.130

4.11 Discussion

It is interesting to notice that single crystals of both the 2213 and 1212 lead cuprate phases can be prepared by using the same composition of starting materials (without NaCl) under different atmospheres, N_2 for 2213 and air or O_2 for 1212[124]. A similar situation has arisen in the growth of lead cuprate thin films. Thin films of the 1212 phase were grown under an oxygen atmosphere by Hughes et al.[125] using laser ablation, and of the 2213 phase under nitrogen by Adachi et al.[115] using rf-magnetron sputtering. This demonstrates that the oxygen partial pressure plays an important role in the determination of the product and the partial exclusion of oxygen by the encapsulating NaCl layer is critical to the crystal growth of the 2213 phase.

CHAPTER 5

CRYSTAL STRUCTURE OF Ca-FREE $Pb_2Sr_2RCu_3O_8$

Ca-free, or the proto-type, $Pb_2Sr_2YCu_3O_8$ has been described as an insulator by several groups[7,126,127]. Bulk superconductivity ($T_c = 10$ to 70K) in Ca-free 2213 single crystals was first reported by Cava et al.[7] without further detailed study of crystal structure and physical properties of these materials. Schneemeyer et al.[109] substituted various rare-earth elements (R) into the Y-sites. The resultant polycrystalline compounds, $Pb_2Sr_2RCu_3O_8$, are nonsuperconducting as well, although a small amount of superconductivity (1% or less) was often observed in the samples which was ascribed by the authors to variations in the oxygen content or to inhomogeneities. Later, Prasad et al.[114] reported the existence of superconductivity ($T_c = 70$K) in $Pb_2Sr_2RCu_3O_8$ (R = any rare-earth except for La and Ce) powder samples with a low superconducting volume fraction ($\leq 10\%$). Thus the situation regarding the Ca-free 2213 phase is presently unclear.

The crystal structure of R = Nd was first refined in an orthorhombic space group, Cmmm, by Cava et al.[7] using single crystal x-ray diffraction. The oxygens in the PbO layers were fixed at the special position (*0,0,z*) which yielded a high thermal parameter. A tetragonal space group, P4/mmm, has also been assigned to these Ca-free crystals[109]. Subsequently, a more detailed structural study on an R = Nd crystal was reported by Hayri et al.[127] The R-O1 bond lengths of 2.488(5)Å and 2.478(8)Å

obtained from these two refinements respectively, are too short in comparison with an averaged bond length of 2.55Å calculated for a Nd/Sr ratio of 0.76/0.24 by summing the effective ionic radii[118].

The fact that bulk superconductivity (nearly 100% shielding volume fraction) was detected in those $Pb_2Sr_2YCu_3O_8$ single crystals grown from a Ca-free PbO/NaCl flux (see §4.8) was surprising since there is no apparent chemical doping in these materials. In order to understand this result, a systematic study of the crystal growth[128], structural and chemical characterizations[129] and physical properties[128,130] of a $Pb_2Sr_2RCu_3O_8$ (R = La, Ce, Pr, Nd, Sm, Eu, Gd, Tb, Dy, Ho and Y) single crystal series has been carried out. This series turns out to be an ideal system for the study of the relationship between crystal structure and the electronic properties of high-T_c copper oxide superconductors since these crystals display a systematic trend from insulating to metallic and superconducting character as a function of decreasing rare-earth size[128,130]. Crystals of $Pb_2Sr_2RCu_3O_8$ with R = La, Ce, Pr and Nd exhibit insulating behaviour with basically no carrier-doping in the CuO_2 planes; R = Sm, Eu, Gd and Tb are lightly doped; and R = Dy, Ho and Y are poor metals. The crystals with medium or small rare-earth elements (i.e. R = Eu, Gd, Dy, Ho and Y) also show a superconducting transition around 75K with the exception of crystals with R = Tb which are nonsuperconducting due to reasons which will be discussed later in §6.5. Results of dc-resistivity and mid-infrared optical reflectivity measurements on these Ca-free $Pb_2Sr_2RCu_3O_8$ single crystals have been reported[130]. Crystals of the Ca-free 2213 phase were grown using the method described in §4.3. The crystal growth parameters and comments concerning crystal quality have been given in table 4.3.3. This chapter focuses mainly on the crystal structures of $Pb_2Sr_2RCu_3O_8$ which have

been determined on samples with R = La, Pr, Nd, Eu, Tb and Dy by single crystal x-ray diffraction and discusses the monoclinic distortion found for R = Pr, Nd and Tb in terms of ordering of oxygen atoms driven by the Pb^{2+} lone pair orientation, addresses a possible (*110*) micro-twinning in the R = Eu and Dy crystals and interprets a bond valence sum analysis of the six crystals studied.

5.1 Crystal structure determination

A typical crystal structure determination started with choosing a small, brick-shaped $Pb_2Sr_2RCu_3O_8$ crystal in order to minimize x-ray absorption which is serious for these compounds. The linear absorption coefficient of $Pb_2Sr_2LaCu_3O_8$ is 57.17 mm^{-1} for a silver radiation source with a wave-length of 0.56086Å. The data sets were collected for $Pb_2Sr_2RCu_3O_8$ (R = La, Pr, Nd, Eu, Tb and Dy) on a Siemens P3 single crystal x-ray diffractometer. The crystal faces were indexed after data collection. The shapes of the crystals were examined under an optical microscope (Olympus BH-2) and recorded by a video camera so that the dimensions of the crystals could be measured on a magnified view from a TV screen giving an accuracy of $\pm 0.7\mu m$. A face-indexed numerical absorption correction was then performed. Details of the data collection and crystallographic information for six $Pb_2Sr_2RCu_3O_8$ (R = La, Pr, Nd, Eu, Tb and Dy) crystals are given in table 5.1.1 and the crystal structural diagrams obtained from refinement are illustrated in figure 5.1, where the thermal ellipsoids are drawn as 50% probability surfaces and the displaced O3 in the PbO layers are represented by dashed ellipsoids.

$Pb_2Sr_2RCu_3O_8$ (R = Pr, Nd and Tb)

Small monoclinic distortions were detected in several $Pb_2Sr_2RCu_3O_8$ (R = Pr, Nd and Tb) crystals by the single crystal x-ray diffractometer. In the case of the R = Nd crystal, the monoclinic lattice parameters were refined from 35 centred reflections with 2θ range from 15° to 40° using an auto-indexing package supplied by Siemens. A data set was collected on a primitive lattice within a hemisphere. Direct methods were applied to locate the metal positions in the unit cell and a full-matrix least-squares refinement was carried out by minimizing $\Sigma w(|F_o|-|F_c|)^2$ using the SHELXTL-PLUS(VMS) package. 117 out of a total 2024 independent reflections were found which violated the C-centering condition $h+k=2n$ and 72 of these had an integrated intensity greater than $3\sigma(I)$ suggesting a primitive lattice. The systematic extinctions of *OkO:* $k=2n+1$ and *hOl:* $h=2n+1$ are consistent with the space group $P2_1/a$ (No.14). However, the structure refinement performed on this space group was not very successful: the thermal parameters of oxygens could only be refined isotropically (otherwise, they became non-positive definite) and the R-indices were R = 7.80% and R_w = 7.76%, respectively. Strong correlations with the correlation coefficients ranging from 0.71 to 0.92 were observed in both the z-coordinates and anisotropic thermal parameters between the oxygens at (¼, ¼, z) and (¼, ¾, z) in the CuO_2 layers implying a higher symmetry space group. Refinement in C2/m (No.12) was successfully conducted by omitting those weak $h+k=2n+1$ reflections which presumably originate from the oxygen ordering in the PbO layers and will be discussed in more detail later in §5.2. The unit cell is shown in figure 5.1c. Refinements on $Pb_2Sr_2RCu_3O_8$ with R = Pr and Tb were similar except that an electron density deficiency of ~4.5% was found at the Tb-site. The best refinement was achieved in the case of R = Tb (see

table 5.1.1 for the R-indices). The results are given in tables 5.1.2 and 5.1.3.

$Pb_2Sr_2LaCu_3O_8$

In contrast, there was no monoclinic distortion observed in the $Pb_2Sr_2LaCu_3O_8$ crystal. The lattice parameters a=5.460(1)Å, b=5.505(1)Å, c=15.876(3)Å, α=90.00(1)°, ß=90.03(1)° and τ=90.02(1)° were obtained from a thin plate of $Pb_2Sr_2LaCu_3O_8$ using 38 centered reflections with 2θ ranging from 15° to 30° indicating an orthorhombic cell. A data set was collected from the primitive lattice within one octant. There were 143 out of a total 1412 independent reflections violating the C-centering condition, but only 61 of them had an integrated intensity greater than $3\sigma(I)$. The intensities of these reflections are relatively weak [$3\sim10\sigma(I)$]. The same crystal was mounted on a precession camera, exposed for four days and none of these weak reflections appeared on the film. The space group Pman, which is a non-standard setting of Pmna (No.53), was deduced from the systematic absences of *hk0:* $h+k=2n+1$ and *h0l:* $h=2n+1$. The structure refinement was performed by using the reported atomic coordinates[131] as the starting values, except that the position *8i* (*x,y,z*) was assigned to the oxygens (O3) in the PbO layers in our refinement instead of *4h* (*0,y,z*) as in reference 131. The anisotropic thermal parameters of O3 thus obtained were basically isotropic. However, the refinement results were still unsatisfactory since a similar situation was encountered as in the monoclinic case, i.e. strong correlations and non-positive definiteness of the oxygen thermal parameters. Therefore, as in the previous cases, the higher symmetry space group, Cmmm (No.65), was used. The refinement results (see tables 5.1.2 and 5.1.3) resemble those of the monoclinic cases except that the O3 in the PbO layers are split

into four closely-spaced sites instead of two as in the latter. The occupancies of both the rare-earth and O3 were refined to full and quarter occupation respectively and were subsequently fixed at these values in the final refinement due to insignificant deviation. An orthorhombic symmetry was deduced for an R = Ho crystal as well (cf. table 4.6.2) from 26 centered reflections with 2θ ranging from 20 to 40°. The unit cell is shown in figure 5.1b.

$Pb_2Sr_2RCu_3O_8$ (R = Eu and Dy)

The structure refinements of the $Pb_2Sr_2RCu_3O_8$ (R = Eu and Dy) crystals proceeded somewhat differently from those described above. A primitive, tetragonal cell was found for a $Pb_2Sr_2EuCu_3O_8$ crystal from 25 centered reflections. The attempt to transform the small, primitive cell ($a_p \approx 3.84$Å) to a conventional cell with $a = \sqrt{2}a_p \approx 5.4$Å was made by collecting a small data set of 500 reflections with 2θ ranging from 4 to 45° in the one octant. None of the measured intensities of those reflections corresponding to the 5.4Å cell was greater than $3\sigma(I)$. Therefore, a primitive 3.8Å cell was assumed. The space group P4/mmm was deduced by using an algorithm suggested by Y. LePage[132] ——— a strategy based on identifying the three shortest two-fold axes which limit the lattice symmetry and conventional cell edges. In the primary stage of refinement, the oxygens in the PbO layer were restricted to the position *2g* (*0,0,z*). The thermal parameters at this site were highly anisotropic: the components of U_{11} and U_{22} being about one order of magnitude higher than U_{33} indicating that the O3 are disordered in the basal plane. Two potential positions for O3 in space group P4/mmm are *8r* (*x,x,z*) and *8s* (*x,0,z*). Both of them will allow the disordering of O3 over four sites. The refinement of O3 at *8r* reduced

the amplitudes of U_{11} and U_{22} to one third of their former values, but the anisotropy was still large. Splitting the oxygen atoms has the effect of moving them directly towards the Pb atoms and gives rather short bond lengths of 2.310(35)Å and 1.866(34)Å for Pb-O3 and Cu1-O3, respectively. The refinement using *8s* (*x,O,z*) gives basically isotropic thermal displacement parameters and reasonable bond lengths for Pb-O3 and Cu1-O3 (see table 5.1.3). The O3 atoms in the refined structure (figure 5.1a) are located on ac- and bc-planes. An attempt to put extra oxygens at a potential oxygen position (*0, ½, ½*) yielded an extremely high thermal displacement parameter which confirms the absence of oxygen in the Cu1 layer.

Refinement of the R-site occupation

Full-occupancy of the rare-earth sites was assumed in the early stages of the structure refinement for $Pb_2Sr_2EuCu_3O_8$, but a large residual electron density peak ($\sim 10 e/Å^3$) at the Eu-site suggested that too many electrons had been assumed in the structural model. Thus, two hypothetical disordered models ——— that of cation-vacancies and Eu^{3+}/Sr^{2+} mixed-occupation were refined independently. For the cation-vacancy model, the anisotropic thermal displacement parameters for Eu were refined concurrently with the site-occupancy, and the results showed a deficiency of ~9% at the Eu-sites; while for the mixed-occupation model, an Eu^{3+}/Sr^{2+} ratio of 0.77/0.23 was obtained. Both refinements yielded basically the same R-indices and anisotropic displacement parameters of the rare-earth sites since the same number of electrons (57e/site) were assigned to the rare-earth sites in both models. Similar results were obtained in the case of R = Dy. At the final stage of the refinement, the largest residual electron density peak ($\sim 5 e/Å^3$) in the difference Fourier map was at position

(*0.4,0.4,0.4*) about 0.51Å from the Pb ions. Refinement of the occupancy and the x and y coordinates of the Pb ions showed neither deviation from full-occupation nor a positional shift. These residual electron densities seem to be caused by anisotropic extinction, imperfect correction for absorption ... etc.

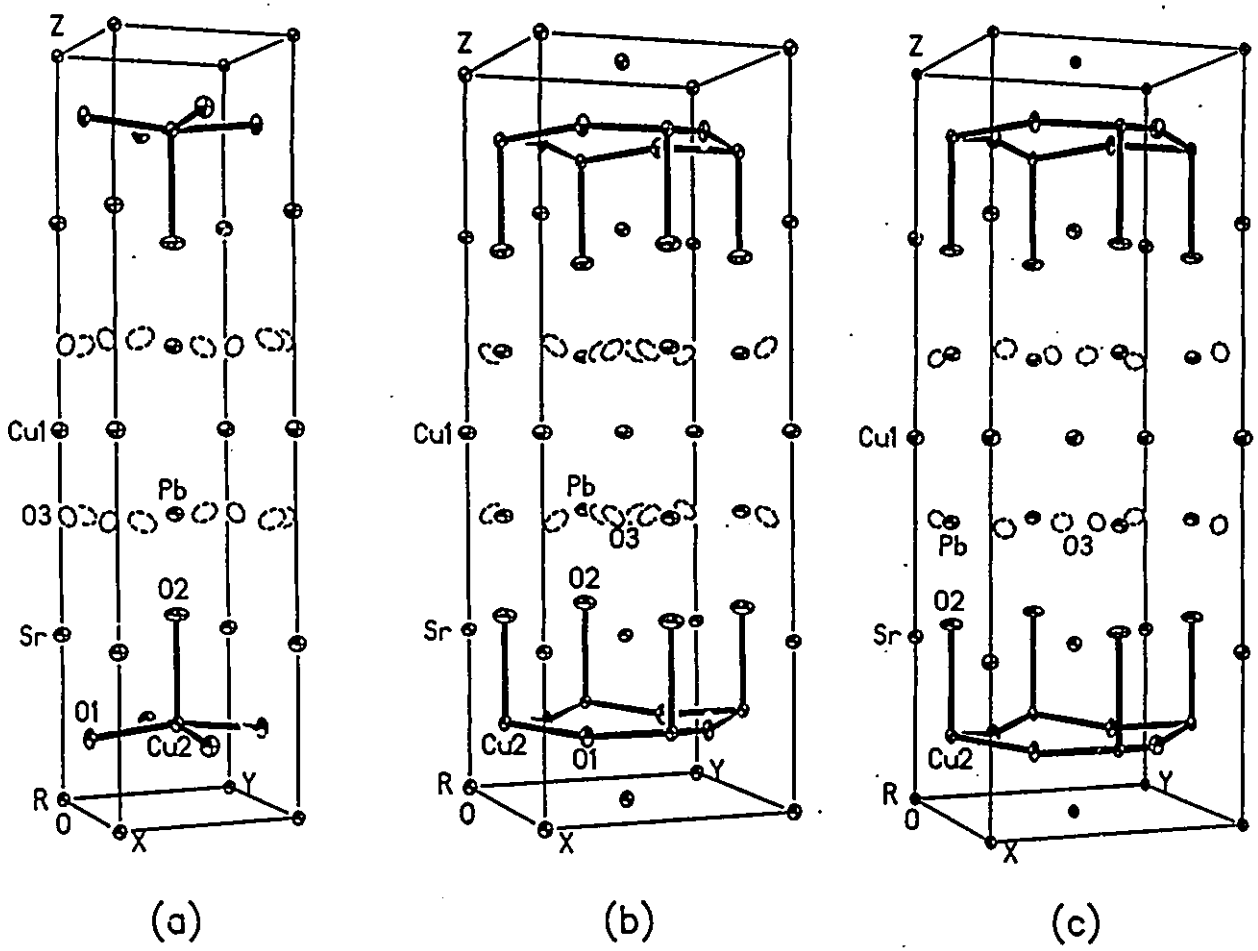

Figure 5.1 Unit cells of $Pb_2Sr_2RCu_3O_8$ with (a) primitive, tetragonal symmetry for R = Eu and Dy, (b) C-centered, orthorhombic for R = La, and (c) C-centered monoclinic for R = Pr, Nd and Tb.

Table 5.1.1 Summary of Crystallographic information for $Pb_2Sr_2RCu_3O_8$ (R = La, Pr, Nd, Eu, Tb and Dy).

R	La	Pr	Nd	Eu	Tb	Dy
Dimensions (mm^3)	0.100x0.100x0.031	0.172x0.167x0.005	0.131x0.122x0.100	0.147x0.136x0.072	0.153x0.112x0.027	0.124x0.117x0.069
Diffractometer	Siemens P3					
Radiation	Ag K_α(λ = 0.56086Å)					
Monochromator	Graphite					
Temperature	Ambient					
Absorption correction	Face-indexed numerical					
Scan mode	θ - 2θ					
2θ range (°)	3 - 80	3 - 80	3 - 60	3 - 80	3 - 70	3 - 80
Octants	+ + +	+ + + --+	+ + + -+ + --+ +-+	+ + + --+	+ + + -+ + --+ +-+	+ + + --+
Crystal system	Orthorhombic	Monoclinic		Tetragonal	Monoclinic	Tetragonal
Space group	Cmmm(65)	C2/m(12)	C2/m(12)	P4/mmm(123)	C2/m(12)	P4/mmm(123)
a (Å)	5.460(1)	5.456(2)	5.443(2)	3.846(2)	5.407(1)	3.833(1)
b (Å)	5.505(1)	5.481(2)	5.468(2)	3.846	5.446(1)	3.833
c (Å)	15.876(3)	15.804(5)	15.774(3)	15.786(5)	15.742(2)	15.756(5)
ß (°)	90.0	90.18(3)	90.13(2)	90.0	90.41(1)	90.0
Density (g/cm^3)	7.29(Z = 2)	7.37(Z = 2)	7.45(Z = 2)	7.38(Z = 1)	7.58(Z = 2)	7.56(Z = 1)
Formula weight	1047.2	1049.2	1052.5	1045.9	1058.4	1056.2
Max/Min transmission	0.866/0.121	0.382/0.065	0.133/0.037	0.168/0.032	0.411/0.050	0.198/0.065
Extinction (μm)	0.0001(1)	0.0001(1)	0.0001(1)	0.0003	N/A	0.0037
Total reflections	2755	1412	6084	2426	3425	1958
Independent refln's	1412	1195	2024	987	1856	980
R_{int}(%)	1.30	3.03	5.83	3.94	3.49	2.95
Obs.reflns.[I > 3σ(I)]	422	523	1204	465	1143	496
Data/parameters	11.4	10.3	23.2	16.6	21.6	17.7
μ(mm^{-1})	57.170	58.363	59.088	59.936	61.538	61.663
R (%)	5.45	3.80	4.52	4.22	2.83	4.15
R_w(%)	7.89	3.87	5.04	4.77	3.19	5.84
Max shift/e.s.d.	0.001	0.001	0.001	0.001	0.001	0.001

Table 5.1.2 Atomic positions and thermal displacement parameters for $Pb_2Sr_2RCu_3O_8$ (R=La, Pr, Nd, Eu, Tb and Dy). Space groups Cmmm (No.65) for R=La: Pb(*0,0,z*), Sr(*0,0,z*), R(*0,0,0*), Cu1(*0,0,½*), Cu2(*0,½,z*), O1(*¼,¼,z*), O2(*0,½,z*), O3(*x,y,z*); C2/m (No.12) for R=Pr, Nd and Tb: Pb(*x,0,z*), Sr(*x,0,z*), R(*0,0,0*), Cu1(*0,0,½*), Cu2(*x,0,z*), O1(*x,y,z*), O2(*x,0,z*), O3(*x,y,z*); and P4/mmm (No.123) for R=Eu and Dy: Pb(*½,½,z*), Sr(*0,0,z*), R(*0,0,0*), Cu1(*0,0,½*), Cu2(*½,½,z*), O1(*0,½,z*), O2(*½,½,z*), O3(*x,0,z*). The anisotropic thermal displacement parameter exponent has a unit of Å^2 and takes the form: $-2\pi^2(h^2a^{*2}U_{11}+\ldots+2hka^*b^*U_{12})$. K stands for site-occupation. The last-digit in parentheses is the uncertainty.

R		La	Pr	Nd	Eu	Tb	Dy
Pb	x		0.4970(2)	0.4984(1)		0.4959(1)	
	z	0.3899(1)	0.3891(1)	0.3887(1)	0.3881(1)	0.3878(1)	0.3879(1)
	U_{11}	0.029(1)	0.019(1)	0.016(1)	0.013(1)	0.015(1)	0.013(1)
	U_{22}	0.019(1)	0.016(1)	0.014(1)	0.013	0.011(1)	0.013
	U_{33}	0.007(1)	0.007(1)	0.007(1)	0.008(1)	0.007(1)	0.007(1)
	U_{13}		0.000(1)	0.001(1)		-0.000(1)	
Sr	x		0.0018(3)	0.0015(2)		0.0051(1)	
	z	0.2219(2)	0.2223(1)	0.2221(1)	0.2211(1)	0.2210(1)	0.2209(1)
	U_{11}	0.014(2)	0.008(1)	0.014(1)	0.013(1)	0.011(1)	0.013(1)
	U_{22}	0.006(1)	0.011(1)	0.011(1)	0.013	0.010(1)	0.013
	U_{33}	0.007(1)	0.007(1)	0.008(1)	0.009(1)	0.008(1)	0.008(1)
	U_{13}		0.000(1)	0.002(1)		-0.001(1)	
R	U_{11}	0.028(2)	0.012(1)	0.013(1)	0.007(1)	0.006(1)	0.009(1)
	U_{22}	0.016(1)	0.008(1)	0.009(1)	0.007	0.005(1)	0.009
	U_{33}	0.012(1)	0.011(1)	0.008(1)	0.007(1)	0.006(1)	0.004(1)
	U_{13}		-0.002(1)	0.001(1)		-0.001(1)	
	K	1.00	1.00	1.00	0.906(7)	0.955(3)	0.911(8)
Cu1	U_{11}	0.028(4)	0.021(3)	0.012(1)	0.013(1)	0.016(1)	0.012(1)
	U_{22}	0.019(3)	0.018(2)	0.014(1)	0.013	0.013(1)	0.012
	U_{33}	0.013(3)	0.009(2)	0.012(1)	0.011(2)	0.010(1)	0.010(1)
	U_{13}		0.000(2)	0.003(1)		0.002(1)	

(cont'd)

(cont'd)

Cu2	x		0.5008(4)	0.5012(3)		0.5020(1)	
	z	0.1133(2)	0.1111(2)	0.1104(1)	0.1088(2)	0.1068(1)	0.1071(1)
	U_{11}	0.019(3)	0.005(1)	0.011(1)	0.007(1)	0.005(1)	0.008(1)
	U_{22}	0.006(1)	0.005(1)	0.007(1)	0.007	0.005(1)	0.008
	U_{33}	0.009(2)	0.011(1)	0.008(1)	0.010(1)	0.008(1)	0.008(1)
	U_{13}		-0.002(1)	0.001(1)		-0.001(1)	
O1	x		0.2495(14)	0.2486(10)		-0.2482(6)	
	y		0.2471(17)	0.2500(13)		0.2503(7)	
	z	0.1042(9)	0.0993(6)	0.0989(4)	0.0967(6)	0.0942(3)	0.0946(6)
	U_{11}	0.030(10)	0.008(5)	0.013(3)	0.006(3)	0.009(1)	0.014(4)
	U_{22}	0.011(5)	0.005(3)	0.009(2)	0.015(4)	0.007(1)	0.004(3)
	U_{33}	0.016(6)	0.021(5)	0.014(2)	0.016(4)	0.015(2)	0.015(3)
	U_{12}	0.001(7)	0.001(3)	0.001(2)		-0.001(1)	
	U_{13}		-0.005(4)	0.003(2)		0.001(1)	
	U_{23}		-0.004(4)	0.001(2)		-0.003(1)	
O2	x		0.5032(27)	0.4974(20)		0.5053(13)	
	z	0.2530(15)	0.2540(11)	0.2537(7)	0.2539(11)	0.2526(5)	0.254(1)
	U_{11}	0.020(14)	0.016(9)	0.020(4)	0.027(5)	0.019(3)	0.031(6)
	U_{22}	0.017(9)	0.030(8)	0.026(6)	0.027	0.024(3)	0.031
	U_{33}	0.010(9)	0.010(9)	0.007(3)	0.007(5)	0.007(2)	0.010(5)
	U_{13}		0.003(7)	0.002(3)		-0.003(2)	
O3	x	0.9315(73)	0.0346(41)	0.0293(33)	0.8542(94)	0.0548(16)	0.866(10)
	y	0.0812(51)	0.0753(35)	0.0648(44)		0.0756(17)	
	z	0.3808(25)	0.3855(13)	0.3871(13)	0.3831(26)	0.3850(7)	0.387(2)
	U_{11}	0.018(30)	0.078(16)	0.055(12)	0.048(22)	0.027(4)	0.027(15)
	U_{22}	0.001(9)	0.016(9)	0.022(10)	0.016(12)	0.012(3)	0.005(8)
	U_{33}	0.032(22)	0.008(8)	0.056(12)	0.046(23)	0.019(4)	0.038(18)
	U_{12}	0.001(18)	-0.007(11)	-0.002(8)		0.002(4)	
	U_{13}	0.003(21)	-0.002(11)	0.031(10)	0.021(19)	0.002(4)	-0.009(14)
	U_{23}	0.022(12)	0.000(8)	0.003(10)		-0.001(3)	

Table 5.1.3 Selected bond lengths (Å) for $Pb_2Sr_2RCu_3O_8$ (R = La, Pr, Nd, Eu, Tb and Dy).

R	La	Pr	Nd	Eu	Tb	Dy
Pb-O2x1	2.172(24)	2.135(17)	2.130(10)	2.119(17)	2.144(6)	2.116(16)
-O3x1	2.340(29)	2.338(19)	2.386(24)	2.358(21)	2.357(8)	2.375(22)
x1	2.402(40)	2.556(22)	2.578(18)	2.358	2.401(8)	2.375
x1	3.140(27)	2.963(20)	2.911(25)	3.116(21)	3.064(8)	3.092(19)
x1	3.225(35)	3.160(15)	3.093(19)	3.116	3.131(8)	3.092
Sr-O1x2	2.692(10)	2.753(9)	2.744(6)	2.748(7)	2.766(4)	2.763(7)
-O1x2	2.692	2.731(9)	2.733(6)	2.748	2.770(4)	2.763
-O2x2	2.797(4)	2.786(3)	2.779(2)	2.769(3)	2.766(1)	2.759(3)
x1	2.774(4)	2.779(15)	2.744(11)	2.769	2.737(7)	2.759
x1	2.774	2.768(15)	2.789(11)	2.769	2.756(7)	2.759
-O3x1	2.589(40)	2.618(21)	2.630(21)	2.619(40)	2.647(9)	2.672(37)
R-O1x4	2.549(9)	2.477(9)	2.475(6)	2.455(6)	2.425(4)	2.427(6)
-O1x4	2.549	2.503(9)	2.487(6)	2.455	2.426(4)	2.427
Cu1-O3x2	1.981(40)	1.865(21)	1.823(21)	1.929(40)	1.858(9)	1.849(37)
Cu2-O1x2	1.944(1)	1.936(9)	1.928(7)	1.932(1)	1.926(3)	1.927(1)
-O1x2	1.944(1)	1.949(9)	1.947(7)	1.932	1.932(3)	1.927
-O2x1	2.218(25)	2.259(17)	2.261(10)	2.290(17)	2.280(6)	2.317(17)

5.2 Crystal symmetry and oxygen ordering in the PbO layer

Various tetragonal, orthorhombic and monoclinic space groups have been assigned to several Pb-2213 phases in the literature: P4/mmm[101] and Pman[131] for $Pb_2Sr_2(Y/Ca)Cu_3O_{8+\delta}$ crystals, Cmmm[100], or a combination of Cmmm and $P\bar{1}$[133], Pmmm[126] and $P2_1/m$[134] for the Ca-free 2213 compounds and $P22_12$[103] for $Pb_2Ba_2YCu_3O_8$ ... etc. No structural difference has been observed between the Ca-doped and Ca-free 2213 phases since no Ca ordering has been observed in the former[135]. The crystal structures refined in different space groups are nearly identical because all the atoms in the unit cell sit on special positions except for O3 which is symmetry dependent. For each O3, there are four closely-spaced sites available in Cmmm and P4/mmm, two in Pman and C2/m, but only one in $P2_1/a$ where the positions of O3 are related by an inversion centre. It is worth pointing out that the coordination environment for the Pb^{2+} ion does not change with the choice of different space groups, i.e. C2/m, Cmmm and P4/mmm ———— there are always two sets of in-plane Pb-O3 bond lengths ($\sim$2.4Å and $\sim$3.1Å, cf. table 5.1.3).

The structure refinements of four of the $Pb_2Sr_2RCu_3O_8$ compounds were carried out in either Cmmm (R=La) or C2/m (R=Pr, Nd and Tb) by neglecting very weak reflections which violate the C-centering condition. Thus the lattice type is certainly primitive. The very weak reflections arise, most likely, from oxygen atoms in the PbO layers and a definitive structure determination will require information from neutron diffraction as well. The other two structures, R=Eu and Dy, were refined in tetragonal symmetry, P4/mmm. The true symmetry here is either monoclinic or orthorhombic and the pseudo-tetragonal symmetry reflects a (*110*) twinning. Thus, the structures for

R=Eu and Dy represent an average of the two twin components which will be addressed later in §5.6. Although the crystal structures refined here are subject to the shortcomings indicated above, they represent a fairly good approximation to the true structure and are of sufficient accuracy to provide reliable information regarding electron densities at the R-site and R-O1 distances which are crucial to arguments to be made later in Chapter 6. This is because the R atoms occupy the origin in all of the space groups utilized and the O1 atoms are at (¼,¼,*z*) positions, even for the three monoclinic crystals where the position is (*x*,*y*,*z*), the *x* and *y* values are within 2σ of ¼ in all cases.

5.3 Monoclinic distortion

A monoclinic distortion in the $Pb_2Sr_2YCu_3O_8$ compound was first reported by Fujishita et al.[134] But their refinement of a powder x-ray diffraction pattern was not very convincing because all the oxygens in the unit cell were constrained to have a single isotropic thermal parameter and the R_{wp} of 7.2% was relatively high. Our structure refinements on three Ca-free $Pb_2Sr_2RCu_3O_8$ (R=Pr, Nd and Tb) single crystals showed a definite monoclinic distortion with ß values ranging from 90.13° to 90.41°. The R-indices of R=2.83% and R_w=3.19% for $Pb_2Sr_2TbCu_3O_8$ indicate that the structure refinement was very good (better than any structure refinement of the 2213 phase reported thus far). The monoclinic unit cell is not very different from the C-centered orthorhombic one (cf. figures 5.1b & c). The monoclinic distortion of those crystals with R=Pr, Nd and Tb can be seen clearly in the (*010*) projection as illustrated in figure 5.3 where the P-unit and the metal sublattice in the RS-unit are shifted with

respect to each other along the a-axis meanwhile both retain their orthogonality. The oxygens in the upper PbO layer are shifted correspondingly with the P-unit along $<\bar{1}00>$ and those in the lower PbO layer, along $<100>$. Consequently, the bonding between the P- and RS-units is strengthened by this glide as evidenced by the short Pb-O2 and Sr-O3 bonds (see table 5.1.3). This contradicts the conclusion drawn by Zandbergen et al.[136] that interaction between the SrO and PbO layers is the weakest interlayer interaction. A monoclinic distortion (with a distortion angle of 100.01° in the case of R=Tb) of the oxygen sublattice in the RS-unit as shown in figure 5.3b by the dotted lines, seems to be the most distorted structural unit which could supply a ground for the monoclinic distortion of the whole unit cell.

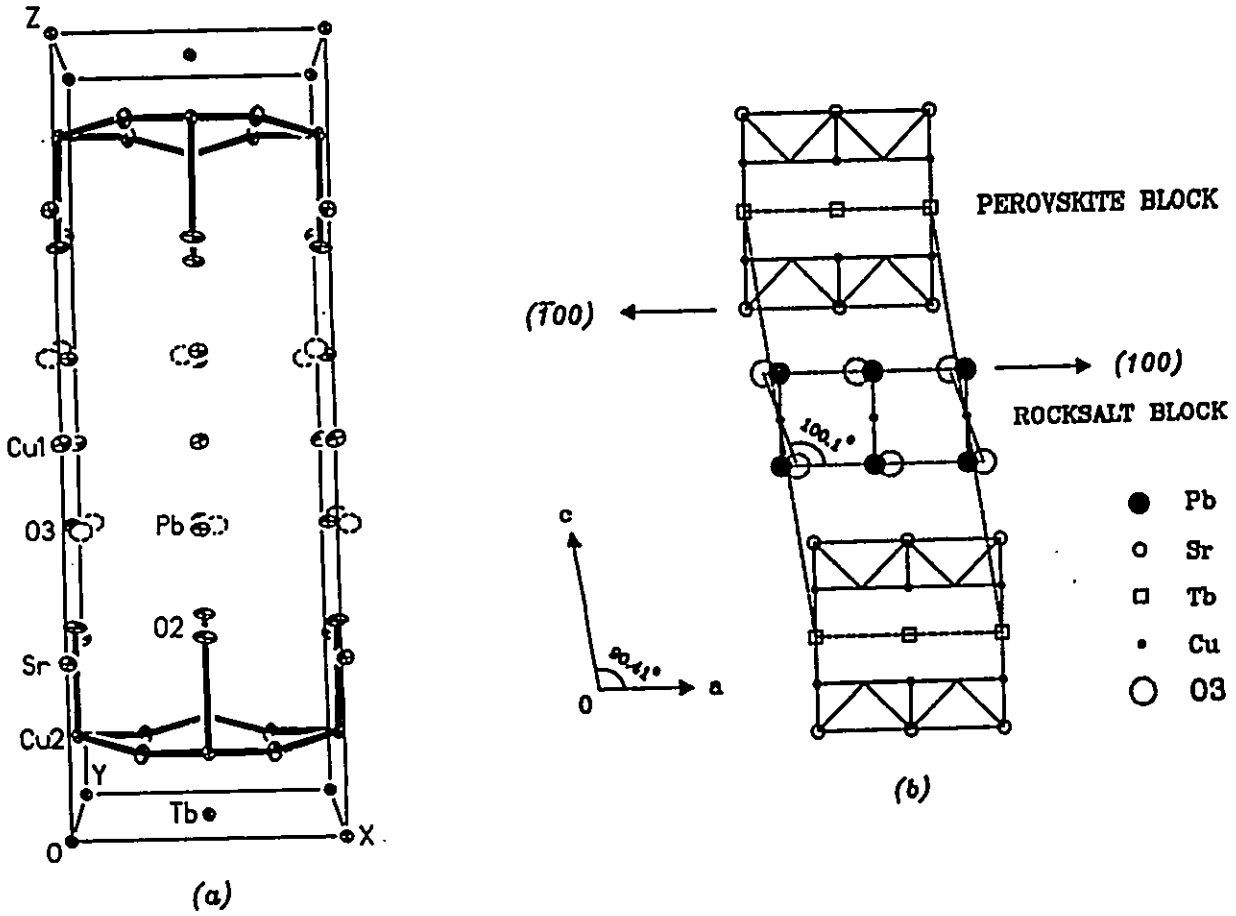

Figure 5.3 (a) 3-D and (b) 2-D (*010*) projections showing a monoclinic distortion of the unit cell of $Pb_2Sr_2TbCu_3O_8$.

5.4 Orientation of the lone pair electrons

Now one may want to know what is the driving force responsible for the monoclinic distortion of the oxygen sublattice in the RS-unit? The answer is the electric negativity of the lone pair residing on the Pb^{2+}. As we know, the outer shell of Pb^{2+} has twelve valence electrons ($5d^{10}6s^2$) which are usually non-bonded. The electrons in the Pb-O bonds are supplied by the full shell O^{2-} while the d electrons are symmetrical and have little effect on the coordination. The $6s^2$ electrons can be symmetrical or, by hybridising with p orbital they can become asymmetric and form a stereo-active electron pair which is the so-called "lone pair". Ideally, the PbO_5 can have a pseudo-octahedral geometry (or AB_5E) as shown in figure 5.4.1a. But a serious problem raised here is that the lone pairs on the Pb^{2+} ions in the upper and lower PbO layers respectively are pointing towards each other, a strong Coulomb repulsion between them will force them to re-orient somehow as shown in figure 5.4.1b. The re-oriented lone pair will push the two in-plane O3 away from the Pb^{2+} ion and give rise to two long Pb-O3 bonds (~3.1Å) and at the same time the other two will be pushed in and the result is two short bonds (~2.4Å) (figure 5.4.1c). Together with a short apical Pb-O2 bond (~2.1Å), the Pb^{2+} ion is in a very distorted five-fold polyhedron. Cava et al.[100] have postulated that the lone pair on the Pb^{2+} is oriented roughly normal to (but directed away from) the triangular face formed by the three shortest Pb-O bonds based on the crystal structure refined in Cmmm. Obviously, there are a number of combinations for the direction of the lone pair in the case of the Cmmm or P4/mmm space groups because each O3 can randomly occupy one out of four sites and there are sixteen sites available in the two PbO layers per unit cell. The

situation in C2/m is simpler since there are only two sites available for each O3. As mentioned earlier in §5.2, the coordination environment of the Pb ions does not change with the choice of different space groups, thus the same postulate discussed above should be applicable to the monoclinic case. Thus, the direction of lone pair will be normal to the triangular (hatched) area as shown in figure 5.4.1b. Notice that the finding of this work is that the lone pairs point between the Cu1 ions (figures 5.4.1b & c) rather than towards the Cu1 ions as ascribed by Cava et al.[100] A better O3 ordering can be established by assuming all the lone pairs in the same PbO layers pointing to the same direction and in this way the potential energy of the crystal lattice can be lowered. According to these hypotheses, the mechanism of monoclinic distortion in the Ca-free $Pb_2Sr_2RCu_3O_8$ crystals can be summarized by the following progression:

lone pair ordering _____ distortion of O3 sublattice _____ glide between P- & RS-units _____ monoclinic distortion

Figures 5.4.2a and b show the (*001*) projections of the displaced oxygens in the lower and upper PbO layers, respectively. By overlapping these two projections, one can obtain a familiar picture of four split O3 sites (figure 5.4.2c) which has been seen in the orthorhombic and tetragonal cases. This is interesting because a better oxygen ordering in the PbO layers occurs in a structure refined in the low symmetry space group C2/m than that in the high symmetry space groups Cmmm or P4/mmm.

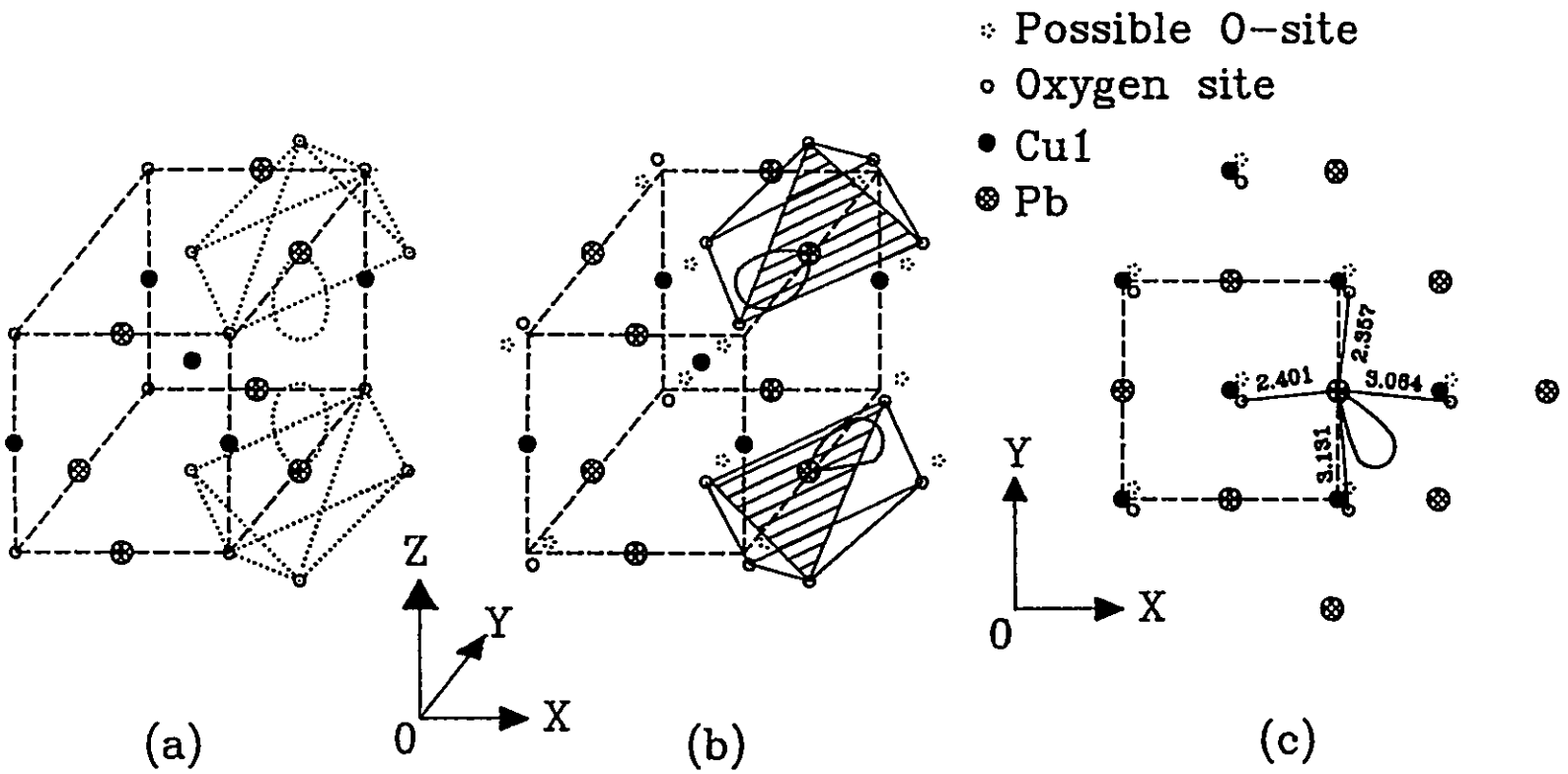

Figure 5.4.1 lone pairs of Pb^{2+} in the lower and upper PbO layers (a) pointed to each other, (b) directed normal to the triangular (hatched) area and pushed two in-plane O3 away from the Pb^{2+} and (c) (*001*) projection showing the lower PbO and Cu1 layers and the in-plane Pb-O3 bond lengths.

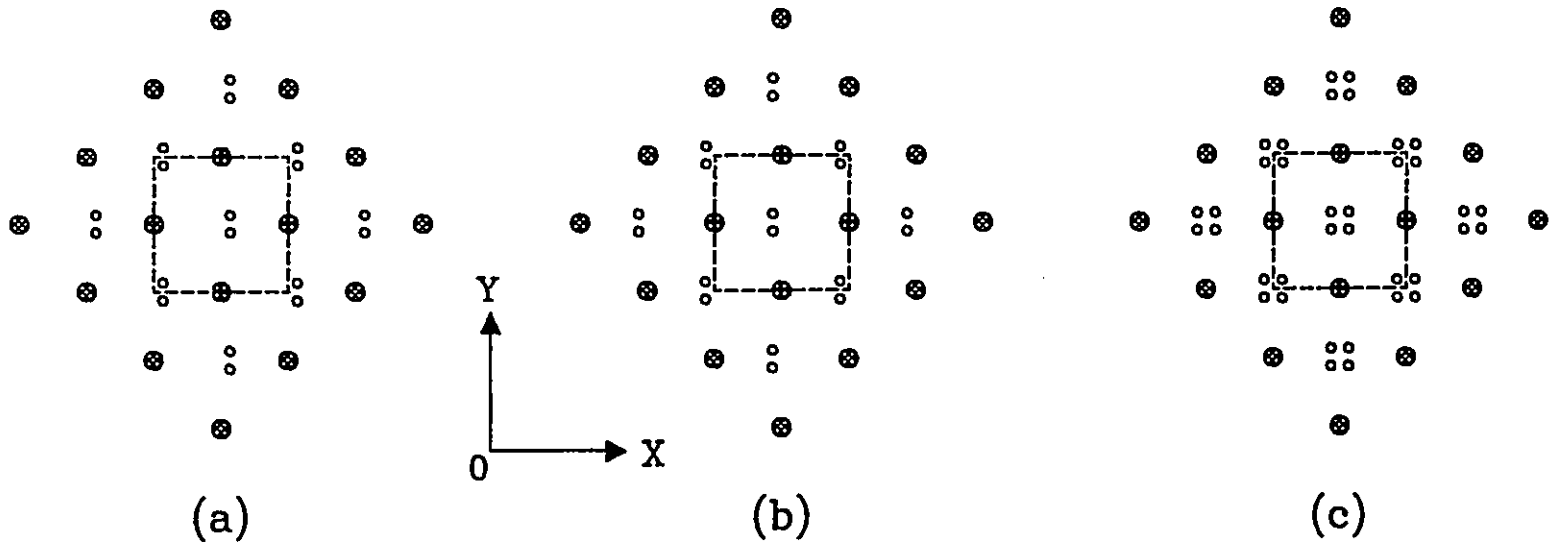

Figure 5.4.2 Oxygen ordering of (a) the lower PbO layer, (b) the upper PbO layer in the monoclinic symmetry and (c) the PbO layers in the orthorhombic symmetry.

5.5 Origin of orthorhombicity*

The origin of the orthorhombic distortion in the Pb-2213 phase has been a puzzle since the compound was discovered. Most authors believe that the displacement of O3 in the PbO layers is responsible for this distortion[100,127,133]. A question raised here is why they displace unevenly along the a- and b-axes? The electron microscopic work conducted by Zandbergen et al.[136] shows that those reflections corresponding to the 5.4Å cell disappear upon interaction with a strong electron beam which causes a reduction of the specimen under the high vacuum of the electron microscope, while the resultant 3.8Å cell is still orthorhombic. This suggests that the orthorhombicity may be related to a structural distortion other than the oxygen ordering in the RS-unit, for instance, a positional shift of the Pb atoms or the tilting of CuO_5 pyramids in the P-units. However, neither positional shifts nor any anomaly in the thermal parameters of Pb^{2+} or those oxygens associated with the CuO_5 pyramids have been found in our structural refinements. All the known high-T_c superconducting copper oxides containing ions with a $5d^{10}$ configuration (without lone pair electrons), i.e. Pb^{4+} or Tl^{3+} are tetragonal, while those containing Pb^{2+} or Bi^{3+} ($5d^{10}6s^2$) which possess lone pair electrons, are orthorhombic (cf. tables 2.4.1 & 2.4.2). This strongly suggests that the orthorhombicity in the Pb-2213 phase is correlated with the lone pair of Pb^{2+}. The source of orthorhombicity may be traced back to the synthetic process where a tetragonal to orthorhombic phase transition for $Pb_2Sr_2GdCu_3O_8$ at 750°C upon

---

* The term orthorhombicity is used here to denote the situation that b>a for both orthorhombic and monoclinic symmetries.

cooling was first observed by Gallagher et al.[120] Subsequently, Kadowaki et al.[102] and Jorgensen[137] showed the similar results for the Ca-doped and Ca-free compounds, respectively. Obviously, the lone pairs of the Pb^{2+} ions will be easier to fit in an expanded, high temperature unit cell than a smaller room temperature cell. The thermal motion at high temperature leads to a random orientation of the lone-pairs. Therefore a tetragonal symmetry will be a better description for the high temperature cell. These lone pairs start to condense into the space available in the oxygen-free Cu^{I} layers upon cooling. As the temperature drops to 750°C, the distance between the two PbO layers also decreases and the strong Coulomb force triggers an ordering process among the lone pairs. Figures 5.5a, b and c show the (*010*) and (*001*) projections of the lone pair ordering between the upper and lower PbO layers. The uneven displacement of the oxygens in PbO layers is due to the fact that the direction of lone pairs deviates from the body-diagonal line of the RS-unit (the dotted lines in figure 5.5), therefore they push the O3 more along the b- than a-axes. Since the orthorhombicity is formed at a relatively high temperature (though lower than 750°C), it tends to maintain its integrity even when the ordering of oxygens in the PbO layers is destroyed by the strong electron beam.

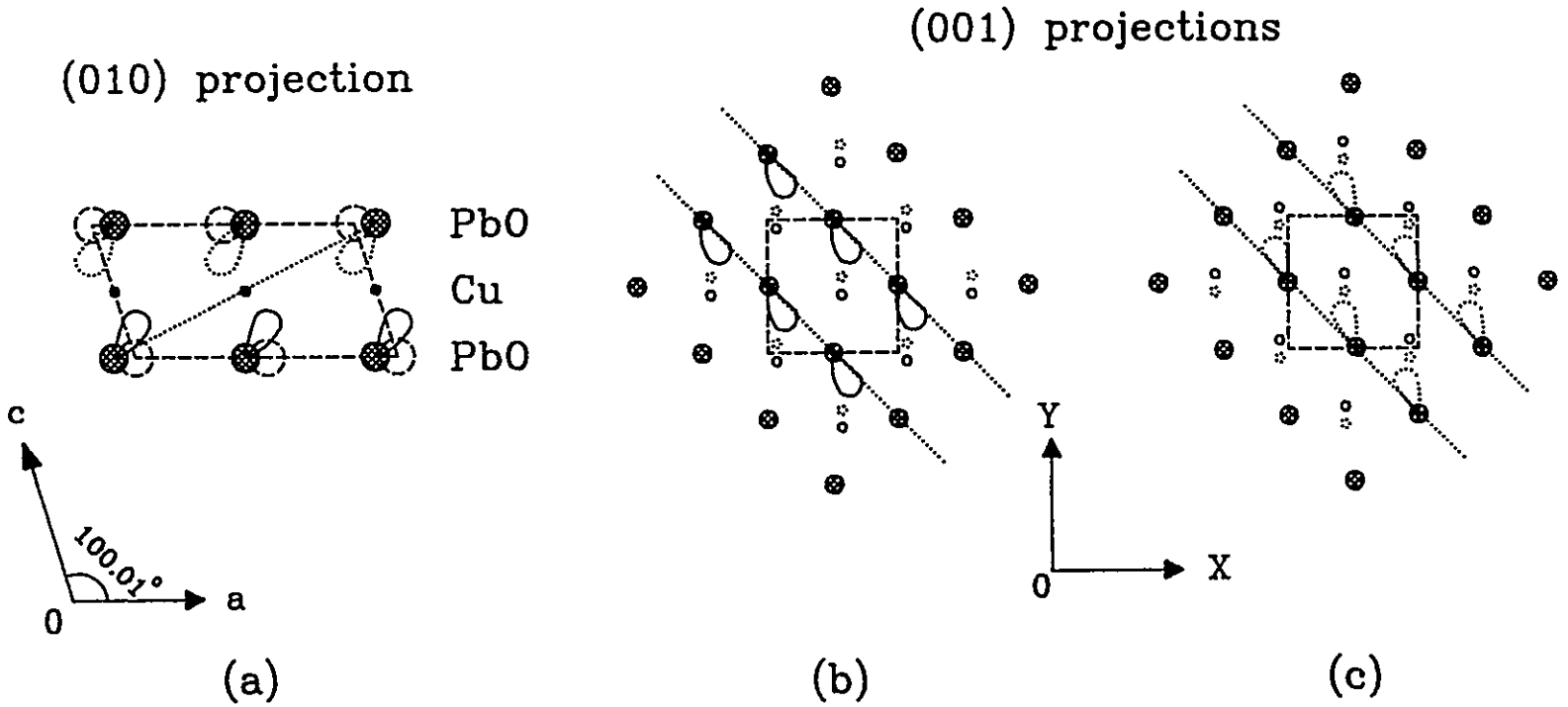

Figure 5.5 (*010*) and (*001*) projections of the lone pair ordering in (a) the RS-unit, (b) the lower and (c) upper PbO layers, respectively.

5.6 Possible (*110*) twinning

The oxygen ordering process in the PbO layers can initiate in different parts of a crystal, and thus a domain structure could be formed such as the (*110*) micro-twinning observed by Hewat et al.[138] Figure 5.6 shows a (*110*) twin model which is constructed by two monoclinic domains of the PbO layers. Within each domain, only one out of two closely-spaced oxygen sites should be filled. A possible ordering of O3 has also been shown in figure 5.6, where all the lone pairs in one domain are oriented in the same direction. If the domain sizes are of the same order of magnitude or less than the x-ray diffraction correlation length and the volume fraction of each twin domain is nearly 50%, a tetragonal symmetry could be obtained as an average of two monoclinic domains. In this case, the tetragonal a-axis should be related to the monoclinic (or orthorhombic) cell by $a_t = (a_m + b_m)/2\sqrt{2}$. For example, the lattice parameters of crushed crystal fragments from the same growth batch as those used in the structure refinement obtained by the high resolution Guinier powder x-ray diffraction are a = 5.421(1)Å, b = 5.459(1)Å for R = Eu, and a = 5.398(1)Å, b = 5.432(2)Å for R = Dy. These values are in fairly good agreement with the tetragonal lattice parameters deduced by single crystal x-ray diffraction. These observations also indicate that the twin domain size distribution is inhomogeneous within the crystals in a given batch. Attempt to deconvolve the twinning by refining a twinning parameter on the single crystal x-ray diffraction data was unsuccessful in one case[109]. But a twinning parameter of ~54% was refined on a $Pb_2Sr_2(Y/Ca)Cu_3O_8$ crystal using the single crystal neutron diffraction technique.[131]

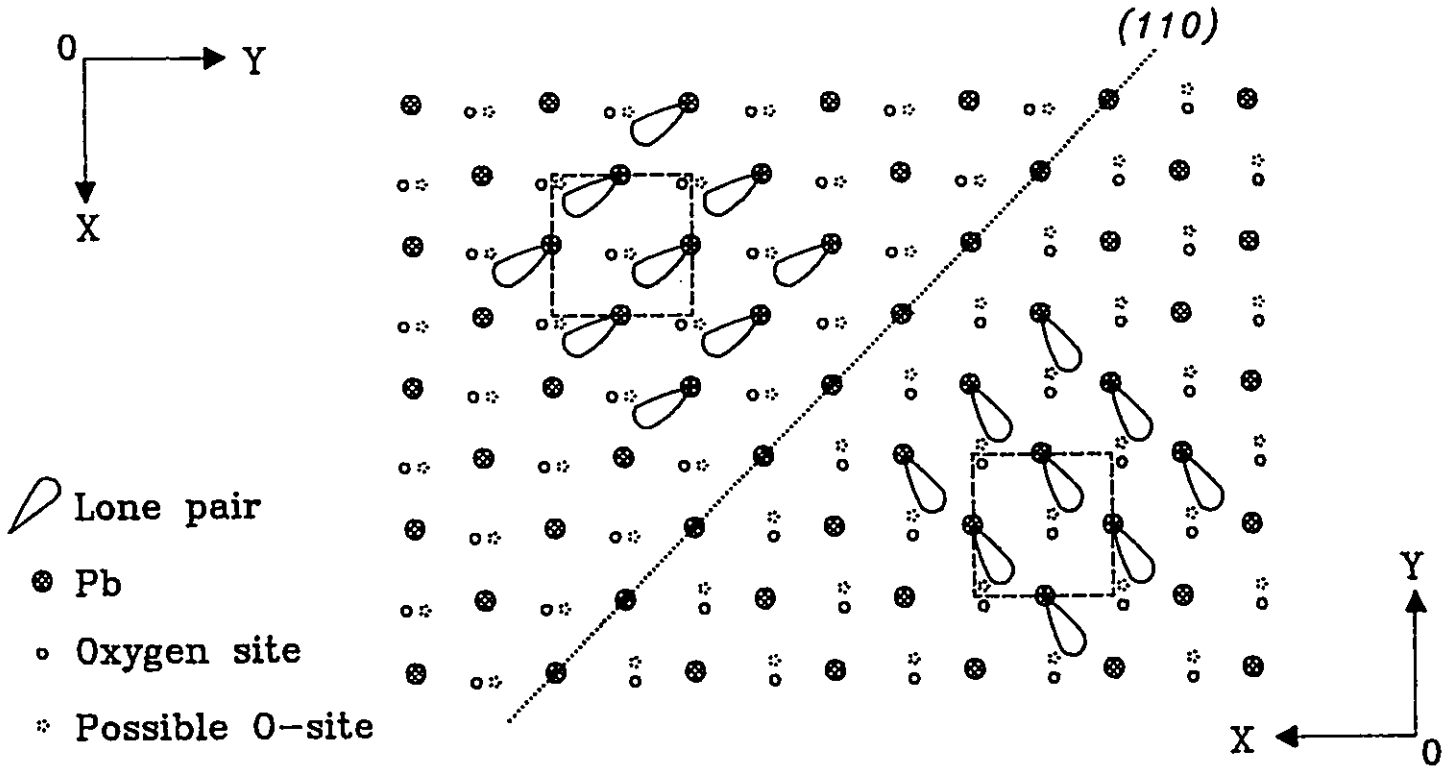

Figure 5.6 Possible (*110*) twinning due to two monoclinic PbO domains.

5.7 Bond valence sum calculation

Bond valence sums (BVS) for each ion in the unit cell of $Pb_2Sr_2RCu_3O_8$ (R = La, Pr, Nd, Eu, Tb and Dy) have been calculated using the following expression:

$$V = \Sigma s_i = \Sigma \exp[(r_0 - r_i)/ß] \qquad (5\text{-}7)$$

where, V is the bond valence sum and is expected to equal approximately the oxidation state of the ion around which the valences have been summed. r_i and s_i are the observed bond lengths and valence of bond i, respectively, which are formed between the cations and anions. The values of r_0 and ß have been calculated by Brown and Altermatt[139]. The results are shown in table 5.7. Firstly, almost all of the BVS for Cu2 are higher than the formal oxidation state +2, and the BVS's for Sr and O2 are lower. Since the BVS reflects the distribution of valence in the bonds about a given ion, it will be increased by shortening and decreased by lengthening the bonds. Thus the Cu2-O1 bonds in the CuO_2 planes are compressed and the Sr-O2 bonds are stretched. Furthermore, a bond valence sum of +2.0 for Pb indicates that the PbO layers are not stressed by the cell dimension constraints. Presumably, any strains in the PbO planes are relaxed by the disordering of the O3 atoms. A tension along the c-axis in the RS-units is also evidenced by the low BVS of O3. A bond valence sum close to +1.0 for the Cu1 ions is consistent with the absence of oxygen in these layers as found in the structure refinement since strain can not be built up within the basal plane without Cu1-O bonds. Secondly, the BVS of the Cu2 ions is essentially constant as a function of R. This may seem surprising since from table 5.1.3 the Cu2-O1 bond lengths clearly decrease with R. Note however, that the Cu2-O2 bond lengths change in the opposite sense, increasing as R decreases. The result is an

average Cu2-O bond length of 2.00(1)Å nearly constant with R and thus a constant BVS for all six $Pb_2Sr_2RCu_3O_8$ (R = La, Pr, Nd, Eu, Tb and Dy) crystals. Thirdly, from the structure refinement, electron density deficiencies were found at the Eu, Tb and Dy sites while full occupancy was observed for R = La, Pr and Nd. The calculated bond valence sums for La, Pr and Nd are close to their valence state +3 and those for Eu, Tb and Dy are significantly less, which agree with the refinement results and are comparable with that of the R = Y/Ca crystals.

Residual strains in the crystal structure of $Pb_2Sr_2RCu_3O_8$ are illustrated in figure 5.7 with the aid of generalized bond valence sums. Obviously, most strains dwell in the P-units. The R layers are strain-free due to lack of oxygen, while the compression in the CuO_2 plane is balanced by the tension in the SrO layers. Compared with the rigid P-unit, RS-unit fits much better with the lattice dimension constraint denoted by the two vertical dotted lines in figure 5.7 due to the flexibility supplied by the displacement of O3 and the oxygen-depleted Cu1 layers.

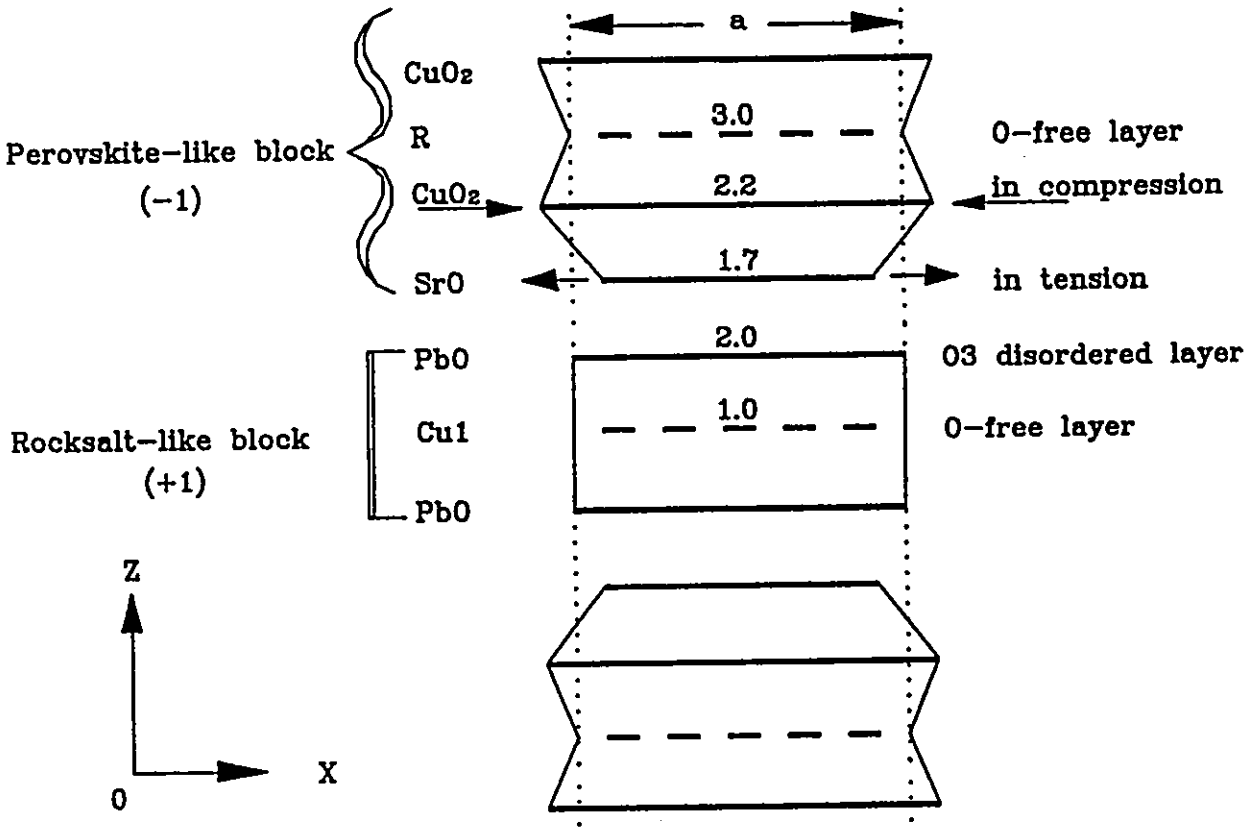

Figure 5.7 Schematic diagram of generalized bond valence sums in various metal oxygen layers showing the residual strains in the crystal structure of $Pb_2Sr_2RCu_3O_8$.

Table 5.7 Calculated bond valence sums for $Pb_2Sr_2RCu_3O_8$ (R = La, Pr, Nd, Eu, Tb, Dy and Y/Ca[101]).

	La	Pr	Nd	Eu	Tb	Dy	Y/Ca
Pb	1.96	1.94	1.90	2.14	2.05	2.11	1.87
Sr	1.79	1.67	1.69	1.67	1.65	1.63	1.77
R	2.89	3.09	2.90	2.59	2.64	2.30	2.55
Cu1	0.71	0.98	1.09	0.82	1.00	1.02	0.91
Cu2	2.19	2.17	2.20	2.21	2.23	2.23	2.34
O1	-2.12	-2.13	-2.09	-2.02	-2.02	-1.95	-2.07
O2	-1.74	-1.82	-1.84	-1.86	-1.83	-1.88	-1.80
O3	-1.75	-1.75	-1.75	-1.83	-1.87	-1.86	-1.79

CHAPTER 6

CATION VACANCIES IN THE Ca-FREE $Pb_2Sr_2RCu_3O_8$ CRYSTAL SERIES

As mentioned in §1.5, the mobile carriers in the CuO_2 planes can be created via several mechanisms: 1) chemical substitution, 2) oxygen vacancies, 3) cation vacancies at the non-copper sites, 4) interstitial oxygen, and 5) an internal redox reaction. Among them, only mechanisms 1 and 2 are well established. Mechanism 3 is controversial since cation vacancies have been observed only in the 2212 and 2201 phases of the bismuth and thallium cuprates before this work[27,28,29,30,140]. Previous studies of the lead cuprate superconductors have focussed on mechanisms 1 and 2. Ca-free $Pb_2Sr_2YCu_3O_8$ has been concluded to be a nonsuperconducting insulator[7,126] rather than a metal as suggested by band structure calculations[141]. Attempts to make this compound superconducting via various oxygen annealing procedures were unsuccessful because the holes created by oxygen addition are not transferred to the CuO_2 planes, and instead, oxidize the Pb^{II} and Cu^{I} ions in the RS-unit[24,134]. In this chapter, we will present the evidence for the existence of cation vacancies at the R-site for R = Eu, Gd, Tb, Dy and Y, and show that the observation of a transition from insulating to metallic and superconducting behaviour as a function of decreasing ionic radius of the rare-earth elements in Ca-free $Pb_2Sr_2RCu_3O_8$ single crystals[130] is due to a cation vacancy carrier-doping mechanism. We have established that T_c up to 75K is possible in nonstoichiometric samples using dc resistivity and

magnetic flux exclusion measurements. The suppression of superconductivity in the Tb crystals is also discussed.

6.1 Metal-insulator transition

Optical measurements conducted by M. Reedyk et al.[130] suggest that the Ca-free crystal series can be roughly categorized into three groups in terms of the carrier-doping levels: an insulating group for R=La, Ce, Pr and Nd with basically no hole-doping, a lightly doped group with R=Sm, Eu, Gd and Tb, and a poorly metallic group which includes those crystals with small R's (Dy, Ho and Y). This can be seen from figure 6.1.1 which shows the mid-infrared reflectance of these crystals. Ce, Pr and Nd show a low and essentially flat, and featureless reflectance in the mid-infrared region which is characteristic of an insulator, while that of Dy, Ho and Y increases monotonically with decreasing frequency in this region, and approaches 70% near 1000 cm^{-1}, more typical of a poor metal. The mid-infrared reflectance of the lightly doped materials (Sm, Eu, Gd and Tb) is intermediate between that of these other two groups. The small slope suggests the presence of a small number of carriers. DC resistivity measurements show that the crystals with large rare-earth elements (R=La, Ce, Pr and Nd) are insulators, those with small R's (i.e. Dy, Ho and Y) are metallic and the medium size rare-earths (R=Sm, Eu, Gd and Tb) are near the metal-insulator (M-I) transition (see figures 6.1.2a & b). An insulator-superconductor transition, starting from R=Eu, happens near the M-I transition. Note that the results for Tb are anomalous in one respect. Aithough the optical measurement indicates a comparable carrier concentration in the R=Tb crystal to the other lightly doped members,

resistivity measurement showed it to be nonsuperconducting in contrast to its neighbours Gd and Dy. More discussions on the R=Tb crystals are found later in §6.5.

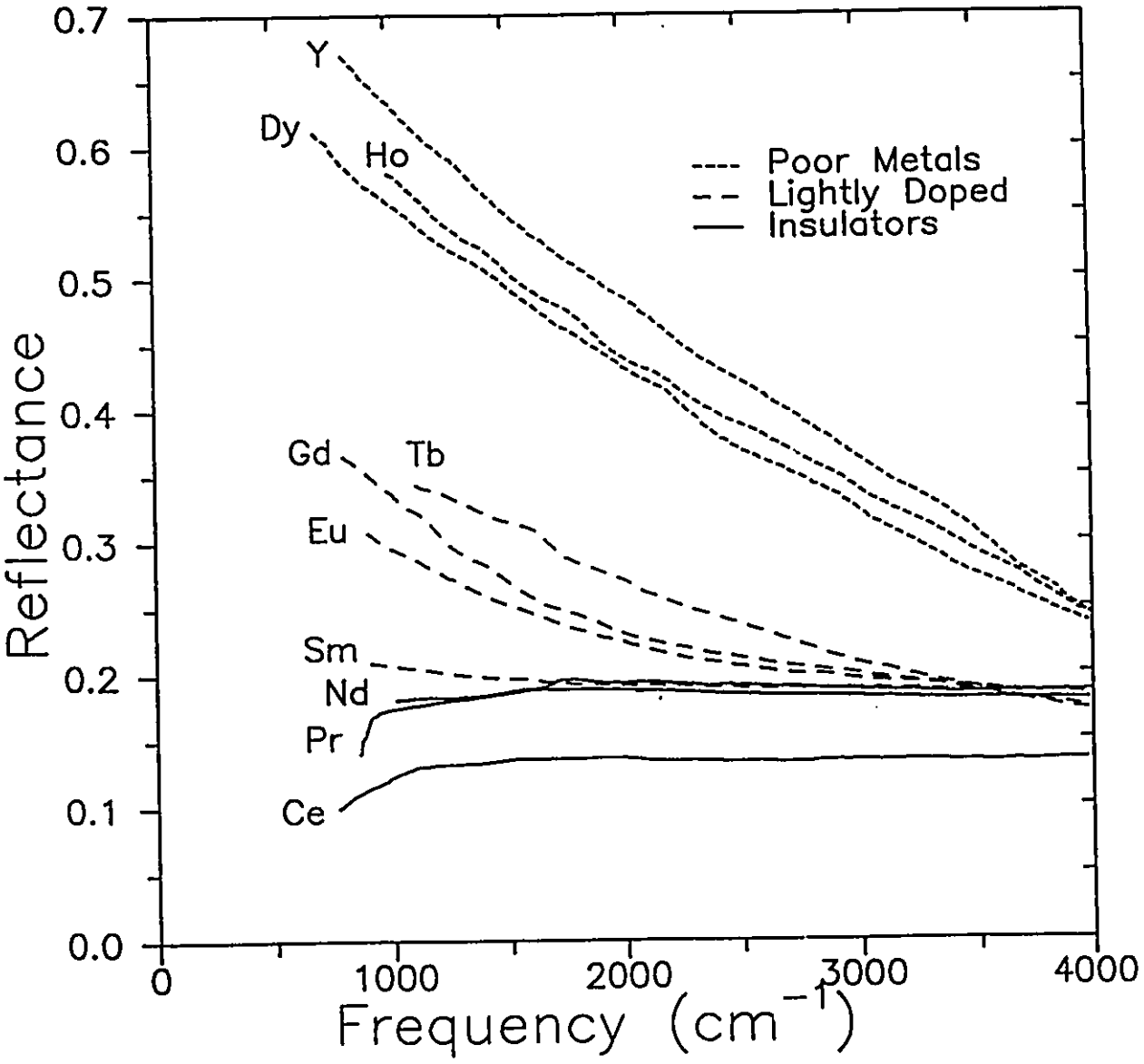

Figure 6.1.1 Mid-infrared reflectance of the $Pb_2Sr_2RCu_3O_8$ single crystals showing that the series can be divided into three groups as indicated in the legend.

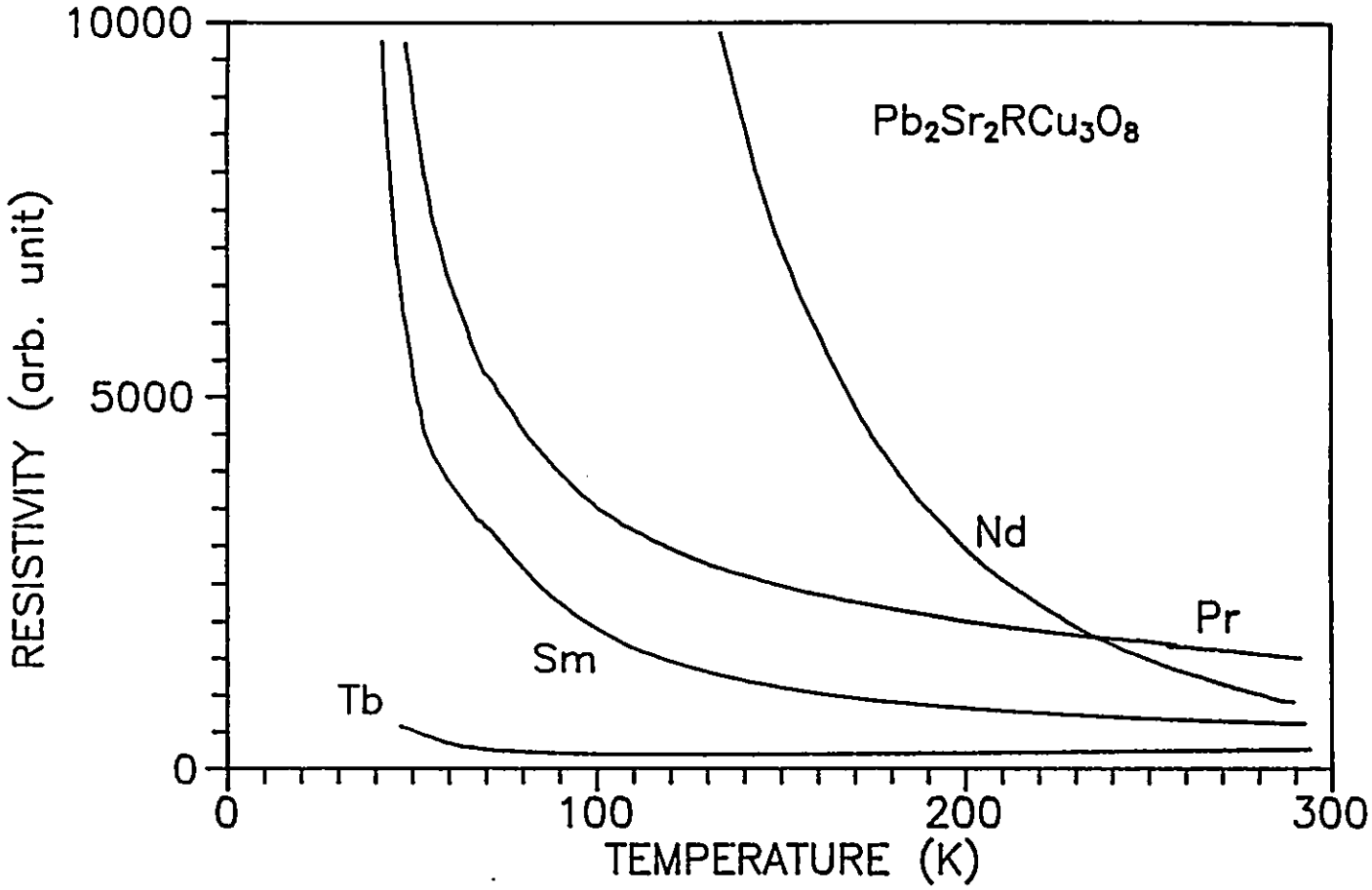

Figure 6.1.2 (a) DC resistivity measurements of the $Pb_2Sr_2RCu_3O_8$ single crystal series showing that the crystals with R = Pr, Nd, Sm and Tb are semiconducting.

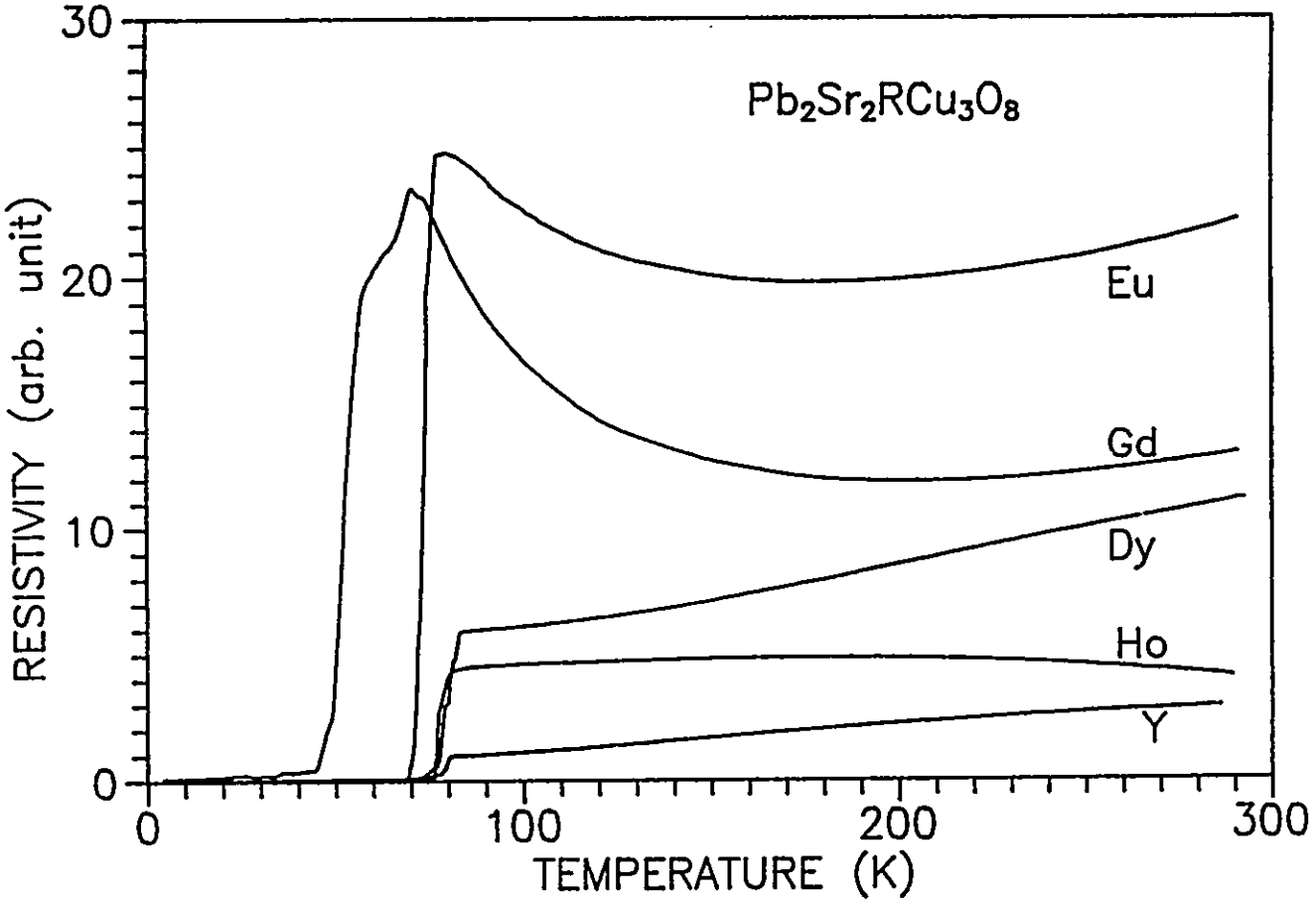

Figure 6.1.2 (b) DC resistivity measurements of the $Pb_2Sr_2RCu_3O_8$ single crystal series showing that those with R=Eu, Gd. Dy, Ho and Y are increasingly more metallic and superconducting.

6.2 Existence of cation vacancies

As mentioned previously and as shown in table 5.1.2 electron density deficiencies were found at the R-site by the structure analysis for three of the crystals, R=Eu [9.4(7)%], Tb [4.5(3)%] and Dy [8.9(8)%] but not for R=La, Pr or Nd. Our result for R=Nd is at variance with two previous structural studies of crystals with nominal composition $Pb_2Sr_2NdCu_3O_8$[7,127]. In both cases the R-site occupation was refined as the mixture $Nd_{1-x}Sr_x$ with $x \approx 0.24$, reflecting an electron density deficiency as Sr has fewer electrons than Nd. Comparison of the reported lattice parameters of those crystals which were grown from a PbO flux show significant differences, a=5.435(1)Å, b=5.463(1)Å, c=15.817(3)Å[7] and a=5.437(3)Å, b=5.472(2)Å, c=15.797(7)Å[127], especially in the c parameter, with those reported for our crystal (see table 5.1.1) which was grown from a PbO/NaCl flux. It is quite likely that the composition of the crystals is different due to different growth techniques. No independent chemical analysis was reported for the crystals of references 7 and 127.

Returning to the cases R=Eu, Tb and Dy for which deficiencies were found it is clear that there are basically two models which might account for this observation, namely doping of that site with an atom of lower electron density such as Sr or Na from the flux, or the presence of cation vacancies. It is of course impossible to discriminate between these models by refinement of occupational factors alone. EDX analysis of the crystals shows no detectable Na content, which leaves only Sr. The concentration of Sr needed is of the order ~23% as mentioned earlier. Such an excess should be detectable by chemical methods. Table 6.2 shows the results for ICP/MS and EPMA analysis on the crystals from the same growth batches from which

the crystals for structure determination were selected. There is no evidence for excess Sr at the required levels for R = Eu, Tb, Dy and Y and in fact the Sr content is the same within error as that for R = Pr and Sm which show no rare-earth deficiency and no Pr-site electron deficiency as well. There is even some evidence that the R-site ion concentration is systematically lower for R = Eu, Tb, Dy and Y compared to R = Pr. The actual values obtained are in reasonable agreement with the refined occupations. The scatter in the Pb content deduced by chemical analysis may be due to the high volatility of Pb or the presence of residual PbO flux on the crystal surfaces or in cracks.

The systematic behaviour of the R-O1 distances versus ionic radii of R can also be used to discriminate between the two models. In figure 6.2 these distances are plotted as a function of the effective R^{3+} radius for VIII-fold coordination[118]. Also plotted, as open circles, are the expected R/Sr-O1 distances for R = Eu, Tb and Dy assuming 23% Sr^{2+}. The dashed line shows the calculated R-O1 distances assuming IV-fold coordination for $O1^{2-}$. The $O1^{2-}$(IV) radius is used to calculate R-O1 because the best agreement between observed and calculated R-O1 distances is obtained. In fact the choice of a radius is somewhat arbitrary. Although O1 has six neighbours the distances are ~1.9Å (2Cu), ~2.4Å (2R) and ~2.7Å (2Sr) and O1(IV) seems a reasonable compromise. It is clear that the calculated R/Sr-O1 distances are much too long, reflecting the large size of Sr^{2+}, 1.26Å, relative to the lanthanides, 1.160Å for La^{3+} to 1.027Å for Dy^{3+}. This points to a further difficulty with the Sr-substitution model, i.e. it is necessary to invoke large amounts of Sr/R mixing for those cations with the largest size mismatch percentages 16.7% for Eu^{3+} to 20.4% for Dy^{3+}. Thus, on the basis of the chemical analysis and the R-O1 bond length analysis the R/Sr mixed-occupation model seems untenable while the cation vacancy model is consistent

with all experimental results.

Table 6.2 Chemical formulae for the selected $Pb_2Sr_2RCu_3O_8$ single crystals determined by structural and chemical analyses.

R	REFINED FORMULAE	ICP/MS & EPMA
La	$Pb_2Sr_2LaCu_3O_8$	———
Pr	$Pb_2Sr_2PrCu_3O_8$	$Pb_{2.14(4)}Sr_{1.94(4)}Pr_{1.07(2)}Cu_{3.00}O_y$
Nd	$Pb_2Sr_2NdCu_3O_8$	———
Sm	———	$Pb_{2.05(4)}Sr_{1.93(4)}Sm_{1.15(5)}Cu_{3.00}O_y$
Eu	$Pb_2Sr_2Eu_{0.906(7)}Cu_3O_8$	$Pb_{1.79(4)}Sr_{2.03(4)}Eu_{0.89(2)}Cu_{3.00}O_y$
Tb	$Pb_2Sr_2Tb_{0.956(3)}Cu_3O_8$	$Pb_{2.39(5)}Sr_{1.89(4)}Tb_{0.91(2)}Cu_{3.00}O_y$
Dy	$Pb_2Sr_2Dy_{0.911(8)}Cu_3O_8$	$Pb_{2.12(4)}Sr_{1.98(4)}Dy_{0.95(2)}Cu_{3.00}O_y$
Y	———	$Pb_{2.00(6)}Sr_{2.08(3)}Y_{0.87(2)}Cu_{3.01(5)}O_y$

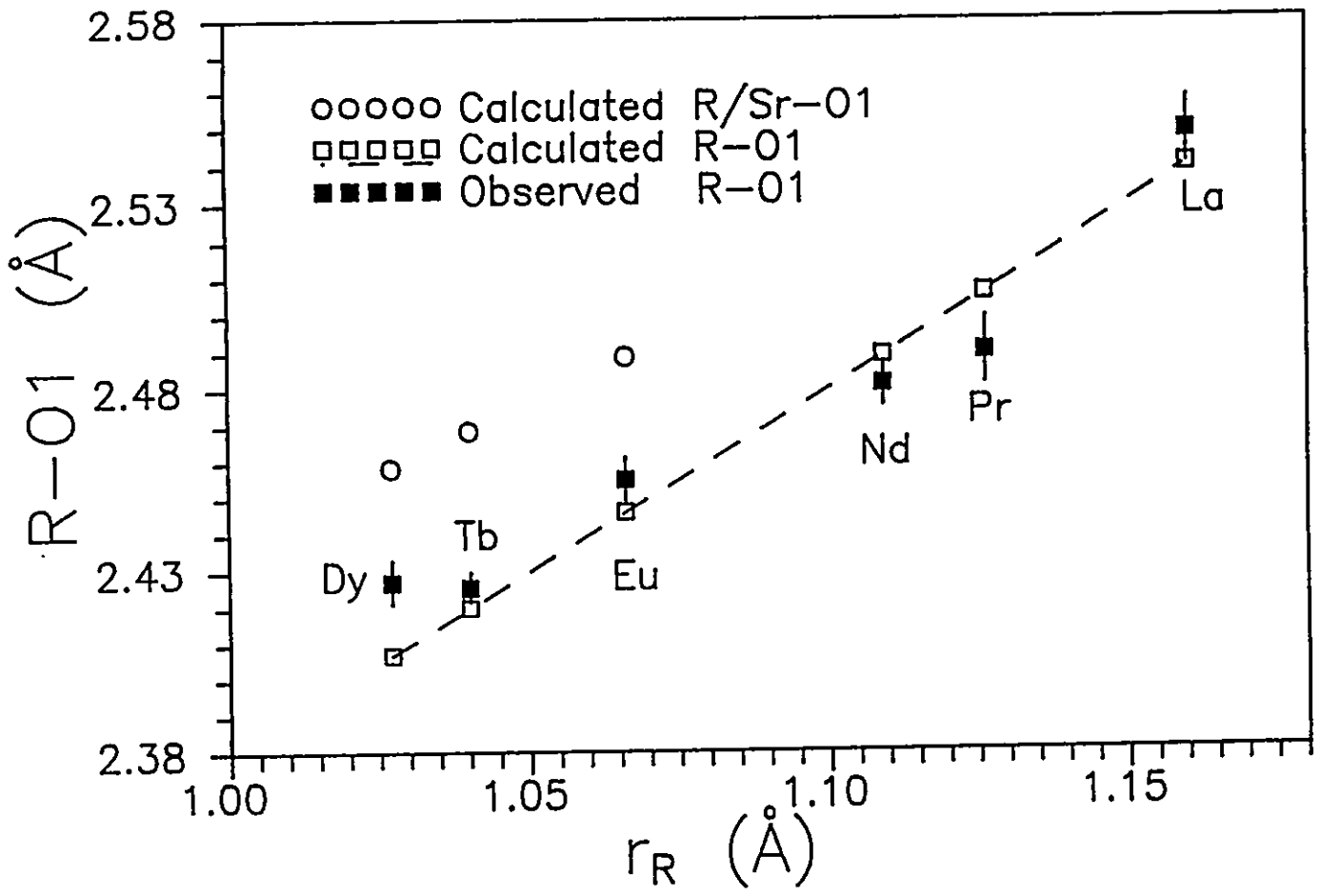

Figure 6.2 Relationships between the R-O1 bond length and r_R, the effective ionic radius of R.

6.3 Stoichiometry and superconductivity

Further evidence for the cation vacancy carrier-doping mechanism can be found from study of the polycrystalline samples where all of the carefully prepared stoichiometric polycrystalline $Pb_2Sr_2RCu_3O_8$ (R = lanthanides or Y) materials shows no sign of superconductivity down to 5K in magnetic flux exclusion measurements, while the two nonstoichiometric $Pb_2Sr_2Y_{1-x}Cu_3O_8$ (x = 0.1 and 0.2) samples are superconducting (figure 6.3.1). Guinier powder x-ray diffraction indicated that the samples with x = 0.1 and 0.2 were single phase within a detection limit of ~2%. The maximum onset T_c of 60K for x = 0.2 is comparable to the result for single crystals ($T_c \approx 74$K). The small diamagnetic signals of the powder samples imply small superconducting volumes (a few percent), similar to the results reported by Prasad et al.[114] The Ca-free $Pb_2Sr_2RCu_3O_8$ crystals with R = Eu, Gd, Dy and Ho show a diamagnetic moment but the transitions are not as sharp as that of R = Y, an onset T_c of 75K for $Pb_2Sr_2Dy_{1-x}Cu_3O_8$ crystal has been shown in figure 6.3.2 with a hump at low temperature which might be caused by the magnetization of the *f* electrons of the Dy^{3+} ions.

The existence of cation vacancies in the Ca-free $Pb_2Sr_2RCu_3O_8$ single crystals has an effect on their lattice parameters as well. Figures 6.3.3a and b show plots of the lattice parameters of single crystal and polycrystalline samples versus the effective ionic radius of the rare-earth. Here the lengths of the a and b axes of both single crystal and stoichiometric polycrystalline samples increase linearly as the size of the rare-earth in these compounds increases. No significant difference in these axes has been observed between the two sample forms except for those of R = Pr polycrystals

which are anomalously short for the reason which is not clear yet. Accordingly, the lengths of c-axis for the stoichiometric polycrystals and single crystals (R = Pr, Nd and Sm) is also proportional to the rare-earth size, while those nonstoichiometric single crystals (R = Eu, Gd, Tb, Dy, Ho and Y) clearly have longer c-axes than their corresponding polycrystals (see figure 6.3.3b). This c-axis elongation is likely traceable to the presence of R-site vacancies. A cation vacancy does expand its coordination polyhedron along the c-axis while the a and b dimensions are less affected because these are controlled by the bonding of CuO_2 plane (see §6.4 for more details).

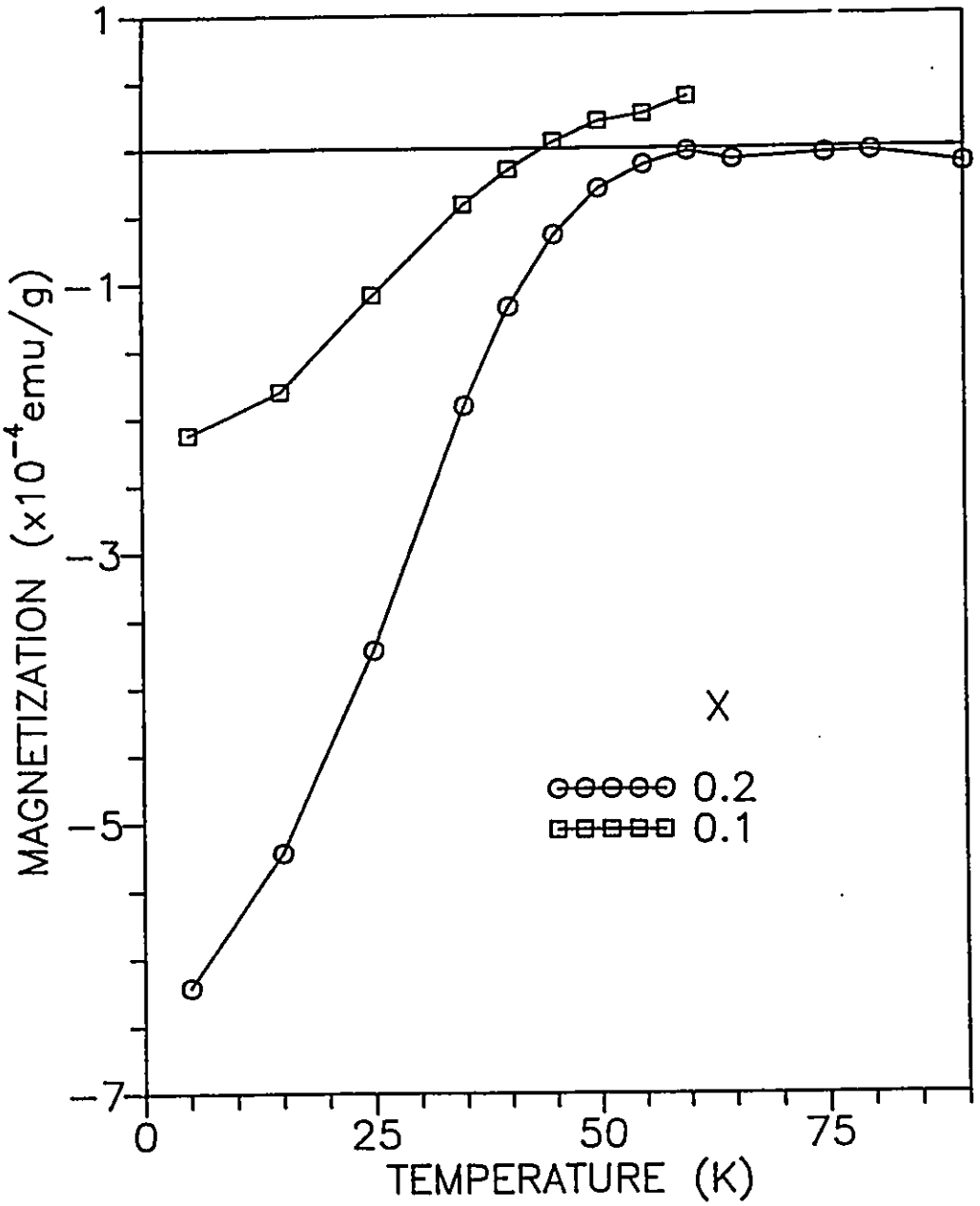

Figure 6.3.1 Temperature dependence of the zero field cooled (ZFC) magnetization for two polycrystalline $Pb_2Sr_2Y_{1-x}Cu_3O_8$ ($x = 0.1$ and 0.2) samples.

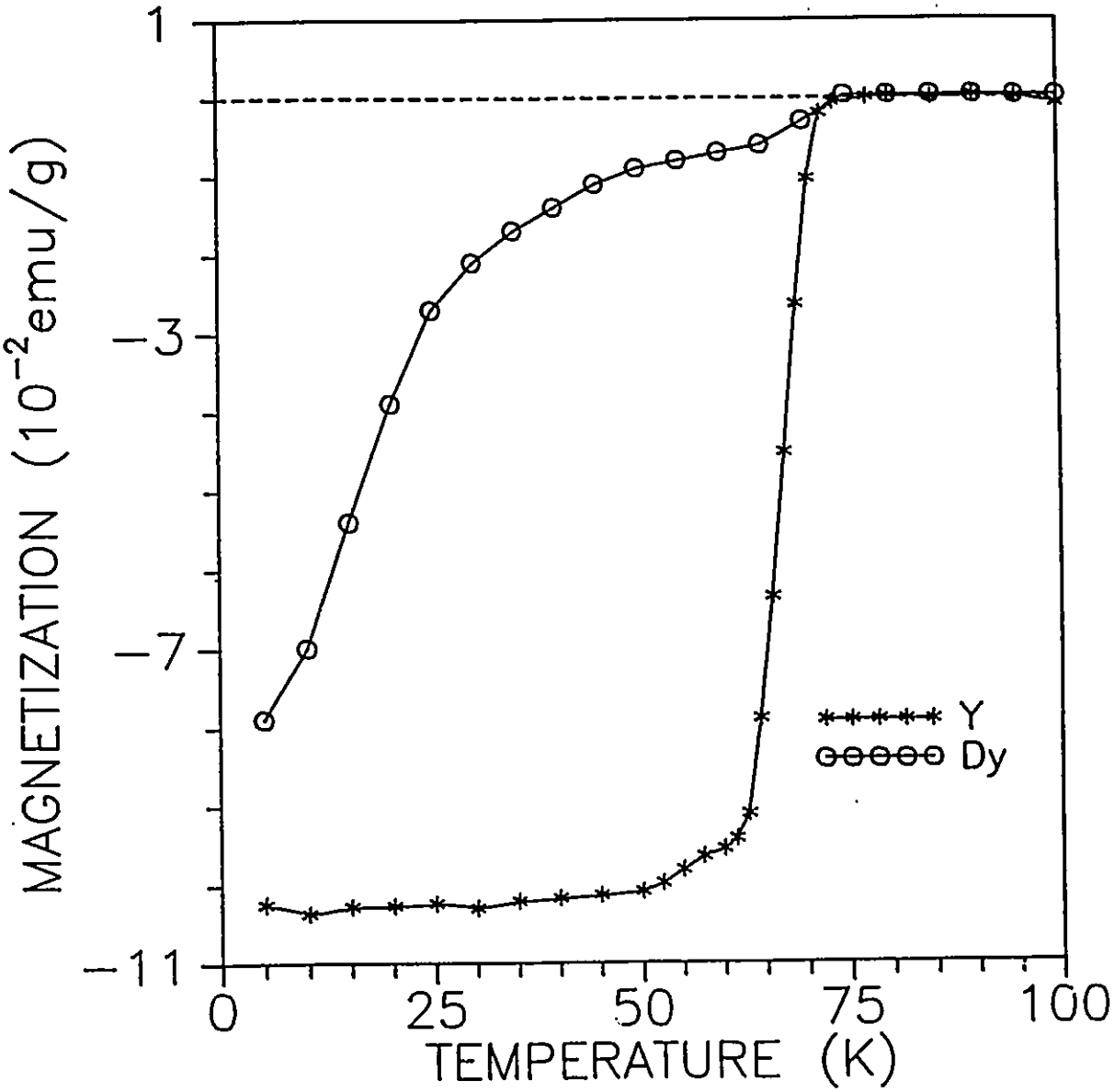

Figure 6.3.2 Temperature dependence of the zero-field cooled (ZFC) magnetization of $Pb_2Sr_2RCu_3O_8$ single crystals with R = Y and Dy.

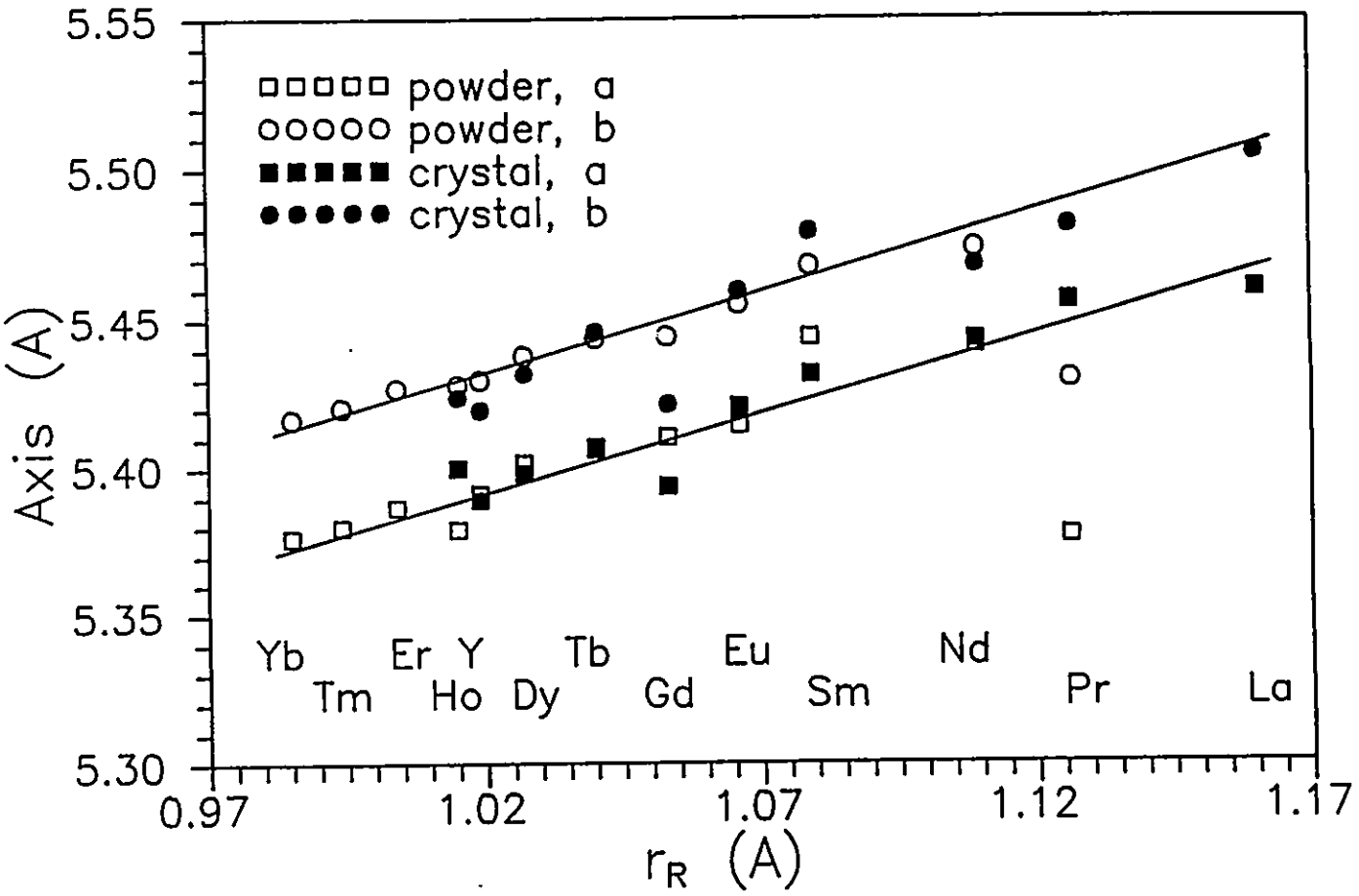

Figure 6.3.3 (a) a comparison of the lattice parameters a, b between the Ca-free $Pb_2Sr_2RCu_3O_8$ single crystal and polycrystalline samples.

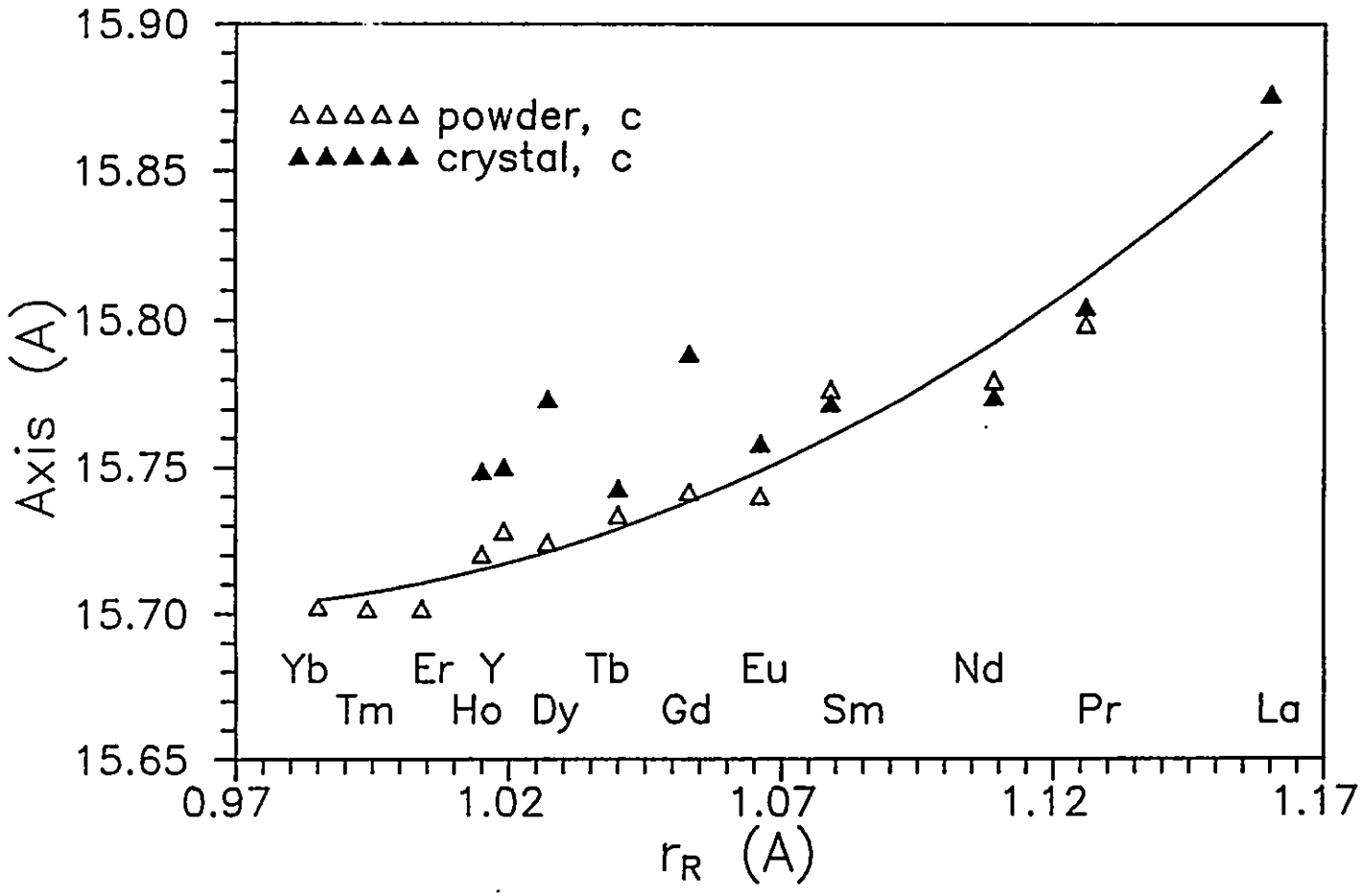

Figure 6.3.3 (b) a comparison of the lattice parameters c between the Ca-free $Pb_2Sr_2RCu_3O_8$ single crystal and polycrystalline samples.

6.4 Oxygen cage model

Naturally, the next question to ask is by what mechanism these cation vacancies (or point defects) are created, and why they exist only in certain Ca-free 2213 crystals? The fact that vacancies appear only for the smaller rare-earths and not for the larger ones suggests a size effect. The R-atoms reside in an eight-coordinated site or an oxygen cage formed by eight O1 atoms (see figure 6.4.1) which are also bonded to Cu2 atoms. The cage size will be determined by factors associated with R-size and Cu2-O1 bonding requirements. If the Cu2-O1 bonding is more important, then the cage size will depend more on this fact than on R-size. As the rare-earth radius decreases systematically through the series, the cage volume will decrease less rapidly than the R^{3+} ionic volume and R^{3+} will fit less well into the cage. A similar situation occurs for the RMO_3 perovskites (here M stands for a transition metal) as the R radius decreases. In this case the MO_6 octahedra tilt in such a way as to decrease the size of the R-O cage with decreasing R-radius. This tilting mechanism has never been observed in the layered cuprates. The creation of cation vacancies can be viewed as an alternative mechanism for decreasing the cage size and increasing the effective size of the R-ion, both of which will improve the fit. A cation vacancy, having a negative formal charge, will appear "larger" in size than a cation coordinated by oxygens. The deficit of positive charges accompanied with the creation of a cation vacancy must be balanced by an oxidation of nearest cations, Cu^{2+} in this case, in order to maintain the local charge neutrality. Thus hole-carriers are created in the Cu-d(x^2-y^2) and O-p(xy) conduction bands. Experimental evidence for the size effect can be found in figures 6.3.3 and 6.4.2 where smaller R ions reduce a and b axes, hence in-plane Cu2-O1

bonds. This is partially compensated by an increase in apical Cu2-O2 bonds. For small R, the introduction of vacancies reduces the amount by which the cell shrinks and increases the charge on Cu^{2+}, thus compensating also for the short a and b axes and, incidentally, providing the condition for superconductivity.

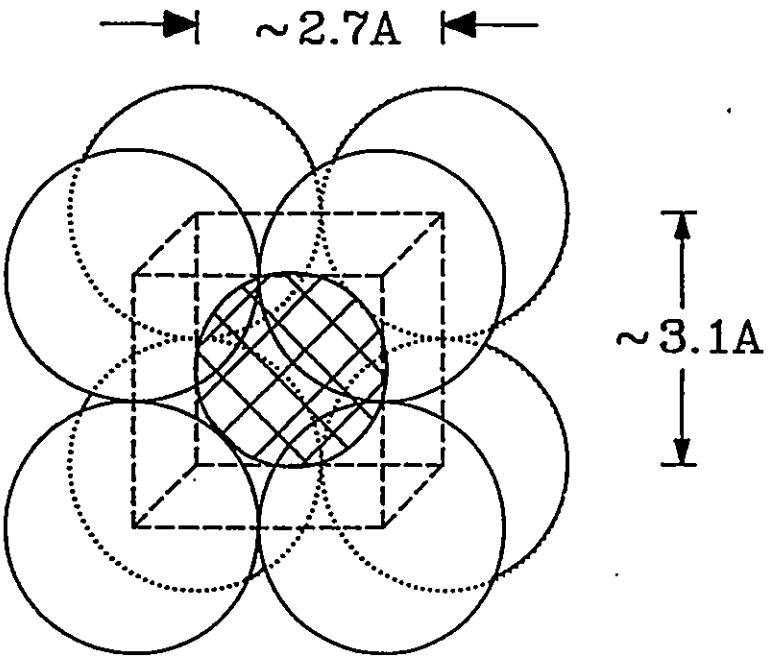

Figure 6.4.1 Oxygen cage model

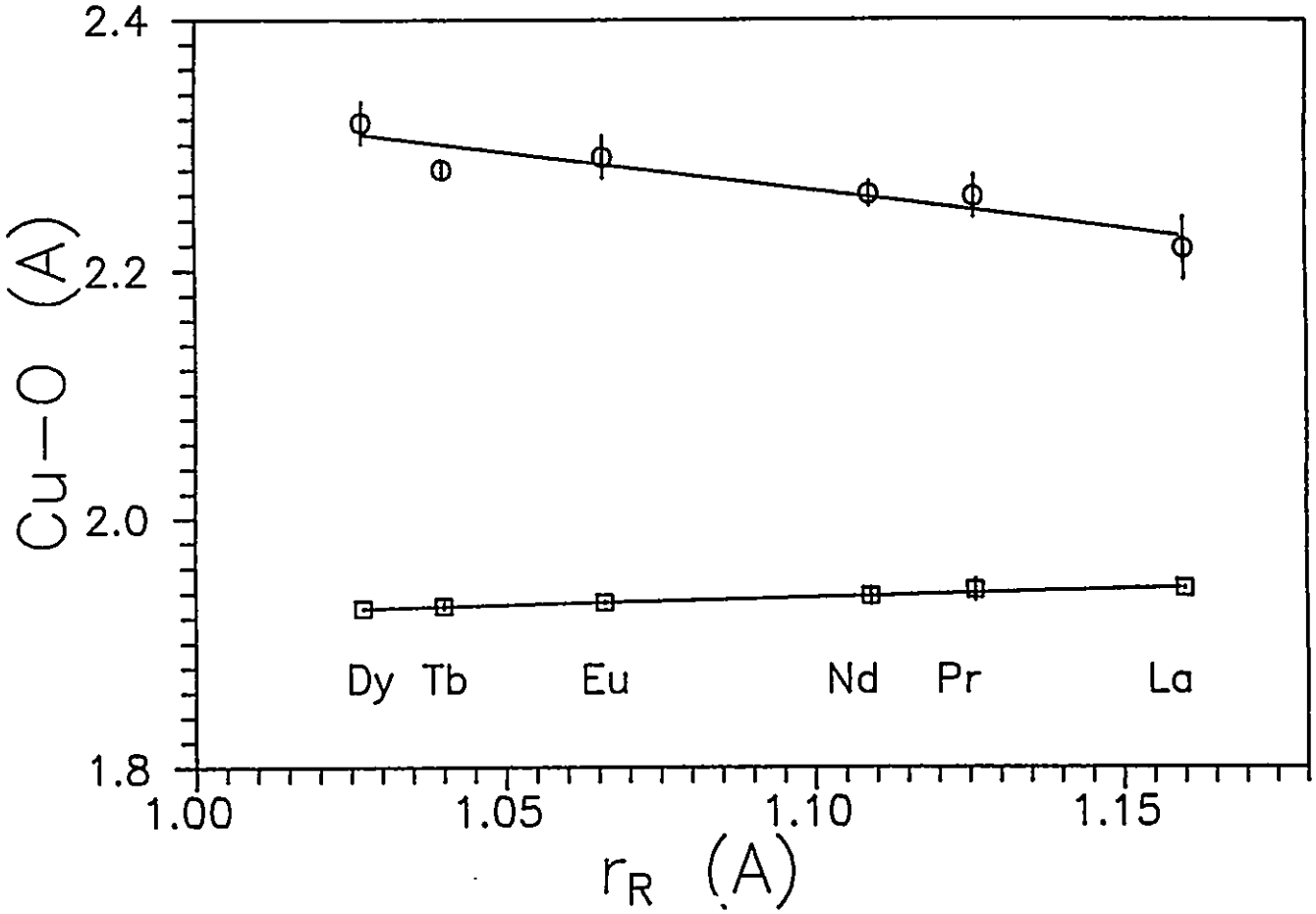

Figure 6.4.2 The distortion of the CuO_5 square pyramids as a function of decreasing rare-earth size. The □ and O represent the observed in-plane and apical Cu-O bond lengths, respectively.

6.5 Suppression of superconductivity in the $Pb_2Sr_2TbCu_3O_8$ crystals

The R = Tb crystals are of interests because of their peculiar electronic character as mentioned earlier in §6.1. The monoclinic distortion (with a ß angle deviating only slightly from 90°) observed in these crystals may be not serious enough to alter their electronic behaviour. The resistivity of one R = Tb crystal behaves like that of a semiconductor, decreasing as the temperature is raised, while that of another one exhibits a temperature-induced metal/insulator transition (figure 6.5). Neither crystal shows any evidence for a superconducting transition. Although chemical analysis showed about 9% Tb-deficiencies (see table 6.2), crystal structure analysis revealed that the refined vacancy concentration in the Tb case is only half of Eu or Dy (~4.5% versus ~9%). The small difference in the length of c-axis of single crystals and stoichiometric polycrystalline samples (see figure 6.3.3b) provides further evidence for a low cation vacancy level in the crystal. As for the existence of Tb^{4+} ions in the $Pb_2Sr_2TbCu_3O_8$ crystals, the crystallographic evidence is ambiguous: a Tb-O1 bond length is nearly identical to that of Dy-O1 suggesting that it is anomalously short (table 5.1.3). But a short apical Cu2-O2 bond for the Tb crystals (see figure 6.4.2) may imply that a charge transfer occurring between the Tb and Cu2 ions via a redox reaction $Cu2^{2+} + Tb^{4+} \rightleftharpoons Cu2^{3+} + Tb^{3+}$ which induces excess holes into the CuO_2 planes and destroys the possible superconductivity in these crystals. However, the question of the presence of Tb^{4+} in these crystals can not be answered on the basis of the present information.

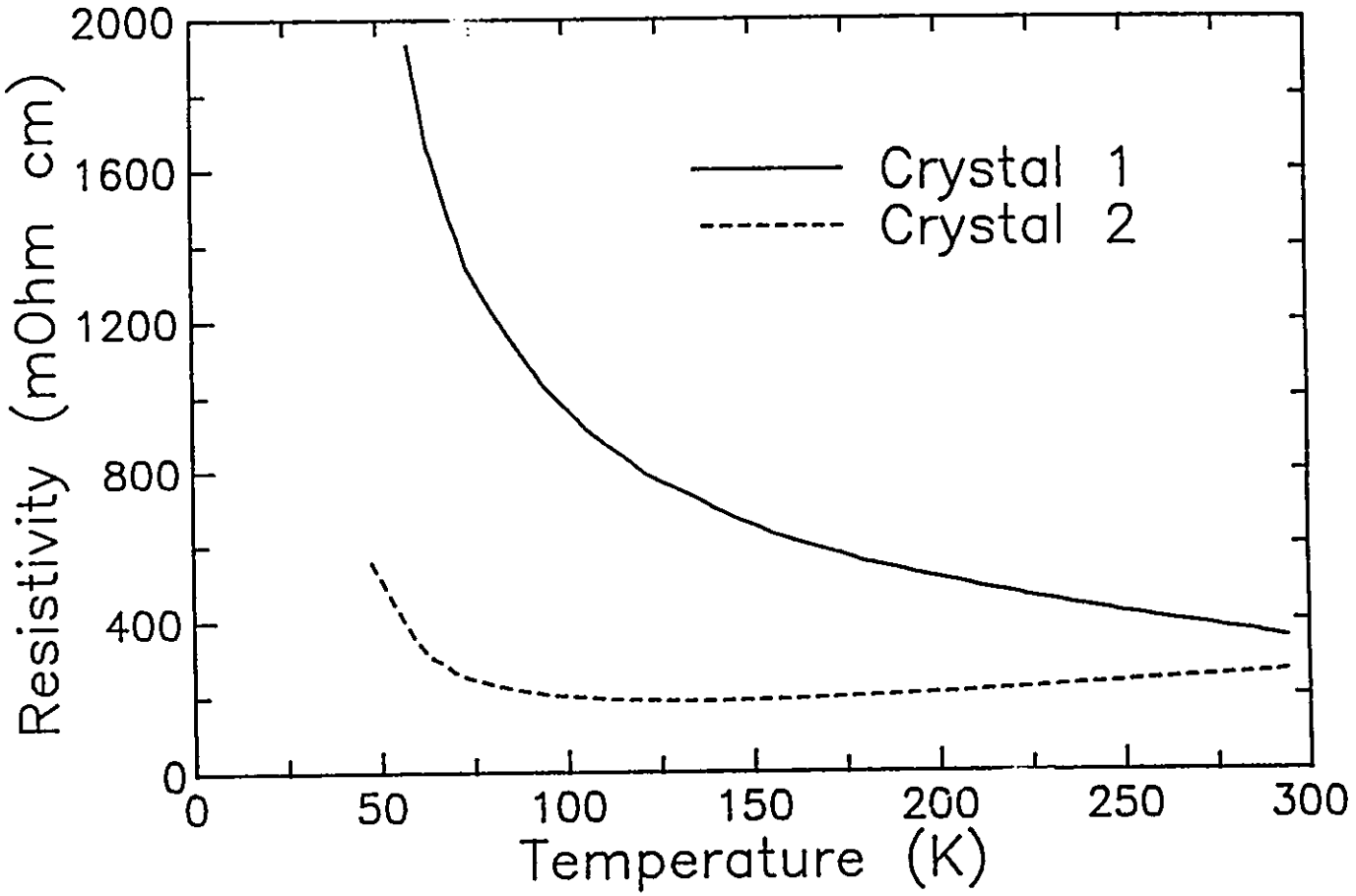

Figure 6.5 DC resistivity measurements of two $Pb_2Sr_2TbCu_3O_8$ crystals show that crystal 1 is insulating while crystal 2 shows metallic behaviour at higher temperatures and becomes insulating for temperatures lower than 100K.

6.6 Hole concentration in $Pb_2Sr_2RCu_3O_8$

According to the electrical neutrality principle, the hole concentration, or formal oxidation state (p) per copper in the CuO_2 plane of high-T_c copper oxide superconductors can be calculated by summing the different formal charges of the metal and oxygen ions. For example, the maximum T_c of 92K in the $Ba_2YCu_3O_{6+\delta}$ compound corresponds to a hole concentration (p) from 2.15 to 2.20[142]. $Pb_2Sr_2YCu_3O_{8+\delta}$ is structurally similar to $Ba_2YCu_3O_{6+\delta}$ except that the oxygen-deficient Cu^I layers in the latter are sandwiched by two PbO layers in the former. The reduced forms of both compounds, if stoichiometric, are found to be antiferromagnetic insulators[126,143,144]. Despite these similarities, they are quite different in other aspects. For example superconductivity occurs in fully oxidized $Ba_2YCu_3O_{6+\delta}$, but not in oxidized $Pb_2Sr_2YCu_3O_{8+\delta}$. The holes created by oxygen addition seem to be absorbed by oxidized lead and copper ions in the RS-units without being transferred to the conducting CuO_2 layers[50]. In that sense, the RS-unit in the title compounds acts like a *buffer* which manipulates the carriers doped or depleted by various annealing procedures. Therefore the hole concentration, p, of the Ca-free $Pb_2Sr_2R_{1-x}Cu_3O_8$ crystals studied here may be calculated in a straightforward manner, $p = 2 + 3x/2$, assuming eight oxygens per formula unit. For R = Eu, Dy and Y with $x \approx 0.09$, $p \approx 2.14$ which is not inconsistent with a T_c near 75K assuming the same systematics as found for $La_{2-x}Sr_xCuO_4$[145], $Ba_2YCu_3O_{6+\delta}$[142] and $Bi_2Sr_2CaCu_2O_{8+\delta}$[146]. For R = Tb, if the x-value of 0.045 from the structure refinement is taken, p = 2.07 which may imply that the smaller apparent doping for R = Tb lies below the critical threshold for superconductivity.

A final problem concerns the actual oxygen content of the crystals which might give rise to errors in the p-values calculated in the manner stated. Attempts to determine accurate oxygen contents by conventional thermal gravimetric analysis (TGA) gave inconsistent results due in part to the small sample size and, probably, to the contamination of PbO flux ascribed in §6.2. Useful information can be obtained from the crystal structure refinements in which the oxygen thermal and occupational parameters were refined (table 5.1.2). No significant differences are seen in the thermal parameters of the R = Eu, Tb and Dy phases, which show R-site vacancies, and those of R = La, Pr and Nd which show no such vacancies. In all cases the oxygen sites refined to full occupation to within experimental error. From a crystal chemical point of view, an oxygen stoichiometry less than eight per formula unit is also unacceptable because it means that some of the Cu^{I} ions in the RS-units are coordinated only by one oxygen.

CHAPTER 7

CONCLUSIONS

Conclusions

We have seen that the novel PbO/NaCl flux growth method produces both Ca-free and Ca-doped $Pb_2Sr_2RCu_3O_{8+\delta}$ single crystals which are bulk superconductors with an onset superconducting transition temperature ranging from 75 to 80K. High quality crystals can be obtained with relative ease using routine equipment in a short period of time. The addition of NaCl flux to the crystal growth system is of great benefit:

1) relaxing the requirement of a stringent crystal growth atmosphere,

2) enhancing the thickness and T_c of the 2213 crystals,

3) widening the crystal growth composition range,

4) lowering the eutectic temperature of the growth system,

5) stabilizing the oxidation states of the constituent elements and the composition of the melt and,

6) reducing the toxic hazard of PbO.

An ultrasonic bath/methanol separation technique enables us to recover nearly all the crystals grown and the yield of 2213 crystals obtained from starting materials can be as high as 40%.

The Ca-free $Pb_2Sr_2RCu_3O_8$ single crystal series has been found to be a fascinating system: i) it has a rich substitution chemistry; ii) the electronic properties

of the materials can be controlled by varying the size of the rare-earth constituent which is useful for studies of insulating, metallic and superconducting behaviour in the same type of crystal lattice; iii) it is structurally similar to other high-T_c copper oxide systems, such as the thallium, bismuth cuprates and the well-studied $Ba_2YCu_3O_{6+\delta}$; and iv) the materials are relatively easy to prepare in single crystal form.

A systematic crystal structure determination by single crystal x-ray diffraction shows that there are approximately 9% deficiencies in electron density at the R-sites of those crystals with R=Eu and Dy, ~4.5% for R=Tb, while none at the R=La, Pr and Nd sites. The crystal symmetry of the 2213-phase can be either orthorhombic or monoclinic depending on the oxygen ordering in the PbO layers. The crientation of the lone pair electrons of Pb^{2+} is the key to understanding the crystal chemistry of the 2213 compounds, such as crystal symmetry, oxygen ordering, the micro-twinning ... etc. Bond valence sum analysis shows that the strains inhabit mainly in the P-units and are relaxed in the RS-units by oxygen displacement in the PbO layers.

A trend from insulating to poor metallic and superconducting character of the Ca-free $Pb_2Sr_2RCu_3O_8$ single crystal series has been revealed via dc resistivity, magnetization and optical rneasurements. The deficiencies in electron density at the rare-earth sites of the Ca-free crystals with R=Eu, Gd, Dy, Ho and Y have been confirmed to be due to cation vacancies at these sites by structure refinement and chemical analysis (ICP/MS and EPMA). Therefore, a cation vacancy carrier-doping mechanism is suggested as the most plausible origin for the metallic and superconducting behaviours observed in these crystals. From these observations, we can draw a conclusion that all the stoichiometric Ca-free $Pb_2Sr_2RCu_3O_8$ single crystal and polycrystalline samples are insulating and nonsuperconducting while those

nonstoichiometric, are metallic and superconducting with the exception of the $Pb_2Sr_2TbCu_3O_8$ crystals, where an anomaly in the electronic properties seems to be caused by the low carrier-doping level or possibly the presence of Tb^{4+}.

Direction for Future Research

Evidence of a primitive symmetry in the Ca-free $Pb_2Sr_2RCu_3O_8$ crystals has been observed in the single crystal x-ray diffraction, though those $h+k=2n+1$ reflections are too weak to be refined properly. Further investigation of these crystals by neutron single crystal or electron diffractions might be fruitful.

Synthesis of other potential lead cuprates, such as the 1223 and 2224 phases whose crystal structures have been illustrated in figures 2.4.1 & 2.4.3, respectively, would be beneficial. In analogy with the Tl and Bi cuprate systems, they are possible superconductors with higher T_c than the known lead cuprates.

Extensive studies on the oxidized form of $Pb_2Sr_2YCu_3O_{8+\delta}$ have been conducted by Marezio et al.[126,147] and Gallagher et al.[120] The addition of oxygen produces a long range order in the RS-unit. This oxygen ordering, in turn, generates a complicated 4ax2b superstructure which is proposed according to the results of powder neutron diffraction[126] and electron microscopy[138]. However, more crystal structural data may be needed for constructing a reliable superstructure model.

APPENDIX

CHARGE NEUTRALITY IN VARIOUS HIGH-T_c SUPERCONDUCTORS

Table 1. Charge neutrality in the series I compounds.

(a)

n	1					
	$La_{2-x}Sr_xCaCu_2O_6$		$Nd_{2-x}Ce_xCuO_4$		$Nd_{2-x-y}Ce_xSr_yCuO_4$	
	$\{^9AO\}_2$	2	$<^8A.O_2.^8A>$	2	$\{^9AO\}_2$	2
	$\{^6CuO_2\}$	-2	$\{^4CuO_2\}$	-2	$\{^5CuO_2\}$	-2
	$\{^9AO\}_2$	2	$<^8A.O_2.^8A>$	2	$<^8A.O_2.^8A>$	2
	$\{^6CuO_2\}$	-2	$\{^4CuO_2\}$	-2	$\{^5CuO_2\}$	-2
	Q =	0		0		0

(b)

n	2		3		∞	
	$La_2CaCu_2O_{6+\delta}$		$Ln_6Ba_4Ce_2Cu_9O_{30-\delta}$		$Sr_{1-x}Ca_xCuO_2$	
	$\{^5CuO_2\}$	-2	$\{^9AO\}$	1	$\{^4CuO_2\}$	-2
	$\{^9AO\}_2$	2	$\{^5CuO_2\}$	-2	$\{^8R\}$	2
	$\{^5CuO_2\}$	-2	$<^8A.O_2.^8A>$	2		
	$\{^8R\}$	2	$\{^5CuO_2\}$	-2		
	$\{^5CuO_2\}$	-2	$\{^9AO.^3CuO.^9AO\}$	2		
	$\{^9AO\}_2$	2	$\{^5CuO_2\}$	-2		
	$\{^5CuO_2\}$	-2	$<^8A.O_2.^8A>$	2		
	$\{^8R\}$	2	$\{^5CuO_2\}$	-2		
			$\{^9AO.^3CuO\}$	1		
	Q =	0		0		0

Table 2. Charge neutrality in the series II compounds

n \ m	1		2		1.5	
	$Ba_2YCu_3O_{7-\delta}$		$Ba_2YCu_4O_8$		$Ba_4Y_2Cu_7O_{14+\delta}$	
2	$[^4CuO]$		$[^4CuO.^4CuO]$		$[^4Cu]$	1
	$\{^{10}AO.^5CuO_2\}$	-2	$\{^{10}AO.^5CuO_2\}$	-2	$\{^8AO.^5CuO_2\}$	-2
	$\{^8R\}$	3	$\{^8R\}$	3	$\{^8R\}$	3
	$\{^5CuO_2.^{10}AO\}$	-2	$\{^5CuO_2.^{10}AO\}$	-2	$\{^5CuO_2.^8AO\}$	-2
					$[^4CuO.^4CuO]$	
					$\{^{10}AO.^5CuO_2\}$	-2
					$\{^8R\}$	3
					$\{^5CuO_2.^8AO\}$	-2
Q =		-1		-1		-1

Table 3. Charge neutrality in the series III compounds.

m \ n	1			2			3		
	Tl	Bi	Pb/Cu	Tl	Bi	Pb/Sr	Tl	Bi	Pb
1	$[^6MO]$	1	1	1	$[^6MO]$	1	1	1½	$[^6MO]$	1	1	1½
	$\{^9AO\}$			½	$\{^9AO\}$				$\{^9AO\}$			¼
	$\{^5CuO_2\}$	-2	-2	-2	$\{^5CuO_2\}$	-2	-2	-2	$\{^5CuO_2\}$	-2	-2	-2
	$\{^9AO\}$			½	$\{^8R\}$	2	2	2½	$\{^8R\}$	2	2	2
					$\{^5CuO_2\}$	-2	-2	-2	$\{^4CuO_2\}$	-2	-2	-2
					$\{^9AO\}$				$\{^3R\}$	2	2	2
									$\{^5CuO_2\}$	-2	-2	-2
									$\{^9AO\}$			¼
	Q =	-1	-1	0		-1	-1	0		-1	-1	0
	Tl	Bi	Pb	Tl	Bi	Pb	Tl	Bi	Pb
2	$[^6MO]$	1	1	$[^6MO]$	1	1	$[^6MO]$	1	1
	$[^6MO]$	1	1	$[^6MO]$	1	1	$[^6MO]$	1	1
	$\{^9AO\}$			$\{^9AO\}$			$\{^9AO\}$		
	$\{^6CuO_2\}$	-2	-2	$\{^5CuO_2\}$	-2	-2	$\{^5CuO_2\}$	-2	-2
	$\{^9AO\}$			$\{^8R\}$	2	2	$\{^8R\}$	2	2
				$\{^5CuO_2\}$	-2	-2	$\{^4CuO_2\}$	-2	-2
				$\{^9AO\}$			$\{^8R\}$	2	2
							$\{^5CuO_2\}$	-2	-2
							$\{^9AO\}$		
	Q =	0	0		0	0		0	0
	Pb			Pb			Pb		
3	$[^5MO]$			$[^5MO]$			$[^5MO]$		
	$[^2Cu]$	1		$[^2Cu]$	1		$[^2Cu]$	1	
	$[^5MO]$			$[^5MO]$			$[^5MO]$		
	$\{^9AO\}$	½		$\{^9AO\}$			$\{^9AO\}$	½	
	$\{^6CuO_2\}$	-2		$\{^5CuO_2\}$	-2		$\{^5CuO_2\}$	-2	
	$\{^9AO\}$	½		$\{^8R\}$	3		$\{^8R\}$	2	
				$\{^5CuO_2\}$	-2		$\{^4CuO_2\}$	-2	
				$\{^9AO\}$			$\{^8R\}$	2	
							$\{^5CuO_2\}$	-2	
							$\{^9AO\}$	½	
	Q =	0			0			0	

REFERENCES

1. H.K. Onnes, **Leiden Com.**, (1911)120b.

2. B.W. Roberts, **Progr. Cryog.**, 4(1964)161.

3. D.C. Johnston, H. Prakash, W.H. Zachariasen, and R. Viswanathan, **Mater. Res. Bull.**, 8(1973)777.

4. A.W. Sleight, J.L. Gillson, and P.E. Bierstedt, **Solid State Commun.**, 17(1975)27.

5. J.G. Bednorz, and K.A. Muller, **Z. Phys. B - Condensed Matter**, 64(1986)189.

6. M.K. Wu, J.R. Ashburn, C.J. Torng, P.H. Hor, R.L. Meng, L. Gao, Z.J. Huang, Y.Q. Wang, and C.W. Chu, **Phys. Rev. Lett.**, 58(1987)908.

7. R.J. Cava, B. Batlogg, J.J. Krajewski, L.W. Rupp, L.F. Schneemeyer, T. Siegrist, R.B. van Dover, P. Marsh, W.F. Peck Jr., P.K. Gallagher, S.H. Glarum, J.H. Marshall, R.C. Farrow, J.V. Waszczak, R. Hull, and P. Trevor, **Nature**, 336(17)(1988)211.

8. J.S. Xue, M. Reedyk, and J.E. Greedan, *Synthesis, crystal structure and physical properties of the $Pb_2Sr_2RCu_3O_{8+\delta}$ system*, in: **High Temperature Superconductivity**, Nova Science Publisher Inc., 1992.

9. T. Rouillon, J. Provost, M. Hervieu, D. Groult, C. Michel, and B. Raveau, **Physica C**, 159(1989)201-9.

10. W.T. Fu, H.W. Zandbergen, J.M. van Ruitenbeek, Q. Xu, A.A. Verheijen, A. Smits, and L.J. De Jongh, **Physica C**, 162(1989)979.

11. H. Sasakura, K. Nakahigashi, S. Minamigawa, S. Nakamishi, M. Kogachi, N. Fukuoka, M. Yoshikawa, S. Noguchi, K. Okuda, and A. Yanase, **Jpn. J. Appl. Phys. Pt.2**, 29(4)(1990)L583.

12. S. Adachi, K. Setsune, and K. Wasa; **Jpn. J. Appl. Phys. (Pt.2)**, 29(1990)L1799-802.

13. T. Rouillon, V. Caignaert, M. Hervieu, C. Michel, D. Groult, and B. Raveau, (preprint).

14. T. Maeda, K. Sakuyama, S. Koriyama, A. Ichinose, H. Yamauchi, and S. Tanaka, **Physica C**, 169(1990)133-6.

15. T. Rouillon, D. Groult, M. Hervieu, C. Michel, and B. Raveau, **Physica C**, 167(1990)107.

16. A. Tokiwa, T. Oku, M. Nagoshi, M. Kikuchi, K. Hiraga, and Y. Syono, **Physica C**, 161(1989)459-67.

17. C. Kittel, **Introduction to Solid State Physics**, Sixth ed. John Wiley & Sons Inc. New York, (1986)322.

18. N.W. Ashcroft, and N.D. Mermin, **Solid State Physics**, Holt, Rinehart & Winston, New York, (1976)733.

19. A.W. Sleight, **Science**, 242(1988)1519-27.

20. C.N.R. Rao, **Modern Phys. Lett. B**, 2(1988)1217-21.

21. J.C. Fuggle, P.J.W. Weijs, R. Schoorl, G.A. Sawatzky, J. Fink, N. Nucker, P.J. Durham, and W.M. Temmerman, **Phys. Rev. B**, 37(1988)123.

22. D.D. Sarma, and C.N.R. Rao, **Solid State Commun.**, 65(1988)47.

23. D.D. Sarma, **Phys. Rev. B**, 37(1988)7948.

24. R.J. Cava, **Science**, 247(1990)656-62.

25. T.E. Jones, W.C. McGinnis, R.D. Boss, E.W. Jacobs, J.W. Schindler, and C.D. Rees, *Chemistry of High-Temperature Superconductors II*, in: **Am. Chem. Soc. Symp. No.377**, George TF, Nelson DL, eds., (1988)156-67.

26. H. Nobumasa, K. Shimizu, and T. Kawai, **Z. Phys. B - Condensed Matter**, 83(1991)7.

27. A.W. Hewat, P. Bordet, J.J. Capponi, C. Chaillout, J. Chenavas, M. Godinho, E.A. Hewat, J.L. Hodeau, and M. Marezio, **Physica C**, 156(1988)369.

28. A.W. Hewat, E.A. Hewat, J. Brynestad, H.A. Mook, and E.D. Specht, **Physica C**, 152(1988)438.

29. E. Sonder, B.C. Chakoumakos, and B.C. Sales, **Phys. Rev. B**, 40(1989)6872-7.

30. P. Bordet, J.J. Capponi, C. Chaillout, J. Chenavas, A.W. Hewat, E.A. Hewat, J.L. Hodeau, M. Marezio, J.L. Tholence, and D. Tranqui, **Physica C**, 156(1988)189.

31. A.F. Wells, **Structural Inorganic Chemistry**, Fifth edition, Clarendon Press, Oxford (1984).

32. J. Choisnet, J.M. Bassat, H. Pilliere, P. Odier, and M. Leblanc, **Solid State Commun.**, 66(1988)1245-9.

33. I.D. Brown, *Chemistry of Electronic Ceramic Materials*, in: **Proc. Int. Conf.** Jackson, WY, (1990)471-83.

34. D. Jung, M.H. Whangbo, N. Herron, and C.C. Torardi, **Physica C**, 160(1989)381.

35. W. Dmowski, B.H. Toby, T. Egami, M.A. Subramanian, J. Gopalakrishnan, and A.W. Sleight, **Phys. Rev. Lett.**, 61(1988)2608.

36. J.D. Jorgensen, **Jpn. J. Appl. Phys.**, 26(Suppl. 26-3)(1987)2017.

37. A.W. Hewat, **Europhys. News**, 19(1988)73.

38. J.B. Torrance, Y. Tokura, and A. Nazzal, **Chemtronics**, (Dec.1987).

39. K. Yvon, and M. François, **Z. Phys. B - Condensed Matter**, 76(1989)413-44.

40. J.A. Wilson, **J. Phys. C**, 20(1987); ibid 21(1988)2067.

41. R.J. Cava, in: **Proc. Europ. Workshop High T_c Supercond. & Potential Appl.** Commission of the Europ. Communities (July 1987 Genova).

42. B. Raveau, C. Michel, M. Hervieu, and J. Provost, **Physica C**, 153-5(1988)3.

43. A. Santoro, F. Beech, M. Marezio, and R.J. Cava, **Physica C**, 156(1988)693.

44. T. Fries, G. Mayer-von Kurthy, A. Ehmann, W. Wischert, and S. Kemmler-sack, **J. Less-common Metals**, 159(1990)337-41.

45. W.H. Gong, J.S. Xue, and J.E. Greedan, **J. Solid State Chem.**, 91(1991)180.

46. Von Chr.L.Teske, and H.K. Müller-Buschbaum, **Z. Anorg. Allg. Chem.**, 371(1969)325.

47. Y. Tokura, H. Takagi, and S. Uchida, **Nature**, 337(1989)345.

48. N. Nguyen, J. Choisnet, L. Errakho, C. Michel, and B. Raveau, **Mater. Res. Bull.**, 15(1980)891.

49. J.B. Torrance, Y. Tokura, A. Nazzal, and S.S.P. Parkin, **Phys. Rev. Lett.**, 60(1988)542.

50. R.J. Cava, B. Batlogg, R.B. van Dover, J.J. Krajewski, J.V. Waszczak, R.M. Fleming, W.F. Peck Jr., L.W. Rupp Jr., P. Marsh, A.C.W.P. James, and L.F. Schneemeyer, **Nature**, 345(1990)602-4.

51. M. Takano, Y. Takeda, H. Okada, M. Miyamoto, and T. Kusaka, **Physica C**, 159(1989)375-8.

52. B. Okai, **Jpn. J. Appl. Phys. Pt.2**, 28(1989)L2251-2.

53. T. Siegrist, S.M. Zahurak, D.W. Murphy, and R.S. Roth, **Nature**, 334(1988)231.

54. B. Okai, **Jpn. J. Appl. Phys. Pt.2**, 29(1990)L2091-2.

55. R.J. Cava, A. Santoro, D.W.Johnson Jr., and W.W. Rhodes, **Phys. Rev. B**, 35(1987)6716.

56. Private communication from J.S. Xue, *Crystal structure determination of $Nd_{2-x}Ce_xCuO_{4-y}$*, (April 1989).

57. H. Sawa, S. Suzuki, M. Watanabe, J. Akimitsu, H. Matsubara, H. Watabe, S. Uchida, K. Kokusho, H. Asano, F. Izumi, and E. Takayama-Muromachi, **Nature**, 337(1989)347.

58. A. Fuertes, X. Obradors, J.M. Navarro, P. Gomez-Romero, N. Casan-Pastor, F. Perez, J. Fontcuberta, C. Miravitlles, J. Rodriguez-Carvajal, and B. Martinez, **Physica C**, 170(1990)153-160.

59. B. Okai, **Jpn. J. Appl. Phys. Pt.2**, 30(1991)L179-81.

60. H. Sawa, K. Obara, J. Akimitsu, Y. Matsui, and S. Horiuchi, **J. Phys. Soc. Jpn.**, 58(7)(1989)2252-5.

61. M.G. Smith, A. Manthiram, J. Zhou, J.B. Goodenough, and J.T. Markert, **Nature**, 351(1991)549-51.

62. R.J. Cava, A.W. Hewat, E.A. Hewat, B. Batlogg, M. Marezio, K.M. Rabe, J.J. Krajewski, W.F. Peck Jr., and L.W. Rupp Jr., **Physica C**, 165(1990)419-433.

63. R.W. Veal, A.P. Paulikas, H. You, H. Shi, Y. Fang, and J.W. Downey, **Phys. Rev. B**, 42(1990)6305-16.

64. Y.P. Lin, J.E. Greedan, A.H. O'Reilly, J.N. Reimers, C.V. Stager, and M.L. Post, **J. Solid State Chem.**, 84(1990)226.

65. H.W. Zandbergen, R. Gronsky, K. Wang, and G. Thomas, **Nature**, 331(1988)596.

66. T. Miyatake, S. Gotoh, N. Koshizuka, and S. Tanaka, **Nature**, 341(1989)41-2.

67. J. Karpinski, C. Beeli, E. Kaldis, A. Wisard, and E. Jilek, **Physica C**, 153-5(1988)830.

68. J.E. Greedan, A.H. O'Reilly, and C.V. Stager, **Phys. Rev. B**, 35(1987)8770.

69. B. Okai, **Jpn. J. Appl. Phys. Pt.2**, 29(1990)L2180-2.

70. P. Bordet, C. Chaillout, J. Chenavas, J.L. Hodeau, M. Marezio, J. Kapinski, and E. Kaldis, **Nature**, 334(1988)596-8.

71. P. Fischer, J. Karpinski, E. Kaldis, E. Jilek, and S. Rusiecki, **Solid State Commun.**, 69(1989)531.

72. A. Sundaresan, A.K. Rajarajan, L.C. Gupta, M. Sharon, and R. Vijayaraghavan, **Physica C**, 178(1990)193-6.

73. B. Morosin, D.S. Ginley, P.F. Hlava, M.J. Carr, R.J. Baughman, J.E. Schirber, E.L. Venturini, and J.F. Kwak, **Physica C**, 152(1988)413.

74. B. Morosin, D.S. Ginley, J.E. Schirber, and E.L. Venturini, **Physica C**, 156(1988)587.

75. M.A. Subramanian, J.B. Parise, J.C. Calabrese, C.C. Torardi, J. Gopalakrishnan, and A.W. Sleight, **J. Solid State Chem.**, 192(1988)77.

76. P. Haldar, K. Chen, B. Maheswaran, A. Riog-Janicki, N.K. Jaggi, R.S. Markiewiez, and B.C. Giessen, **Science**, 241(1988)1198-200.

77. M.A. Subramanian, C.C. Torardi, J. Gopalakrishnan, P.L. Gai, J.C. Calabrese, T.R. Askew, R.B. Flippen, and A.W. Sleight, **Science**, 242(1988)249-52.

78. R.A. Mohan Ram, A. Clearfield, P.S. Kobiela, and W.P. Kirk, **Physica C**, 166(1990)125.

79. M.A. Subramanian, G.H. Kwei, J.B. Parise, J.A. Goldstone, and R.B. von Dreele, **Physica C**, 166(1990)19-24.

80. M.H. Pan, and M. Greenblatt, **Physica C**, 176(1991)80-6.

81. A.K. Ganguli, K.S. Nanjundaswamy, and C.N.R. Rao, **Physica C**, 156(1988)788.

82. S.S.P. Parkin, V.Y. Lee, A.I. Nazzal, R. Savoy, R. Beyes, and S.J. LaPlaca, **Phys. Rev. Lett.**, 61(1988)750-3.

83. C. Michel, M. Hervieu, M.M. Borel, A. Grandin, F. Deslandes, J. Provost, and B. Raveau, **Z. Phys. B-Condensed Matter**, 68(1988)421.

84. S. Amelinckx, G. van Tendeloo, H.W. Zandbergen, and J. van Lauduyt, **J. Less-Common. Metals**, 150(1989)71-94.

85. Z.Z. Sheng, and A.M. Hermann, **Nature**, 332(1988)55.

86. M.A. Subramanian, C.C. Torardi, J. Gopalakrishnan, J.C. Calabrese, K.J. Morrissey, T.R. Askew, R.B. Flippen, U. Chowdhry, A.W. Sleight, J.J. Lin, and S.J. Poon, **Physica C**, 153-155(1988)608.

87. K. Imai, I. Nakai, T. Kawashima, S. Sueno, and A. Ono, **Jpn. J. Appl. Phys. Pt.2**, 27(1988)L1661.

88. P. Bordet, J.J. Capponi, C. Chaillout, J. Chenavas, A.W. Hewat, E.A. Hewat, J.L. Hodeau, M. Marezio, J.I. Tholence, and D. Tranqui, **Physica C**, 153-155(1988)623.

89. P. Lee, Y. Gao, H.S. Sheu, V. Petricek, R. Restori, P. Coppens, A. Darovskikh, J.C. Phillips, A.W. Sleight, and M.A. Subramanian, **Science**, 244(1989)62.

90. Y. LePage, W.R. Mckinnon, J.M. Tarascon, and P. Barboux, **Phys. Rev. B**, 40(1989)6810.

91. R.M. Hazen, L.W. Finger, R.J. Angel, C.T. Prewitt, N.L. Ross, C.G. Hadidiacos, P.J. Heaney, D.R. Veblen, Z.Z. Sheng, A. El Ali, and A.M. Hermann, **Phys. Rev. Lett.**, 60(1988)1657.

92. S. Kemmler-Sack, A. Ehmann, R. Kiemel, W. Losch Schafer, L. Kan, and B. Elschner, **J. Less-Common Metal**, 144(1988)L1.

93. C.C. Torardi, M.A. Subramanian, J.C. Calabrese, J. Gopalakrishnan, E.M. McCarron, K.J. Morrissey, T.R. Askew, R.B. Flippen, U. Chowdhry, and A.W. Sleight, **Phys. Rev. B**, 38(1988)225.

94. M.A. Subramanian, **Nature**, 332(1988)420.

95. C.C. Torardi, M.A. Subramanian, J.C. Calabrese, J. Gopalakrishnan, E.M. McCarron, K.J. Morrissey, T.R. Askew, R.B. Flippen, U. Chowdhry, and A.W. Sleight, **Science**, 240(1988)631.

96. J.S. Xue, M. Reedyk, Y.P. Lin, C.V. Stager, and J.E. Greedan, **Physica C**, 166(1990)29.

97. Private communication from Dr. I.D. Brown, and J.S. Xue, *Structures of ceramic superconductors*, (Nov. 1989).

98. G. Bergerhoff, R. Hundt, R. Seivers, and I.D. Brown, **J. Chem. Inf. Comput. Sci.**, 23(1983)66-9.

99. I.D. Brown, **Acta Cryst.**, B44(1988)545-53.

100. R.J. Cava, M. Marezio, J.J. Frajewski, W.F. Peck Jr, A. Santoro, and F. Beech, **Physica C**, 157(1989)272-8.

101. M.A. Subramanian, J. Gopalakrishnan, C.C. Torardi, P.L. Gai, E.D. Boyes, T.R. Askew, R.B. Flippen, W.E. Farneth, and A.W. Sleight, **Physica C**, 157(1989)124-30.

102. K. Kadowaki, M.J.V. Menken, and A.C. Moleman, **Physica C**, 159(1989)165.

103. W.T. Fu, H.W. Zandbergen, W.G. Haije, and L.J. De Jongh, **Physica C**, 159(1989)210.

104. T. Maeda, K. Sakuyama, N. Sakai, H. Yamauchi, and S. Tanaka, **Physica C**, 177(1991)337-44.

105. T. Rouillon, D. Groult, M. Hervieu, C. Michel, and B. Raveau, **Physica C**, 167(1990)107.

106. T. Rouillon, R. Retoux, D. Groult, C. Michel, M. Hervieu, J. Provost, and B. Raveau, **J. Solid State Chem.**, 78(1989)322-5.

107. A. Tokiwa, T. Oku, M. Nagoshi, and Y. Syono, **Physica C**, 181(1991)311-9.

108. U. Amador, F. Garcia-Alvarado, E. Moran, M.A. Alario-Franco, and J. Rodriguez-Carjaval, **Physica C**, 165(1990)499-504.

109. L.F. Schneemeyer, R.J. Cava, A.C.W.P. James, P. Marsh, T. Siegrist, J.V. Waszczak, J.J. Krajewski, W.P. Peck Jr., R.L. Opila, S.H. Glarum, J.H. Marshall, R. Hull, and J.M. Bonar, **Chemistry of Materials**, 1(1989)548.

110. Z. Korczak, W. Korczak, S. Kolesnik, T. Skosliewicz, and J. Igalson, **Supercond. Sci. Technol.**, 3(1990)370.

111. M. Reedyk, J.S. Xue, J.E. Greedan, C.V. Stager, and T. Timusk, *Anisotropy in selected electrical, magnetic and optical properties of $Pb_2Sr_2(Y/Ca)Cu_3O_8$*, in: **Proc. 5th Ann. Conf. Supercond. Appl.**, Buffalo, NY. Sept. 1991.

112. M. Reedyk, C.V. Stager, T. Timusk, J.S. Xue, and J.E. Greedan, **Phys. Rev. B**, (accepted).

113. M. Masuzawa, T. Noji, Y. Koike, and Y. Saito, **Jpn. J. Appl. Phys.**, 28(1989)L1524.

114. R. Prasad, N.C. Soni, K. Adhikary, S.K. Malik, and C.V. Tomy, **Solid State Commun.**, 76(1990)667-9.

115. H. Adachi, S. Adachi, Y. Ichikawa, K. Setsune, and L. Wasa, **Jpn. J. Appl. Phys., Pt.2**, 30(1991)L39-41.

116. J.J. Capponi, O. Chmaissem, T. Fournier, M.F. Gorius, S. Korczak, M. Marezio, and J.L. Tholence, **J. Less-common Metals**, 164-5(1990)808-15.

117. T. Hibiya, S. Imoto, T. Satoh, Y. Nakabayashi, and M. Sakonjyu, **J. Crystal Growth**, 102(1990)862-8.

118. R.D. Shannon, **Acta Cryst.**, A32(1976)751.

119. C.K. Chen, B.M. Wanklyn, E. Dieguez, A.J. Cook, J.W. Hodby, A. Schwartzbrod, A. Dabkowski, and H. Dabkowska, **J. Crystal Growth**, 118(1992)101.

120. P.K. Gallagher, H.M. O'Bryan, R.J. Cava, A.C.W.P. James, D.W. Murphy, W.W. Rhodes, J.J. Krajewski, W.F. Peck Jr., and J.V. Waszczak, **Chemistry of Materials**, 1(1989)277.

121. L.J. van der Pauw, **Phillips Res. Rep.**, 13(1958)1.

122. J.S. Xue, M, Reedyk, A. Dabkowski, H. Dabkowska, J.E. Greedan, and C.H. Chen, **J. Crystal Growth**, 113(1991)371-8.

123. L.D. Calvert, J.L. Flippen-Anderson, C.R. Hubbard, Q.C. Johnson, P.G. Lenhert, M.C. Nichols, W. Parrish, D.K. Smith, G.S. Smith, R.L. Snyder, and R.A. Young, **Symposium on Accuracy in Powder Diffraction**, Washington,D.C., (1979)16.

124. A. Dabkowski, H. Dabkowska, J.E. Greedan, J.S. Xue, and C.V. Stager, **J. Cryst. Growth**, (submitted).

125. R. Hughes, Y. Lu, T. Timusk, and J. Preston, **J. Appl. Phys. Lett.**, 58(1991)762.

126. M. Marezio, A. Santoro, J.J. Capponi, E.A. Hewat, R.J. Cava, and F. Beech, **Physica C**, 169(1990)401.

127. E.A. Hayri, and A. Kvick, **J. Solid State Chem.**, 84(1990)144.

128. J.S. Xue, M. Reedyk, J.E. Greedan, and T. Timusk, **J. Solid State Chem.**, (accepted).

129. J.S. Xue, J.E. Greedan, and M. Maric, **J. Solid State Chem.**, (accepted).

130. M. Reedyk, T. Timusk, J.S. Xue, and J.E. Greedan, **Phys. Rev. B**, 45(1992)7406.

131. C. Chaillout, O. Chmaissen, J.J. Capponi, T. Fournier, G. McIntyre, and M. Marezio, **Physica C**, 175(1991)293.

132. Y. LePage, **J. Appl. Cryst.**, 15(1982)255.

133. J.E. Jorgensen, and N.H. Andersen, **Acta Chem. Scand.**, 45(1991)19.

134. H. Fujishita, S. Yamagata, and M. Sato, **J. Phys. Soc. Jpn.**, 60(1991)913.

135. W.G. Haije, K. Kadowaki, M.J.V. Menken, A.C. Moleman, A.A. Menovsky, J.J.M. Franse, and E. Frikee, **Physica C**, 162-4(1989)875.

136. H.W. Zandbergen, K. Kadowaki, M.J.V. Menken, A.A. Menovsky, G. van Tendeloo, and S. Amelinckx, **Physica C**, 158(1989)155.

137. J.E. Jorgensen, **Solid State Commun.**, 80(1991)613-5.

138. E.A. Hewat, J.J. Capponi, R.J. Cava, C. Chaillout, M. Marezio, and J.L. Tholence, **Physica C**, 157(1989)509-14.

139. I.D. Brown, and D. Altermatt, **Acta Cryst.**, B41(1985)244.

140. A.K. Cheetham, A.M. Chippindale, and S.J. Hibble, **Nature**, 333(1988)21.

141. L.F. Mattheiss, and D.R. Hamann, **Phys. Rev. B**, 39(7)(1989)4780.

142. Y. Tokura, J.B. Torrance, T.C. Huang, and A.I. Nazzal, **Phys. Rev. B**, 38(1988)7156.

143. J.M. Tranquada, D.E. Cox, W. Kanmann, H. Moudden, G. Shirane. M. Suenaga, P. Zolliger, P. Vaknin, S.K. Sinha, M.S. Alvarez, A.J. Jacobson, and D.C. Johnson, **Phys. Rev. B**, 60(1987)156-9.

144. T. Oashi, K. Kumagai, and K. Kadowaki, J. **Phys. Soc. Jpn**, 59(1990)1549-52.

145. J.B. Torrance, Y. Tokura, A.I. Nazzal, A. Bezinge, T.C. Huang, and S.S.P. Parkin, **Phys. Rev. Lett.**, 61(9)(1988)1127.

146. W.A. Groen, D.M. deLeeuw, and L.F. Feiner, **Physica C**, 165(1990)55.

147. M. Marezio, **Acta Cryst.**, A47(1991)640-54.